

2006

## Ultra-violet lithography of thick photoresist for the applications in BioMEMS and micro optics

Ren Yang

*Louisiana State University and Agricultural and Mechanical College*

Follow this and additional works at: [https://digitalcommons.lsu.edu/gradschool\\_dissertations](https://digitalcommons.lsu.edu/gradschool_dissertations)



Part of the [Engineering Science and Materials Commons](#)

---

### Recommended Citation

Yang, Ren, "Ultra-violet lithography of thick photoresist for the applications in BioMEMS and micro optics" (2006). *LSU Doctoral Dissertations*. 3468.

[https://digitalcommons.lsu.edu/gradschool\\_dissertations/3468](https://digitalcommons.lsu.edu/gradschool_dissertations/3468)

This Dissertation is brought to you for free and open access by the Graduate School at LSU Digital Commons. It has been accepted for inclusion in LSU Doctoral Dissertations by an authorized graduate school editor of LSU Digital Commons. For more information, please contact [gradetd@lsu.edu](mailto:gradetd@lsu.edu).

# **ULTRA-VIOLET LITHOGRAPHY OF THICK PHOTORESIST FOR THE APPLICATIONS IN BIOMEMS AND MICRO OPTICS**

A Dissertation  
Submitted to the Graduate Faculty of the  
Louisiana State University and  
Agricultural and Mechanical College  
in partial fulfillment of the  
requirements for the degree of  
Doctor of Philosophy

in

The Interdepartmental Program in Engineering Sciences

by  
Ren Yang  
B.S., Tsinghua University, 1996  
M.S., Tsinghua University, 1999  
M.S., Louisiana State University, 2002

August 2006

## **ACKNOWLEDGEMENTS**

The author would like to sincerely thank his major professor, Dr. Wanjun Wang. Without his constant encouragement, insightful suggestions, and many devoted help, the research work could not be done progressively.

The author would also like to thank Dr. J. Choi, Dr. S. Soper, Dr. S. Pang, and Dr. R. Tague for their inspiring suggestions, their time and effort to serve on his examination committee.

The author would also like to thank his fellow graduate students in the research group- J. Williams, S. Jeong, D. Lee, W. Dai, and R. Fan for their help, and the great time spent together.

Finally, the author wants to express particular gratefulness to his parents, his wife, and his son for their firm and continuous love and support.

# TABLE OF CONTENTS

<b>ACKNOWLEDGEMENTS .....</b>	<b>ii</b>
<b>ABSTRACT .....</b>	<b>vi</b>
<b>CHAPTER 1. INTRODUCTION.....</b>	<b>1</b>
<b>CHAPTER 2. UV LITHOGRAPHY OF ULTRA THICK SU-8 PHOTORESIST .....</b>	<b>6</b>
2.1 Review of the State-of-the-Art for UV-Lithography of SU-8 .....	6
2.2 Basic Steps for UV Lithography of SU-8 and Some Processing Tips.....	7
2.2.1 Pre-treatment of the Substrate.....	8
2.2.2 Spin Coat of SU-8.....	8
2.2.3 Soft Bake.....	9
2.2.4 Exposure .....	10
2.2.5 Post Exposure Bake (PEB) .....	11
2.2.6 Development .....	12
2.2.7 Treatment of Flood Exposure and Extra Hard Bake.....	15
2.2.8 Removing of Cured SU-8 .....	15
2.3 Study of Diffraction Compensation and Wavelength Selection in Lithography .....	15
2.3.1 Diffraction Caused by Air Gap and Wavelength Dependence of UV Absorption Rate of SU-8 .....	16
2.3.2 Numerical Analysis of Diffraction and the Absorptions Spectrum on UV Lithography of Ultra Thick SU-8 Resist.....	19
2.3.3 Experimental Results Using Filtered Light Source and Air Gap Compensation for Diffraction.....	24
2.4 Tapered Sidewall in <i>i</i> -line and <i>h</i> -line Lithography and Their Applications .....	32
2.5 Tilted Lithography of SU-8 and Refraction Compensation.....	37
<b>CHAPTER 3. USING CURED SU-8 MICRO-MOLD INSERT TO REPLICATE BIODEGRADABLE (PLGA) MICROSTRUCTURES FOR DRUG DELIVERY.....</b>	<b>41</b>
3.1 Implantable Drug Delivery Systems and the Advantages of PLGA.....	41
3.2 Design and Fabrication of the Prototype Drug Capsule .....	43
3.3 Experimental Results and Discussions .....	47
<b>CHAPTER 4. APPLICATIONS OF UV LITHOGRAPHY OF SU-8 IN FABRICATION OF 3D MICRO MIXER / REACTORS WITH ARRAYS OF IMPINGING MICRO JETS .....</b>	<b>52</b>
4.1 The Challenges in Micromixing and the State-of-the-Art in Design and Fabrication of Micro-mixers/Reactors .....	52
4.2 Design for the Three-Dimensional Micromixers/Reactors Based on Impinging Micro-jets.....	54

4.3	Fabrication of the Micro-mixer/Reactor .....	58
4.4	Experiments and Discussions .....	62
<b>CHAPTER 5. FABRICATION OF A NOVEL HYDRO-FOCUSING UNIT FOR MICRO FLOW CYTOMETRY USING UV LITHOGRAPHY OF SU-8 .....</b>		<b>69</b>
5.1	Basic Principle of Conventional Flow Cytometry and the Advantages of a Truly Three-Dimensional Hydrofocusing Unit .....	69
5.2	Design of the Three-dimensional Hydro-focusing Microfluidic Unit .....	71
5.3	Experiments and Discussions .....	80
<b>CHAPTER 6. OUT-OF-PLANE, FREE-SPACE, PREALIGNED REFRACTIVE MICRO-OPTIC COMPONENTS BASED ON UV LITHOGRAPHY OF SU-8 .....</b>		<b>86</b>
6.1	Out-of-Plane Micro-optic Components and the Advantages in Integrated Optical Systems .....	86
6.2	Principle of the Out-of-Plane Microlens and Microlens Array Fabricated Using Direct Lithography .....	89
6.3	Simulation for the Surface Formation of the Out-of-plane Microlens .....	91
6.4	Microfabrication Process and Results .....	101
<b>CHAPTER 7. MICROFABRICATION OF OPTIC FIBER BUNDLE COUPLER WITH INTEGRATED FOCUSING LENSES USING UV LITHOGRAPHY OF SU-8 .....</b>		<b>110</b>
7.1	Limitations of the Conventional Technologies and the Advantages of Integrated Fiber Coupler Fabricated Using Direct Lithography of SU-8 .....	110
7.2	Design of the Fiber Bundle Coupler and Tilted Lithography of SU-8 .....	112
7.3.1	Wavelength Selection and Refraction Compensation in Tilted Lithography .....	116
7.3.2	Microfabrication of Pre-aligned Fiber Bundle Coupler .....	118
7.4	Experimental Results and Discussions .....	121
<b>CHAPTER 8. A NEW TYPE OF NEGATIVE-TONE, UV LITHOGRAPHY PHOTORESIST BASED ON COMPOSITE OF EPON RESINS 165 AND 154 .....</b>		<b>128</b>
8.1	Introduction .....	128
8.2	Material and Lithography Properties of 154 .....	130
8.3	Material and Lithography Properties of 165 .....	133
8.4	Use the Composite of EPON Resins 154 and 165 in UV Resist for Optimal Lithography Properties .....	136
8.4.1	The Optical Properties of the Resist Based on EPON Resins 154 and 165 .....	137
8.4.2	Lithography Properties of Resist Based on EPON Resins 165 and 154 .....	140
8.4.3	Lithography Results and Discussions .....	144
8.5	Advantages of the New Resist and Discussions .....	149
<b>CHAPTER 9. CONCLUSIONS AND FUTURE WORK .....</b>		<b>151</b>

<b>REFERENCES</b>	.....158
<b>VITA</b>	.....169

## **ABSTRACT**

UV lithography of thick photoresist is widely used in microelectromechanical systems (MEMS) and micro-optoelectromechanical systems (MOEMS). SU-8 is a typical negative tone thick photoresist for micro systems, and can be used for both structural material and pattern transfer.

This dissertation presents an effort to comprehensively study these important subjects. The first part, and the most fundamental part of this dissertation concentrated on the numerical analysis and experimental study of the wavelength dependent absorbance of SU-8 and the diffraction effects on the sidewall profiles of the microstructures made using UV lithography of SU-8. This study has laid the foundation for all the designs and analysis for the BioMEMS and Micro-optic components and systems using UV lithography of SU-8 in the following chapters of the dissertation.

After a full discussion of UV lithography of SU-8, the applications of SU-8 in BioMEMS and micro optics were presented in the following areas: 1) design, analysis, and molding fabrication of biodegradable PLGA microstructures for implanted drug delivery application; 2) design, fabrication, and test of a novel three-dimensional micro mixer/reactor based on arrays of spatially impinging micro-jets; 3) design, analysis, fabrication, and test of a novel new type of truly three-dimensional hydro-focusing unit for flow cytometry applications based on SU-8; 4) Study on a new technology to fabricate out-of-plane pre-aligned microlens and microlens array, and the application of the microlens in a fiber bundle coupler.

Finally, a new negative tone thick photoresist based on the composition of EPON resins 165 and 154 were introduced. The synthesis, physical properties, and UV-lithography properties

of this new photoresist have been completed. The experimental results have proved it can be a better alternative to SU-8 and can be used in various MEMS and MOEMS applications.

Most of the contents have been published or accepted for publications in technical journals or international conferences. Two US patent applications are pending and two more disclosures have been filed for the new technologies presented in this dissertation. There are obviously more work to be done in this promising area and these are presented in the section for future work.



# CHAPTER 1. INTRODUCTION

Thick photoresists, such as SU-8, PMMA, are widely used in Micro ElectroMechanical Systems (MEMS), micro-optoelectromechanical systems (MOEMS), and biological-microelectromechanical systems (BioMEMS). These photoresists play important roles in the pattern transferring or serving as the structure materials. In BioMEMS and MOEMS, these thick photoresists can be directly used to form the basic micro fluidic channels, mixing components, separation components, optical detection components, etc; they may also be used as templates to transfer the designed patterns to metal molding inserts for low cost duplication of microchips for BioMEMS and micro-optics applications.

Although X-ray lithography of methyl methacrylate (PMMA) or SU-8 can meet these requirements, the expensive beamlines are not readily available for many researchers. The high cost of x-ray lithography also made it impractical for many applications. As a cheaper alternative, UV lithography of SU-8 received wide attentions in the last few years. As the obtainable results with UV lithography of SU-8 get better and better, ever-wider applications have been found for the technology in BioMEMS and micro-optical systems.

SU-8 resist is a negative tone, epoxy-type photoresist based on EPON™ SU-8 (also called EPIKOTE™ 157) epoxy resin from Hexion Specialty Chemicals, Inc. (Columbus, OH 43215), and originally developed and patented by IBM [1-5]. It is commercially available from MicroChem Corp. (Newton, Massachusetts). SU-8 epoxy is solved in standard gamma-butyrolactone (GBL) solvent, which can be replaced by cyclopentanone and has improved properties. The solution is then mixed with photo initiator to obtain the photosensitivity. Due to its low optical absorption in the near-UV range, SU-8 can be lithographed in thickness of

hundreds, or thousands of micrometers with very high-aspect-ratios using standard contact Ultra-Violet (UV) lithography equipment. SU-8 can also be patterned using X-ray or E-beam. Cross-linked SU-8 has good chemical and physical properties and can serve as excellent structural material for many applications [6-13]. For SU-8's near-UV contact printing, normally broadband near UV light between 320nm~450nm is used for the exposure. With well controlled the lithography conditions, with pressure contact exposure or vacuum contact exposure, cross-linked polymer microstructures with high-aspect-ratios more than 100 and the heights more than 1000  $\mu\text{m}$  could be obtained [14-20].

Though widely used in the MEMS field, there has been no research work to comprehensively study the ultraviolet (UV) lithography of the ultra-thick SU-8 resist analytically and experimentally. For example, detailed study on the wavelength dependence of the sidewall profiles, understanding of the air gap effects on the projection images as the light wave penetrates the resist and absorbed, have not been reported in the field.

The research work on UV lithography of ultra thick SU-8 resist will be presented first, followed by the numerical modeling and analysis of UV lithography, and finally presentation of optimal UV lithography conditions and some processing tips [21]. Some applications of UV lithography of ultra-thick SU-8 resist in BioMEMS will also be presented, such as using SU-8 mould to pattern biodegradable material PLGA for drug delivery [22, 23], and three-dimensional micro mixer/reactor based on array of micro impinge jets [24], three-dimensional hydrofocusing unit for micro flow cytometry [25]. Finally, the applications in micro-optics, such as the out-of-plane pre-aligned polymer refractive microlens and microlens array will be demonstrated in detail with discussions of their potential applications in optical communication and optical detection system [26-31].

Chapter 3 will present the research effort to microfabricate high aspect-ratio microstructures of PLGA with the help of SU-8 resist and possible applications in implantable drug delivery [22, 23]. Using biodegradable polymers for implantable drug delivery purposes has been a very important research area and in medical practice for many years. Polymers, such as PLGA, have been the most attractive one because they do not require removal after the drug has been released. The prototypes of capsule packaged with sample species have been made and tested. The preliminary results approve the feasibility to make bio-degradable PLGA capsule with linear drug release.

Chapter 4 will present a novel micro-mixer/reactor based on arrays of spatially impinging micro-jets fabricated by 3D lithography of SU-8 resist [24]. Using the impinging plumes from two opposite arrays of micro-nozzles, the interfacial contact in the mixing chamber was significantly boosted. This effect has effectively increased the mixing efficiency. The experimental results of the prototype mixers have proved the high mixing efficiency with a pressure drop of about 200 Pa. This micro-mixer/reactor can be easily integrated with other micro-fluidic components and used in various bio-chemical, biological or chemical systems.

Chapter 5 covers the research work on a truly three-dimensional (3D) hydro-focusing cell sorter in micro-flow cytometry applications [25]. The unit was microfabricated by means of three-dimensional lithography of SU-8. The three-dimensional microstructure for coaxial sheathing was designed, microfabricated, and tested. Three-dimensional hydro-focusing capability was demonstrated with experiments to sort labeled tanned sheep erythrocytes (red blood cells). This SU-8 polymer hydro-focusing microstructure can be easily batch-fabricated and integrated with other polymer microfluidic components for construction of total analysis systems ( $\mu$ TAS).

Chapter 6 presents a research work to design, fabricate, and test a new type of polymer microlens and microlens array using direct lithograph of SU-8 resist [26-31]. These microlenses have many potential applications in optical communication and optical detection systems. To develop integrated free-space micro optical systems, out-of-plane microlenses with the principal plane perpendicular to the plane of the substrate are necessary. Most of the reported microlenses in the literature are either in plane or hinged lenses fabricated in surface technologies then driven up to the required vertical position electrostatically or electromagnetically. This microlens and microlens array presented here do not require any assembly process or external driving forces, and have quasi-ball/spherical surface profile in the paraxial area. Lenses with different dimensions, focus pads, focal length, and numerical aperture can be obtained. In this chapter, the working and fabrication principles of this type of out-of-plane microlenses, the numerical simulations for fabrication and optical functions, fabrication process, and the experimental results are presented.

Chapter 7 describes the design, microfabrication and testing of a pre-aligned array of fiber couplers using direct UV lithography of SU-8 with potential application in optical communication [29]. This fiber coupler array includes an out-of-plane refractive microlens array and two fiberport collimator arrays. With the optical axis of the pixels parallel to the substrate, each pixel of the microlens array can be pre-aligned with the corresponding pixels of the fiberport collimator array as defined by the lithography mask design. This out-of-plane polymer microlens array is pre-aligned with the fiber collimator arrays with no additional adjustment and assembly required. This integrated design and fabrication may help to dramatically reduce the running cost and improve the alignment quality and coupling efficiency. In addition, the latest research effort to develop a new type of the fiber bundle coupler with a pair of microlens arrays

integrated instead of just one lens array, with improved coupling efficiency, will also be presented.

Chapter 8 covers the development of a new type of resist for high aspect ratio microstructures and devices. Though widely used with demonstrated good lithography properties, SU-8 has some limitations. It shows some significant surface flatness errors when thick resist layer is spin-coated, resulting in large diffraction related lithography errors. It also has debonding problems with some commonly used substrate materials, such as commonly used glass. Research work has also been conducted to develop a new type photoresist that has similar lithography properties, but much better surface flatness and stronger adhesion and less micro-cracking problems. It is based on composite of the EPON™ resin 154 and EPON™ resin 165. Both of these components are solved into gamma-butyrolactone (GBL) solvent with photo initiator. This new photoresist has excellent surface wetting properties, which can self-planarize in the pre-baking processing. With excellent adhesion property, lower internal stress, and less cracks in the corners of microstructures, this new type of negative tone photoresist shows superior properties in UV project and contact lithography. Without any pre-clean processing for the substrate surfaces, the photoresist has excellent adhesion on all types of substrate surfaces in commonly used MEMS applications. In addition, the cured polymer of the photoresist composition also has better material properties than SU-8. It has significant potentials to replace SU-8 photoresist as a better choice for UV lithographed thick photoresist.

Chapter 9 covers the conclusions and the future work. In addition to presentation of the major research conclusions, two major areas of the future work are also presented: one for continuous work to improve the performances of the fiber coupler, and the other is in the area of microlens fabrication. They represent the areas that may require some future research efforts, and at the same time may have potentially industrial applications.

## **CHAPTER 2. UV LITHOGRAPHY OF ULTRA THICK SU-8 PHOTORESIST**

### **2.1 Review of the State-of-the-Art for UV-Lithography of SU-8**

Ultraviolet (UV) lithography of ultra-thick photoresist with high-aspect-ratio, high sidewall quality, and good dimensional control is very important for microelectromechanical systems (MEMS) and micro-optoelectromechanical systems (MOEMS) [1, 2, 4, 5, 8, 15-17, 19, 20, 24-27, 29-31]. Although X-ray lithography of poly methyl methacrylate (PMMA) or SU-8 can meet these requirements, the expensive beamlines are not readily available for many labs and companies. The high cost of x-ray lithography also made it not practical for many applications. As a cheaper alternative, UV lithography of SU-8 received wide attentions in the last few years. As the obtainable results with UV lithography of SU-8 get better and better, ever-wider applications have been found for the technology in MEMS and MOEMS [15-17, 19, 20, 24-27, 29-31].

The un-polymerized SU-8 has a glass temperature 50~60°C [32], the cured SU-8 has glass temperature higher than 220°C [32]. The thermal set temperature for SU-8 resist is about 140°C, the pre-bake temperature on hot plate therefore needs to be lower than 130°C. When post-bake at 95°C after exposure, the polymer shrinkage in generally is at 7.5% [33]. The cured SU-8 polymer has a Young's modulus around 4.0~4.5 GPA, Poisson ratio around 0.22, film stress around 16~19Mpa, friction coefficient around 0.19 with 10g load [2, 8, 14, 34]. The cured SU-8 polymer has a relative dielectric constant around 4 [35]. The cured SU-8 also has very good chemical resistance and shows a very slow etching rate for most chemicals. The adhesion strength of SU-8 in most cases depends on the substrate materials. In general, SU-8 has very good adhesion with Ti, Au, and Cr, but less with Cu and Ni [36]. The SU-8 adhesion on Si wafer

with native oxide is good. The SU-8 has good biocompatibility and can be used for PCR and cell culture [37-39]. The fully cured SU-8 is very difficult to reflow even at 230°C (above its glass temperature) and it changes color and turns black at this temperature.

Normally, SU-8 microstructures with aspect ratio less than 1:30 can be obtained easily in UV lithography. In this chapter, SU-8 microstructures with aspect-ratio more than 1:100, even 1:190, will be demonstrated [21]. The SU-8 microstructures more than 2mm high will also be presented [21].

In the following sections of the chapter, the recent development in SU-8 lithography of ultra thick SU-8 resist will be presented first, followed by a summary of optimal UV lithography conditions and some processing tips.

## **2.2 Basic Steps for UV Lithography of SU-8 and Some Processing Tips**

The standard processing procedure for UV lithography of SU-8 includes: 1) pre-treat the substrate, spin-coat SU-8; 2) pre exposure bake, UV exposure (320-450nm); 3) post exposure bake; and 4) development. The process parameters determine the final quality of the microstructures. The curing process of SU-8 completes in two steps: formation of acid during optical exposure and thermal epoxy cross-linking during the post exposure bake. A flood exposure or controlled hard bake is recommended to further cross-link the exposed SU-8 microstructures if they are going to be used as parts of the final products. Because most of the publications in the field do not provide detailed lithography conditions, starters often have to learn from their own experiences and the learning curve some time can be exceptionally long. The data sheet provided by MicroChem Corp., the vendor of SU-8 is a reasonably good information source. However, the processing conditions are highly dependent on the specific equipment available. The following processing steps and conditions are what have been proved

effective for the cleanroom facility in the Center for Advanced Microstructures and Devices (CAMD) of LSU.

### **2.2.1 Pre-treatment of the Substrate**

To obtain good adhesion for SU-8, the substrate needs to be cleaned with acetone, IPA, and DI water sequentially and then dehydrated at 120°C for 5~10 minutes on a hot-plate. The substrate may also be primed using plasma asher immediately before spin-coating resist. In addition, adhesion promoter may also be used as needed. For the applications involving electroplating metals/alloys and stripping of cured SU-8, the vendor of SU-8, MicroChem, recommends using OmniCoat before coating of SU-8.

### **2.2.2 Spin Coat of SU-8**

The thickness of SU-8 film is dependent on several factors: viscosity of SU-8 used, spin speed, and total number of turns. The vendor of the SU-8, MicroChem Inc., provides some spin-coating curves for different SU-8 formulations, such as SU-8 5, SU-8 50, and SU-100. Some research labs have also developed their own spin-coat curves based on the particular equipment used and spin acceleration profile. Figure 2.1 shows the some typical spin-coating curves of SU-8 calibrated in the CAMD cleanroom. Additional information may be found from product catalogues of MicroChem Inc.

Bubbles formed during spin-coating step may lead to reduced lithography quality. To eliminate bubbles in resist film, the SU-8 should be poured directly from the bottle as close to substrate as possible. The substrate can be placed on a flat and horizontal plate for 2~10 hours before prebake. To avoid introduction of particles into the SU-8 film, the mouth of the bottle needs to be cleaned with wipe absorbing acetone before and after pouring the SU-8 resist. This is an easy but especially critical step for obtaining good quality of thick SU-8 film.



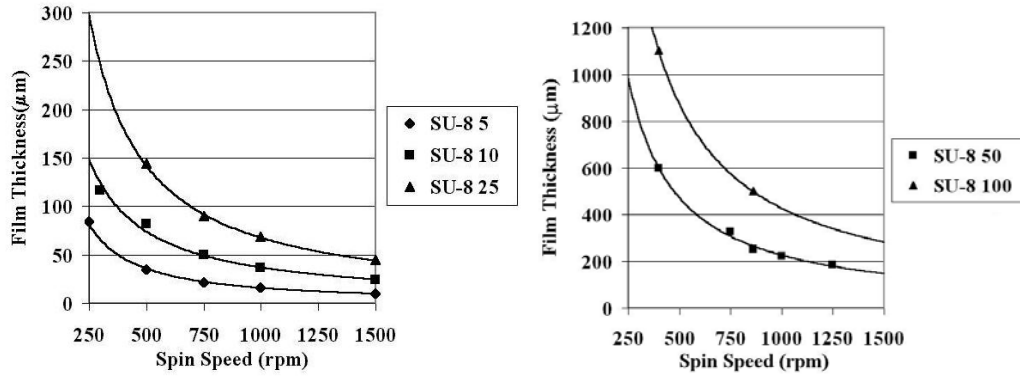


Figure 2.1. SU-8 spin-speed vs. film thickness curve in CAMD cleanroom

### 2.2.3 Soft Bake

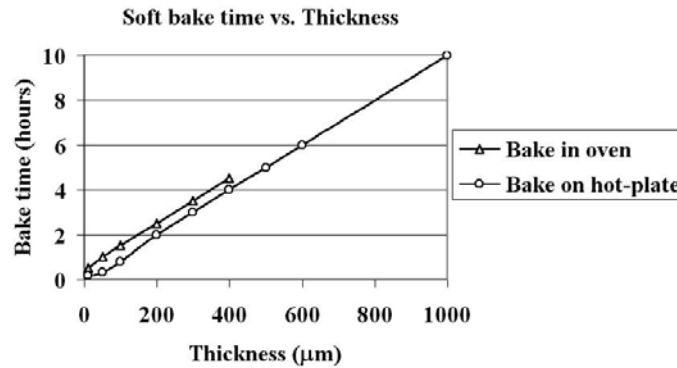


Figure 2.2. Soft bake time vs. SU-8 thickness

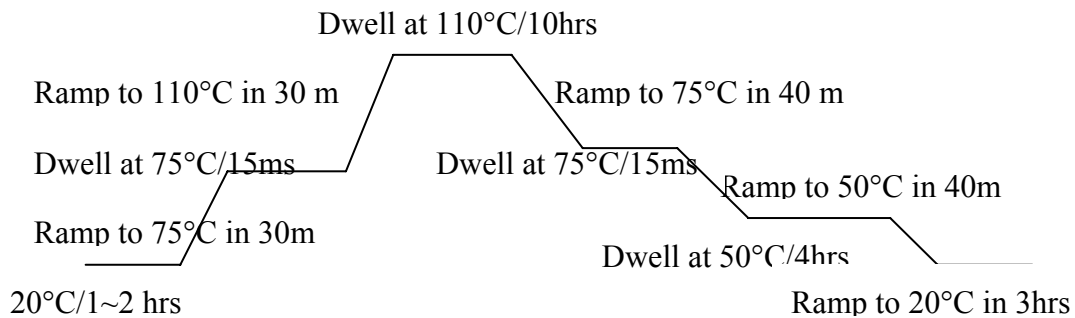


Figure 2.3. A selected soft bake profile for 1100  $\mu\text{m}$  thick SU-8 film

The spin-coated sample needs to be soft baked to evaporate the solvent on a leveled hot plate or convection ovens. The heat transfer condition and ventilation are different for the hot

plate and the convection ovens, the preferred soft baking times are therefore different as shown by the curves for measured soft baking times in Figure 2.2. Ramping and stepping the soft bake temperature are often recommended for better lithography results. The glass temperature of the un-exposed SU-8 photoresist is about 50~60°C. Figure 2.3 shows a typical soft baking temperature curve used in CAMD cleanroom. This soft bake process consists of multiple steps of ramping up, dwell, and ramping down. The total cooling down time is about 8~10 hours for a 1000  $\mu\text{m}$  thick SU-8 resist. For ultra thick SU-8 film (more than 1000  $\mu\text{m}$  thick), bake temperature at 110°C is used as shown in Figure 2.3. To improve the adhesion of the SU-8 film on substrate coated with Cr/Au film (as commonly used in UV-LIGA process as plating seed layer), 110°C bake temperature is suggested instead of 96°C. At the same time, the bake time should be slightly reduced.

#### **2.2.4 Exposure**

Near UV (320-450nm) light source is normally used for lithography of SU-8. As the wavelength of the light source increases, the absorbance of the light reduces and the transmission increases significantly. The transmission increases from 6% at  $\lambda=365\text{nm}$  to about 58% as the wavelength increases to 405nm. SU-8 has high absorption for wavelength less than 350nm, but is almost transparent and has very low absorption for wavelengths of above 400nm. Because of the high absorption of SU-8 for light with shorter wavelengths, light source dominated by shorter wavelength components often results in over exposure at the surface of the resist and under exposure at the bottom part of the resist layer. This is the main reason that UV lithography of SU using *i*-line dominated light source tends to produce microstructures with T-topping geometric distortions. Thickness of the resist is another key parameter that dictates the required dosage of the exposure. Figure 2.4 shows two curves of required exposure dosage and the thickness of SU-

8. The vendor of SU-8, MicroChem Inc., advises to filter out the light with wavelength lower than 350nm to improve lithography quality. After removing the light components with wavelength less than 350nm, for the Oriel UV station with spectrum as shown in Figure 2.11 in CAMD of LSU, the total exposure dosage ratio between of *i*-line and *h*-line are kept in 1:7 ~1:10 to achieve perfect vertical sidewall, especially for the SU-8 resist with thickness around 1mm. This can be validated by the results of both ZEMAX simulation for exposure and our experiments. For lithography of very thick resist, multiple exposures are required to avoid over heating, scattering and diffusion on the surface of the resist. Typically exposures need to be separated in 20 seconds (or less than 400mJ/cm<sup>2</sup> per time) intervals with 60 seconds waiting period in between. For highly reflective substrate, the effect of the reflection needs to be taken into account in estimation of the total exposure time.

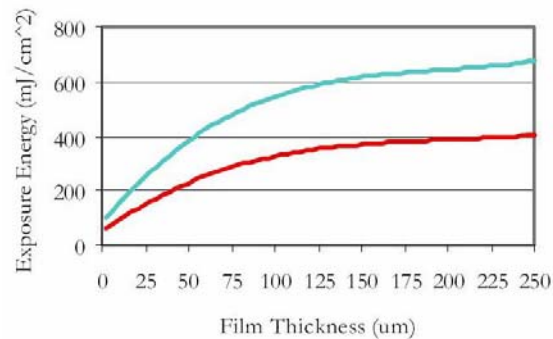


Figure 2.4. SU-8 Exposure dosage vs. film thickness: the exposure dosage is inside the region between the blue and red lines. (Needs permission from MicroChem Inc.)

### 2.2.5 Post Exposure Bake (PEB)

Post exposure bake (PEB) is performed to cross-link the exposed regions of the SU-8 resist. The cross-link, or the curing step of SU-8, can be achieved at room temperature. Post bake at raised temperature helps to accelerate the polymerization process. Figure 2.5 shows a typical PEB temperature profile. For resist thickness up to a few hundreds micrometers, post bake at 96°C for 15~20 minutes is required either on a hot plate or in a convection oven. SU-8's cross-

link process may cause significant residual stress, which may cause cracks or de-bonding. In order to minimize residual stresses, wafer bowing, and cracking, rapid cooling down from the PEB temperature should be avoided. For resist films with thickness more than 1000 micrometers, to ramp the PEB temperature down from 96°C should take more than eight hours. Another possible way to reduce post bake stress is to use lower PEB temperature, such as 50°C or 55°C, but longer baking time. This method would result in much lower thermal stress in comparison with using 96°C PEB temperature.

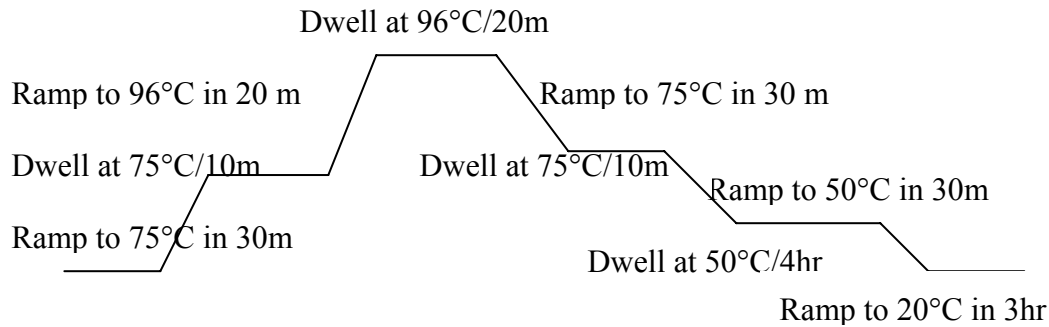


Figure 2.5. A possible temperature profile to be followed in PEB for 1100µm thick SU-8 film

### 2.2.6 Development

After exposure and post bake, the sample is then developed using SU-8 developer. Recommended develop times can be found from the catalogue provided by the vendor of SU-8 or your lab's experiment data. Development process can be optimized based on the experiment's agitation rate, develop temperature, and SU-8 resist processing conditions. After the sample is developed by SU-8 developer, it is rinsed using fresh SU-8 developer for several time, then rinse with isopropyl alcohol (IPA) for 3~5 minutes. If there are white spots produced inside the IPA, it means the SU-8 is underdeveloped. The sample needs to be immersed into SU-8 developer or spring with fresh SU-8 developer to further development. After the sample is completely developed, the sample needs to be rinsed using fresh IPA. Our experiments show that the surface

of prebaked SU-8 film seems to be damaged when it was placed into water, either because of dissolve or some chemical reactions, rinse with De-ionized (DI) water should be avoided. Finally, the sample is dried naturally or by nitrogen gas blow.

Development of thick SU-8 film is a challenge in fabrication of high-aspect-ratio microstructures. The SU-8 developer cannot effectively work in ultra deep and narrow structures by simple diffusion and conventional stirring mechanism. The development may last hours, damage the fine structures, and often is incomplete. Strong agitation is normally used to completely develop the SU-8. However, the strong stirring process or supersonic vibration often produces vibrations in random directions and cause severe vibrations of the microstructures. They may also reduce the sidewall quality, deform or de-bond some fine patterns, and destroy the high-aspect-ratio microstructures.

For high aspect ratio microstructure, one direction agitation may be necessary to accelerate the development process but avoid destroying the microstructures. Normally, the agitation direction should parallel with growth direction of the microstructure. The agitation can be gravity [40] or megasonics [41]. With gravity as the agitation force, the substrate can be face down and immersed into the SU-8 developer. With megasonics as the agitation force, the substrate can face to or back to the megasonics actuators.

In contact lithography, the light source is projected in perpendicular to the substrate. With no external agitation, the un-exposed SU-8 is developed from the top layer to the bottom layer and is based on diffusion of the SU-8 developer solution. If the direction of the agitation force is perpendicular to the substrate (parallel with the sidewall of the microstructures), the agitation would accelerate the development speed but not effect the sidewall quality or minimize the possibility to damage the microstructures. There are two methods to accelerate the development

process. One is to immerse the sample in a face-down orientation to take advantage of the gravity force for better convective transport. Another method is to use a megasonics agitation in perpendicular with the substrate.

The mechanism of SU-8 development should be understood in the following way: when the SU-8 developer enters the un-crosslinked SU-8, a porridge-like region is produced between the SU-8 and the developer. Inside this porridge-like region, as the developer diffuses, the un-cross-linked SU-8 dissolves into the SU-8 developer. The concentration of un-crosslinked SU-8 is non-uniformly distributed. The concentration decreases as it is closer to the boundary line between the dissolved and the solid section of the un-crosslinked SU-8. With the sample positioned in a face-down orientation, the diffusion and removal of the dissolved SU-8 from the boundary region of the developer and the un-crosslinked SU-8 were accelerated by gravity force. This may help to achieve a much higher development rate based on our experience. Our experiments have proved that the development rate for face-down oriented samples can be at least two times of that obtained when the samples were placed in a face-up orientation. SU-8 microstructures' edges and trenches were also found to be much cleaner after the development.

With megasonic agitation when the wave propagates is in the perpendicular to the substrate, much faster development rates can also be achieved. Our experiments also found that excellent uniformity of development can also be realized. This technique is commonly used in x-ray LIGA processes and has been reported to work well with SU-8. In megasonic agitated development, the range of frequencies is normally in several Mhz. These reduced wavelengths help to agitate the fluids in the porridge-like region between the un-crosslinking SU-8 and the SU-8 developer. This leads to higher dissolved speed and faster development.

### **2.2.7 Treatment of Flood Exposure and Extra Hard Bake**

When the SU-8 is used as structural material, flood exposure and extra hard bake may be needed to fully cross-link SU-8. The flood exposure may be two or three times more than normal exposure dosage in some cases. The hard bake temperature may range from 150°C (higher than the thermal set temperature) to 200°C (lower than the glass temperature of cured SU-8). The variation of temperature profile and baking time is dependent on the structure and thickness.

### **2.2.8 Removing of Cured SU-8**

There are many methods to remove the cured SU-8 polymer. One way is to use the Omnicoat adhesion/release layer provided by SU-8 vendor, MicroChem Corp. To remove cured SU-8 with Omnicoat release layer, immerse the substrates into the Remover PG bath at 50-80°C for 30-90 minutes [42].

Dynasolv from Dynaloy Inc. also can be used as the SU-8 stripper to remove SU-8 easily [43].

If the structures on which the remaining cured SU-8 need to be removed can sustain high temperature, the cured SU-8 can be ashed with hot air flow at 600°C, then the residues on the structure can be clean by ultrasonic [44].

RIE [45], laser ablation [46], salt bath [45], etc. also can be use to remove the residues.

## **2.3 Study of Diffraction Compensation and Wavelength Selection in Lithography**

To achieve high quality microstructure with expected sidewall profile, dimensional control, and high-aspect-rate with UV lithography of ultra thick SU-8, several important parameters need to be carefully controlled: temperature profile in pre-bake and post-bake, Fresnel diffraction and wavelength-dependent absorption in exposure, and development

parameters. Among these parameters, the effects of absorption spectrum and the diffraction on the lithography quality are two key factors to decide the aerial image and limit the sidewall quality of UV lithography of ultra thick SU-8 resist. They will be the major topics in this chapter.

### **2.3.1 Diffraction Caused by Air Gap and Wavelength Dependence of UV Absorption Rate of SU-8**

SU-8 in general has excellent surface planarizing property. However, as the thickness of SU-8 resist increases, the non-uniformity of the resist can become a serious issue. To fabricate ultra thick, high-aspect-ratio microstructures, spin-coated resist layers ranging from several hundreds to thousand micrometers are commonly required. In such cases, high viscosity SU-8, such as SU-8 50 or SU-8 100, is always preferred. The surface flatness can be a very severe problem, with typical flatness errors to be 10  $\mu\text{m}$  to 100  $\mu\text{m}$ . Other factors such as unintentional tilt in baking process, dirt particles, curvatures of the substrate or mask, etc, may also contribute to the reduced surface flatness. The flatness error then forms air gaps between the mask and resist surface, and results in serious diffraction, aerial image distortion, and printing errors.

For the ultra thick photoresist, the absorption of the resist to the light source also greatly affects the lithography quality. As the light beam penetrates the SU-8 resist layer from the top to the bottom, the light intensity drops gradually as the light is absorbed. The top part of SU-8 resist therefore absorbs higher dosage than the bottom part does. There are therefore over-dosage at the top and under-dosage at the bottom. This is one of the major reasons that an inexperienced operator often produces mushroom types of microstructures in UV lithography of SU-8. It is also one of the reasons X-ray lithography is normally preferred for high quality vertical sidewall and high-aspect-ratio structure. The extremely high transmission of X-ray beamline helps to provide about the same absorptions across the entire thickness of photoresist.

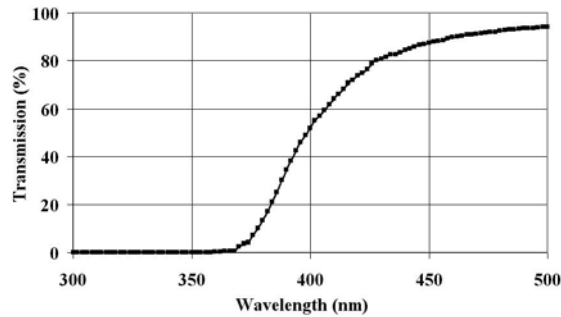


The absorption spectrum of unexposed SU-8 resist shows much higher absorbance at shorter wavelengths than at long wavelengths. Figure 2.6(A) shows the transmission spectrum of 1mm thick unexposed SU-8 100, a thickness close to what was used in our experimental study as will be presented in the later sections. The absorption coefficient of unexposed SU-8 at 365nm (where the photo-resist is the most sensitive) is about 4 times of the absorption coefficient at 405nm. The shorter wavelength components of light are primarily absorbed by the surface layer while the longer wavelength components penetrate further down and expose the bottom part. It is therefore desirable to filter out the wavelengths around and shorter than 365nm to avoid over-exposure at the top layer. Longer wavelengths (either *h* line or *g* line) with much lower absorbance are used to permit more energy to reach the bottom part of the thick SU-8 resist layer and to achieve better sidewall profiles. Figure 2.6(B) shows the measured refractive index of SU-8 as function of the wavelength.

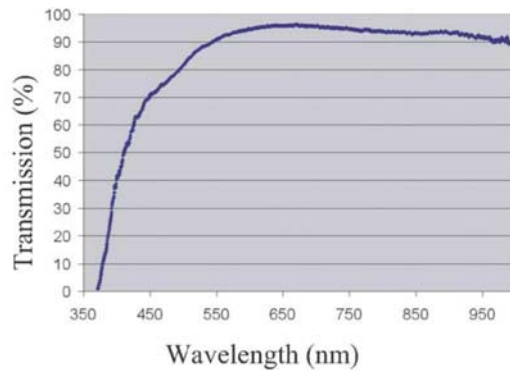
The absorption coefficient of unexposed SU-8 at 436nm is about 1/3 of that at 405nm and 1/12 of that at 365nm. Light source with primarily *g*-line component may therefore be suitable to expose ultra thick SU-8 resist. Sidewall quality using *g*-line exposure may also be much better than using 365nm, also better than using 405nm. Of course, the diffraction effect may become more serious with longer wavelength.

For ultra thick SU-8 lithography, there are several important parameters to be carefully controlled: temperature in pre-bake and post-bake, diffraction and wavelength-dependent absorption in exposure, development processing, etc. Normally, optimization of the temperature control in pre-bake and post-bake can minimize the stress of the SU-8 and reduce the possibility of de-bonding; the diffraction and photoresist's absorption cause the aerial image shape to be degraded and the light intensity distribution changed in the cross-section of light beam along the

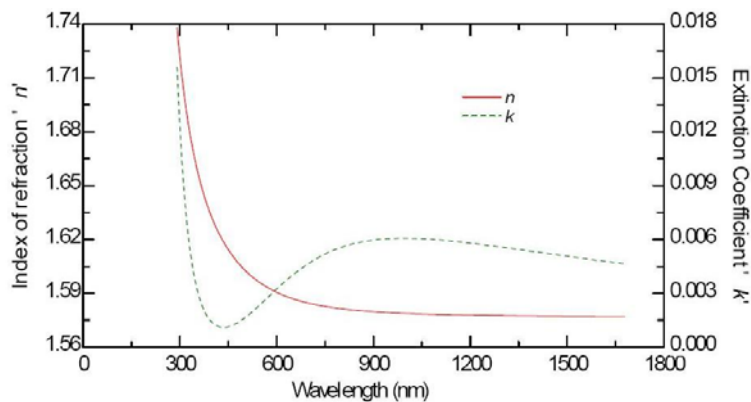
propagation direction; optimization of the exposure dosage helps to obtain enough dosage for the bottom part of SU-8 to improve the adhesion and avoid over exposure for the top part.



(A). Transmission of 1mm thick un-exposed SU-8 film.

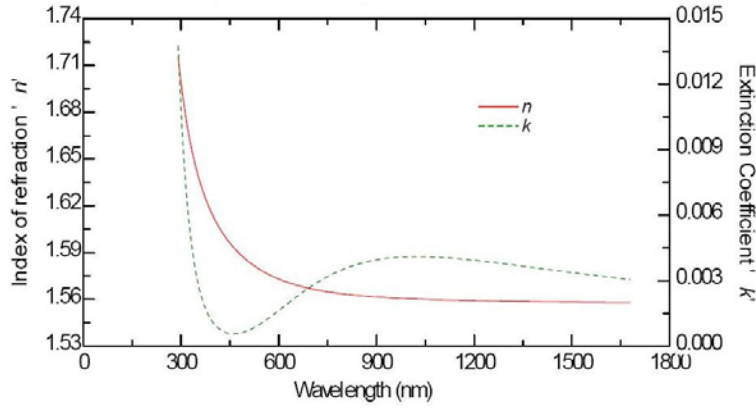


(B) Transmission of cured 1.1mm thick SU-8 film which was pre-baked at 110°C for 13 hours and then cooled down to room temperature in 8 hours, exposed with 2 J/cm<sup>2</sup> dosages, post-baked at 110°C for 30 min, then ramped down to room temperature in 8 hours. The sample was then de-bonded from the glass wafer and tested.



(C). Refractive index of un-exposed SU-8 vs. wavelength.

Figure 2.7 Optical Properties of SU-8. Results in Figures (A) and (B) were measured in our lab with Ocean Optics' S2000 spectrometer; Results in Figures (C) and (D) were measured by Mr. Ron Synowicki in J.A. Woollam Co., Inc. with M-2000 spectroscopic ellipsometer. (Figure continued.)



(D) Optical constant vs. wavelength for cured SU-8 polymer. The SU-8 film is about 3 $\mu$ m thick, exposed with 50mJ/cm<sup>2</sup> dosages, and post-baked at 96°C for 20 min.

### 2.3.2 Numerical Analysis of Diffraction and the Absorptions Spectrum on UV Lithography of Ultra Thick SU-8 Resist

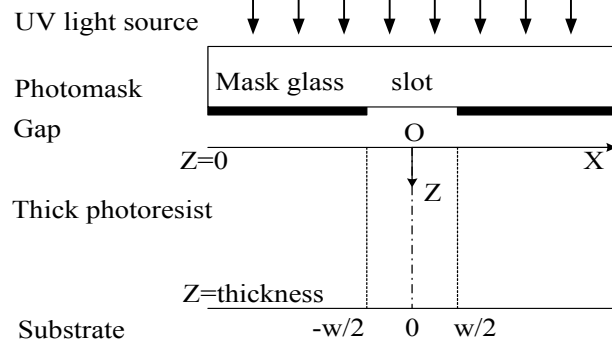
As collimated light passes through an aperture on the mask in UV exposure, diffraction happens because of the mask patterns' limitation for light wavefront. In lithography, the collimated light source can be considered as infinitely far away, but the mask patterns (i.e., diffracting apertures) are so close to the photoresist (observing screen) that the curvature of the wavefront becomes significant.

Based on the Huygens' principle, the diffraction produced by an aperture with arbitrary shape in an otherwise opaque partition can be stated by Fresnel-Kirchhoff integral formula:

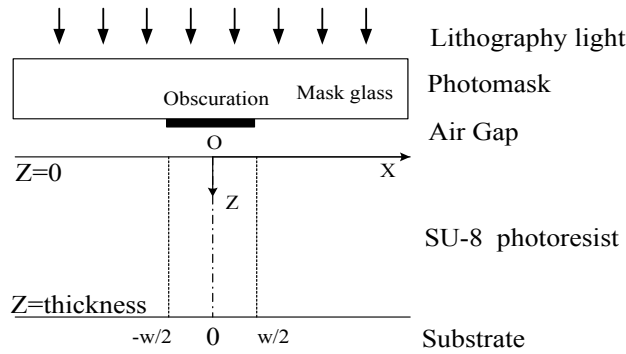
$$U_p = -\frac{ikU_0e^{-i\omega t}}{4\pi} \iint \frac{e^{ik(r+r_0)}}{rr_0} [\cos(n,r) - \cos(n,r_0)] ds, \quad (2.1)$$

where  $k=2\pi/\lambda$ ,  $\lambda$  is the incident light wavelength,  $U_0$  represents spherical monochromatic source waves,  $r$  and  $r_0$  stands for positions of a point on the aperture relative to the screen and the source respectively,  $(n, r)$  and  $(n, r_0)$  denote the angles between the vectors and the normal to the surface of integration,  $ds$  represents the integration on the surface of the aperture.

To better understand UV-lithography of SU-8 and its effects on sidewall profiles, numerical simulations were conducted with commercial software ZEMAX EE (ZEMAX Development Corporation, San Diego, CA, USA). This software, based on the principle of diffraction as stated in Equations (2.1), can be used to perform diffraction simulations in relation to UV-lithography of SU-8 resist. Light intensity distribution data were exported from ZEMAX and imported to Excel or Sigma Plot. The effect of the substrate reflectivity (such as silicon substrate, about 0.575 for vertical incident light with a wavelength of 365nm, and 0.473 for a wavelength of 405nm) was considered in the numerical simulations.



(A)



(B)

Figure 2.8. (A) A slot pattern and (B) an obscuration pattern on a photomask

Using ZEMAX EE software, numerical simulations were conducted for two different cases: 1) with air gap between the mask and wafer and no compensation; and 2) using glycerin liquid compensation. In all the simulations, the slot on mask was assumed to be 20 $\mu\text{m}$  wide and infinitely long as shown in Figure 2.8. The ideal distribution of the light intensity without any diffraction effect (entering the slot) is plotted as uniformly distribution.

Numerical simulations were conducted to study the effects of diffraction caused by the air gap, the diffraction compensation effects using optical liquid, such as glycerin or other optical liquids. In the simulations, the gaps between the mask and resist surface were assumed to be 50  $\mu\text{m}$ , and the slot was assumed to be at 20  $\mu\text{m}$ . The simulation results are presented in Figure 2.10, which shows the light intensity distributions at the surface of the SU-8 resist. It can be seen that with gap compensation using glycerin produced improved intensity distribution than that with air gap.

Since SU-8 is a negative tone resist, the pattern profile is defined by the light intensity higher than the threshold energy to cure SU-8 within the targeted region. With the attenuation of intensity in SU-8 along the vertical direction (Z direction) and diffraction caused by the micro patterns, the aerial dimension of the projection image is varied. The edges of the aerial image are defined as the edges of diffraction pattern with energy higher than the cross-link dosage.

The light intensity along the vertical direction is

$$I = I_0 \cdot e^{-aZ}, \quad (4)$$

where  $a$  is the absorption coefficient,  $z$  is the distance in vertical direction from the film's surface. The transmission is then

$$T = I / I_0 = e^{-aZ}. \quad (5)$$

Figure 2.9 shows measured transmission for un-exposed SU-8 with different thickness. As can be seen from the results in Figure 2.9, the intensity of *i*-line light decayed much faster than *h*-line as light penetrates deeper into the resist. The absorption coefficient is found to be about 0.0031 for *i*-line and about 0.0005 for *h*-line. The measured data presented in Figure 2.9 were used in numerical simulations for combined effect of wavelength dependence of the absorption of unexposed SU-8 and the diffraction. Similarly, a 20  $\mu\text{m}$  opening slot on the mask is assumed. Two different wavelengths *i*-line and *h*-line were considered separately. Numerical simulations were conducted to obtain the diffraction pattern at the bottom of the resist layer.

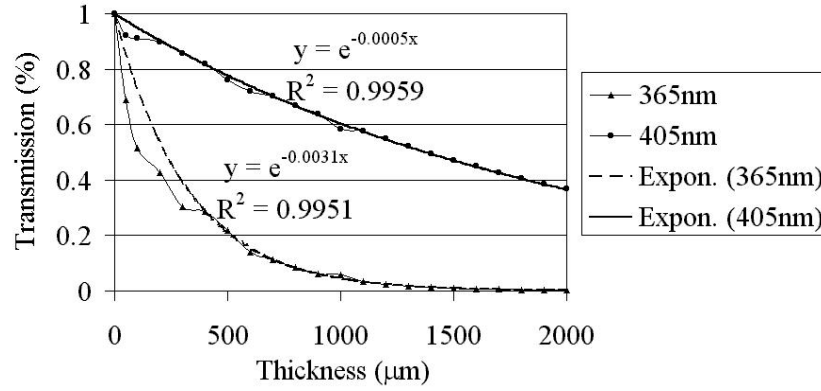
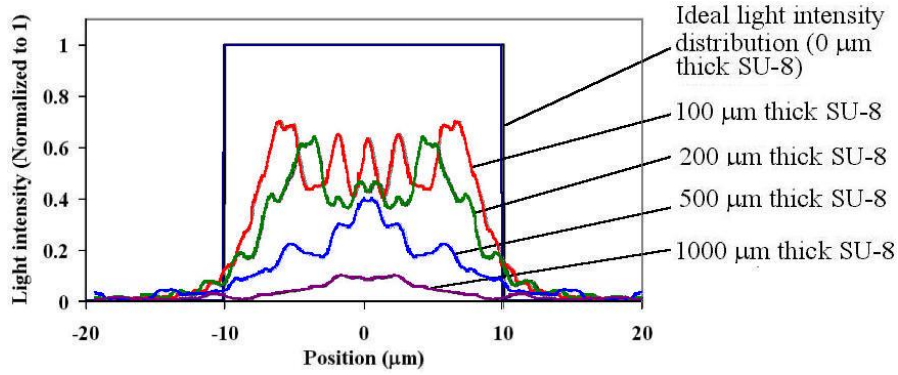


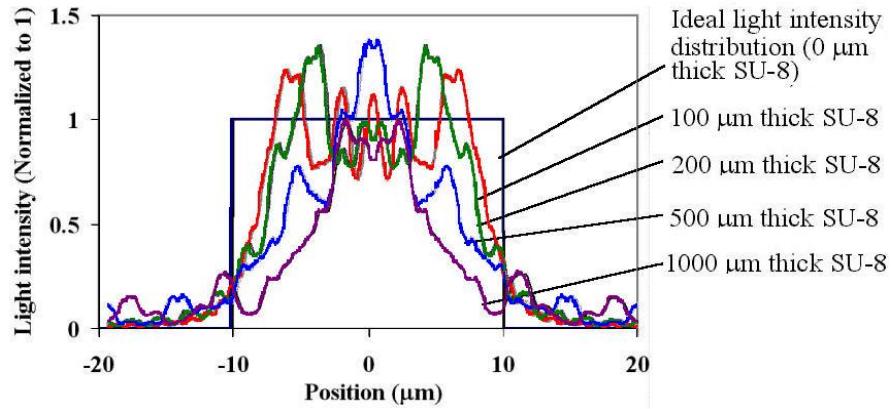
Figure 2.9 Measured transmissions for both *i*-line and *h*-line for different thickness of SU-8.

After using ZEMAX EE to obtain the light energy distribution at the different depth of the SU-8 resist based on the transmission of SU-8 thick film as shown in Figure 2.3, diffraction pattern for an open slot pattern in Figure 2.8(A) was numerically obtained and shown in Figure 2.10. Figure 2.10 (A) shows the simulated results for *i*-line light source and four different resist thicknesses. Figure 2.10(B) shows the simulation results for *h*-line light source at different resist thicknesses. Two observations can be made from the results shown in Figure 2.10. First, as the resist thickness increases, the non-uniformity of light intensity caused by diffraction becomes more serious. Secondly, shorter wavelength light (*i*-line) has less a problem in diffraction but the

light intensity drops fast with the depth and may have difficulty to cross-link SU-8 resist at the bottom region.



(A) Diffraction pattern in the bottom of the resist layer as projected by *i*-line light source



(B) Diffraction pattern in the bottom of the resist layer as projected by h-line light source.

Figure 2.10 Diffraction pattern after taking the absorption of SU-8 resist into consideration. The air gap between the resist and the mask is assumed to be zero.

Figure 2.11 shows the simulated sidewall profiles when a 20 $\mu$ m wide slot pattern is exposed using *i*-line and *h*-line of light source respectively [21]. The sidewall profile is defined by the threshold exposure dosage of lithography. The resist in the left side of the threshold boundary line received enough exposure dosage to fully cross-link the resist. The lithography dosage in the resist at the right side of boundary line is below the required threshold dosage and is removed in development process. Because of symmetry of the exposed pattern, only the right-

half of the exposed region is shown in simulated results in Figure 2.11. The sidewall profiles in Figure 2.11A and 2.11B are for the exposure with a zero gap and 50 $\mu$ m gap between mask and SU-8 resist, respectively. Several different situations have been conducted: h-line or i-line exposure, air gap or with glycerin. The simulation results show that glycerin has effects to reduce Fresnel diffraction. With wavelength selection (for example, using h-line dominated light source), the lithography quality may be further improved. From the foregoing analyses, it can be seen that the wavelength selection played the most important rule in optimal lithography of ultra thick SU-8 while the air gap compensation played a secondary rule. In comparison with air gap, glycerin compensation is proved to be marginally better in producing better sidewall profiles.

### **2.3.3 Experimental Results Using Filtered Light Source and Air Gap Compensation for Diffraction**

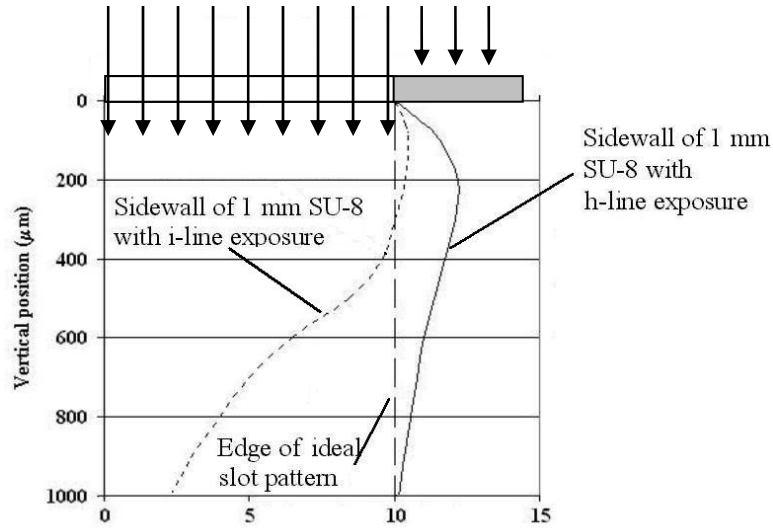
To demonstrate the superiority of the proposed optimal lithography of filtered light source and gap compensation, we will show three different groups of experiments in this section: (1) broadband light source without gap compensation, (2) broadband light source using glycerin for gap compensation, and (3) filtered light source with PolyMethyl MethAcrylate (PMMA) sheet (*i*-line eliminated) and gap compensation using the glycerin as suggested here.

A broadband light source was used in lithography process and a thick plate of PMMA used as an optical filter to eliminate the short wavelength components. The broadband spectra of an Oriel UV station before and after the PMMA filter are shown in Figure 2.12, which were measured using an Ocean Optics S2000 spectrometer. The UV light source has three major spectrum lines: i-line, h-line and g-line. A 4.538mm thick PMMA plate (not annealed) was used as a filter to eliminate the short wavelength components of the light source of Oriel UV station. The optical transmission spectrum of a 4.538mm-thick PMMA sheet without anneal is also shown in Figure 2.12. The transmission of this PMMA sheet is about 0.3% at i-line, 82% at h-

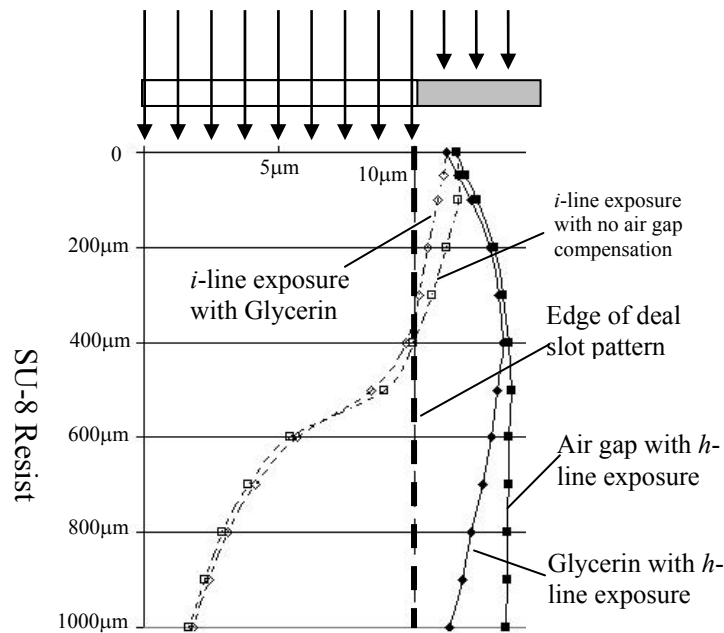


line, and 82% at g-line. The PMMA sheet filters out most of the light with wavelength less than or equal to 365nm. The spectrum of Oriel UV station used in this study after filtering with this PMMA sheet was measured and shown in Figure 2.12 where the i-line is removed, h-line and g-line are reduced. It was found that light intensity at 365nm dropped from 15.08mJ/cm<sup>2</sup> to 0.47mJ/cm<sup>2</sup>, and at 405nm dropped from 42.08mJ/cm<sup>2</sup> to 34.15mJ/cm<sup>2</sup>. This result is consistent with what was expected from the transmission spectrum of PMMA measured using spectrometer. Because the absorbance of unexposed SU-8 around g-line ( $\lambda=436\text{nm}$ ) is only about one third of that around h-line ( $\lambda=405\text{nm}$ ) and total exposure dosage with the light source as shown in Figure 2.12 after PMMA filter is dominated by h-line, the effect of g-line in the lithography of SU-8 will therefore be neglected under such conditions.

The detailed processing conditions for 1150 $\mu\text{m}$  thick SU-8 100 film are as follow: (1) Clean Si wafer with Acetone, IPA, DI water; (2) Spin coat SU-8 100 at 400rpm; (3) Level hot plate, bake 10 hours at 110°C, cool down to 60°C inside 1 hour, dwell at 55°C (Un-cross-linked SU-8's glass temperature is 50°C~60°C) for 4 hours, cool down to room temperature inside 3 hours; (4) Exposure the sample using broad band light source (with spectrum as shown in Figure 2.12, includes *i*-line, *h*-line, *g*-line) with total exposure dosage 2J/cm<sup>2</sup>, for PMMA filter wavelength selection exposure (with spectrum as shown in Figure 2.6, includes h-line and g-line) with total exposure dosage 12J/cm<sup>2</sup>; (5) Post bake at 110°C for 20 minutes, cool down as step (3); (6) Develop sample using SU-8 developer at 32°C with SONOSYS megasonic actuator driven with a 250 W power supply for 2 hours. The megasonic transducer was placed in a water bath supporting a quartz tank in which the developer and substrate were located. Wafers were face to the megasonic actuator. (7) Rinse sample with IPA several times, dry naturally.



(A) On left side of these profile lines, the exposure dosage is enough to cross-link resist. The gap between mask and SU-8 is assumed to be zero.



(B) The simulated sidewall profiles for a 20  $\mu\text{m}$  wide slot on the mask with 50  $\mu\text{m}$  gap between mask and SU-8. On left side of these profile lines, the exposure dosage is enough to cross-link resist

Figure 2.11 The simulated sidewall profiles for a 20  $\mu\text{m}$  wide slot on the mask with 50  $\mu\text{m}$  gap between mask and SU-8. On left side of these profile lines, the exposure dosage is enough to cross-link resist.

To measure the sidewall quality of the microstructures fabricated using filtered light source and gap compensation, a 20- $\mu\text{m}$ -feature-sized microstructure with a flat edge was

removed from the substrate and placed on the measurement stage of the VEECO optical profiler. The  $R_s$  (Roughness of Standard Deviation) was then measured along the 1150 $\mu\text{m}$  length. It was found that the roughness of standard deviation (in light incident direction) was 2.72 $\mu\text{m}$  over the entire length of 1150 $\mu\text{m}$ .

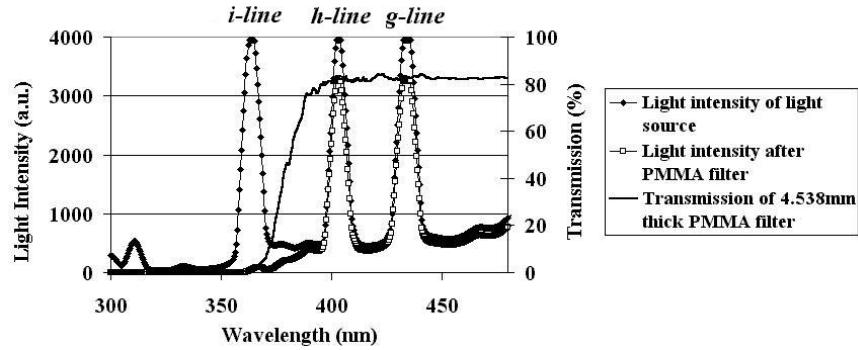
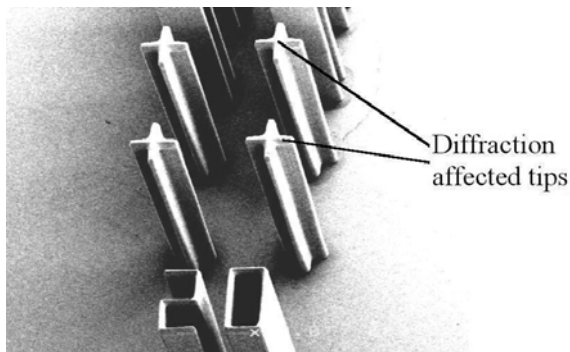


Figure 2.12. Light intensity before and after filter for the Oriel UV station at 200W output

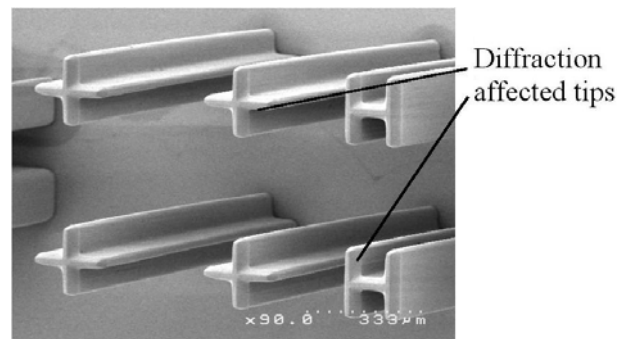
Figure 2.13 and Figure 2.14 shows a group of micro crosses and cylindrical patterns with the height of 1150 $\mu\text{m}$  produced with different conditions: 1) broadband light source with no air gap compensation; 2) broadband light source and air gap compensation using glycerin solution; 3) the filtered light source (*i*-line eliminated) with no air gap compensation; 4) filtered light source with gap compensation using glycerin solution.

For these 1150 $\mu\text{m}$  high microstructure, the minimum designed thicknesses of the crosses (open pattern) achieved are 20 $\mu\text{m}$  width feature size for broadband exposure and without air gap compensation, 15 $\mu\text{m}$  for broadband exposure and with glycerin compensation, 9 $\mu\text{m}$  for *h*-line dominated exposure and without glycerin compensation, 8 $\mu\text{m}$  for *h*-line dominated exposure and glycerin gap compensation. The dark region in Figure 2.13(A) was due to the residuals of the development.

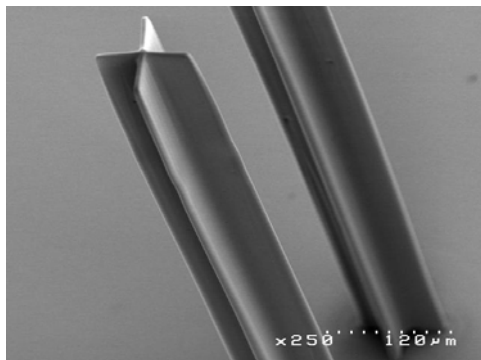
For these 1150 $\mu\text{m}$  high microstructure and compared with the cross pattern, the cylindrical tubes (close pattern) are more difficult to be developed. The minimum cylindrical tube achieved are 20 $\mu\text{m}$  sidewall width and 45 $\mu\text{m}$  inner diameter for broadband exposure and without/with air gap compensation, 10  $\mu\text{m}$  sidewall width and 45 $\mu\text{m}$  internal diameter using h-line dominated exposure and without gap compensation, 8  $\mu\text{m}$  sidewall width and 30 $\mu\text{m}$  internal diameter using filtered light source and with glycerin compensation



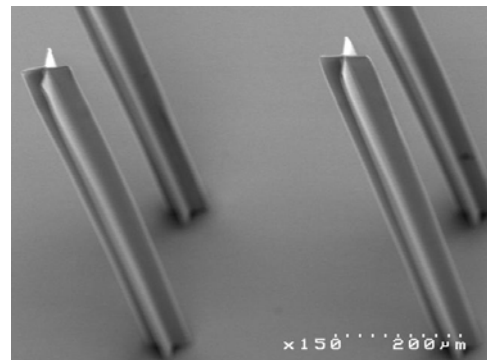
(A) Broadband exposure with no the air gap compensation. Crosses with designed thickness of 20  $\mu\text{m}$  and height of 1150  $\mu\text{m}$ .



(B) Broadband exposure and air gap compensation using glycerin. Crosses with designed thickness of 15  $\mu\text{m}$  and height of 1150  $\mu\text{m}$ .

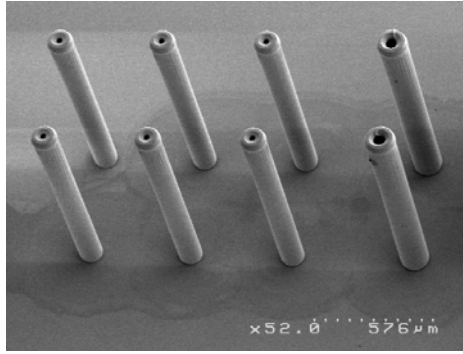


(C) Crosses with designed thickness of 9  $\mu\text{m}$  and height of 1150  $\mu\text{m}$ , Processing conditions: filtered light source and no air gap compensation.

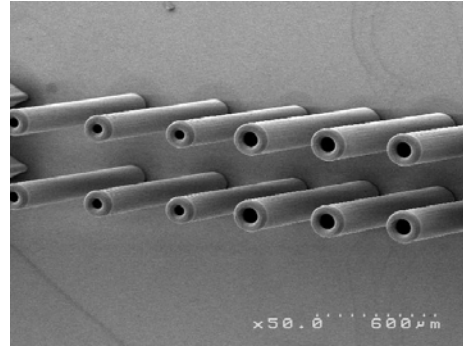


(D) Crosses with designed thickness of 8  $\mu\text{m}$  and height of 1150  $\mu\text{m}$ , Processing conditions: filtered light source and air gap compensation using glycerin.

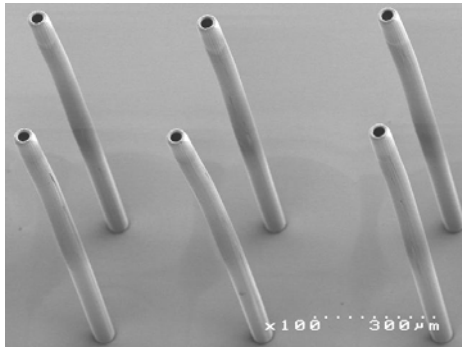
Figure 2.13. Cross-patterns made using filtered light source and three different UV-lithography processing conditions.



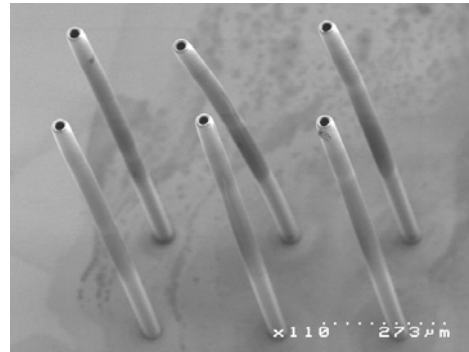
(A) Micro cylinders with a height of 1150  $\mu\text{m}$  and designed wall thickness of 20  $\mu\text{m}$ , internal diameter of 45  $\mu\text{m}$  or 90  $\mu\text{m}$ , obtained using filtered light source and no gap compensation



(B) Micro cylinders with a height of 1150  $\mu\text{m}$  and designed wall thickness of 20  $\mu\text{m}$ , internal diameter of 45  $\mu\text{m}$  or 90  $\mu\text{m}$ , obtained using filtered light source and glycerin gap compensation



(C) Micro cylinders with a height of 1150  $\mu\text{m}$  and designed wall thickness of 10  $\mu\text{m}$ , internal diameter of 45  $\mu\text{m}$ , obtained using filtered light source and no gap compensation



(D) Micro cylinders with a height of 1150  $\mu\text{m}$  and designed wall thickness of 8  $\mu\text{m}$ , internal diameter of 30  $\mu\text{m}$ , obtained using broadband exposure and glycerin gap compensation

Figure 2.14. Micro cylinders (1150  $\mu\text{m}$  tall) obtained using three different sets of processing conditions.



Figure 2.15 Comb structure with line/space 20  $\mu\text{m}$

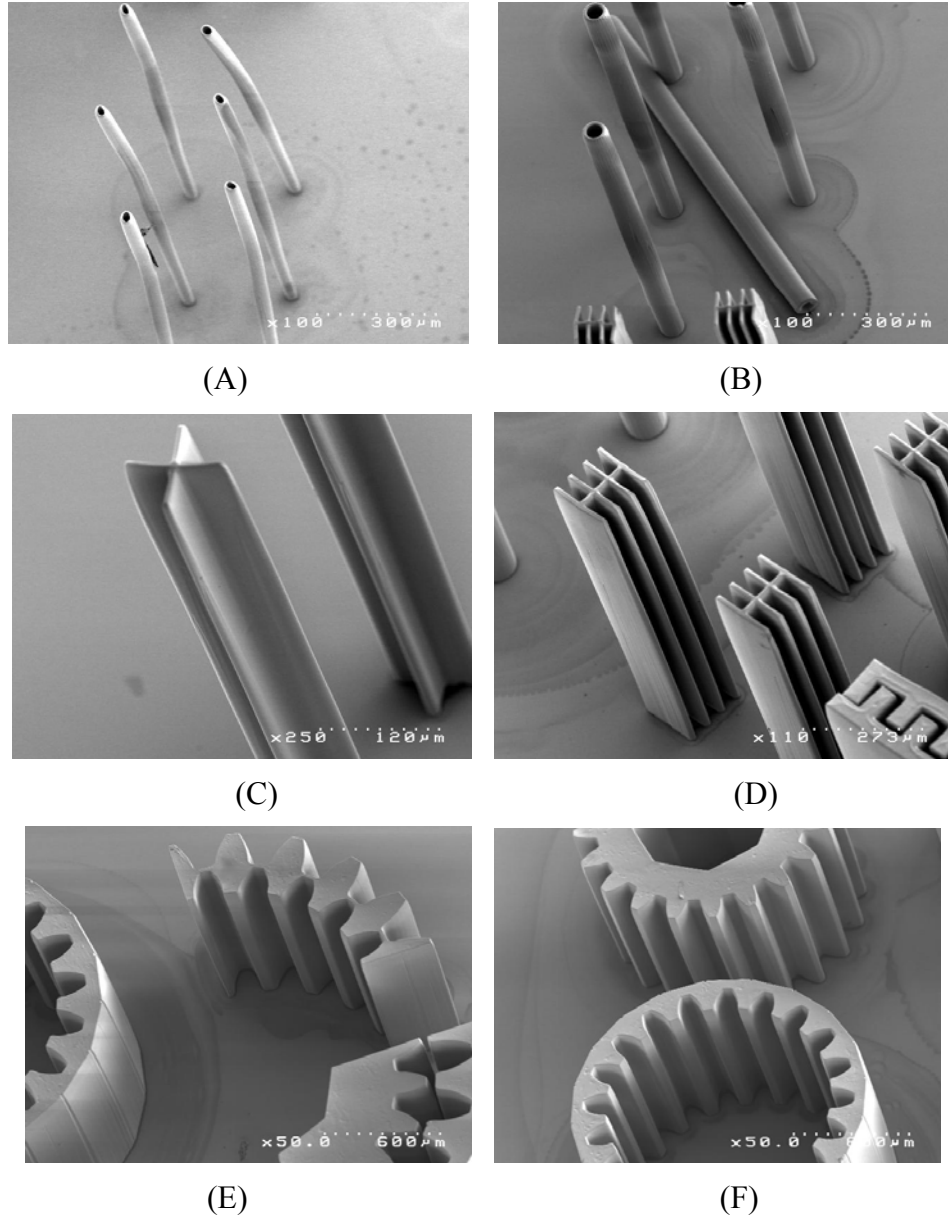
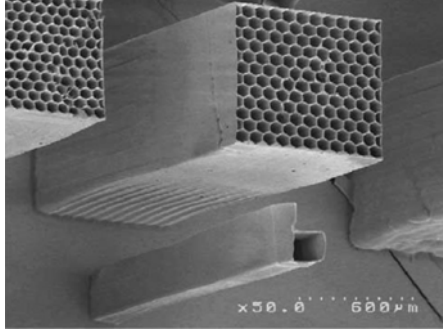
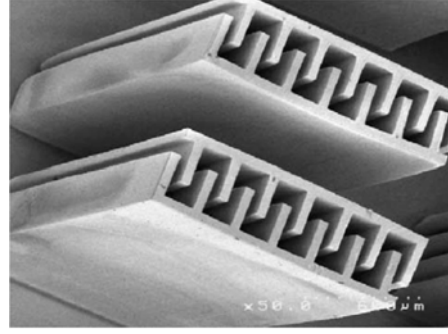


Figure 2.16. Structures made using filtered light source and gap compensation. (A) 1150µm high micro tubes with 6µm wide sidewall tube and the mouth of the tube change its shape by the liquid surface tension when they get dry. (B) 1150µm high micro tube with 10µm wide sidewall tube; the fall down tube shows the bottom part of the tube is completely developed and the tube is a hollow tube. (C) 1150µm high microstructure with 10 µm wide feature size. (D) 1150 µm high microstructure with 15µm wide feature size. (E) 1150 µm high microstructure with gear patterns. (F) 1150µm high gear pattern microstructures. (G) SEM image of honeycomb structures with designed sidewall width of 6µm and a height of 2000 µm. The microfeature next to the honeycombs is an Arabic number “6” with designed width of 7µm and a height of 2000µm. (H) Microcomb structures with designed thickness of 40 µm and height of 2000 µm (Figure continued)



(G)



(H)

The theoretical optical resolution of line/space of the width  $b$  can be estimated by the following equation:

$$b_{\min} = \frac{3}{2} \sqrt{\lambda(s + \frac{1}{2}d)} \quad (2.6)$$

where  $b$  is the width of line or space,  $\lambda$  is the wavelength of the lithography light,  $s$  is the air gap between the mask and the photoresist, and  $d$  is the resist thickness. For 1150  $\mu\text{m}$  thick SU-8 resist, and assuming no air gap, the optical resolution can be estimated as 21.7  $\mu\text{m}$  for i-line and 22.9  $\mu\text{m}$  for h-line. Because of the low absorption in g-line, the lithography processes in broadband lithography was dominated by the combined effect of i-line and h-line, especially the i-line. These calculated results are very consistent what was observed in the experiments for broadband lithography without air gap compensation or using glycerin compensation. The lithography quality of comb structures with broadband light source becomes quite bad as the feature sizes dropped to about a width of 20  $\mu\text{m}$  and height of 1150  $\mu\text{m}$ , with some improvement after gap compensation using glycerin. Figure 2.15 shows a comb structure made using filtered light source and gap compensation with glycerin. It can be seen that the comb structures obtained using the suggested filtered light source and gap compensation with glycerin have excellent sidewall quality and resolutions. Both structures were developed all through and clearly

separated. The top fingers are removed together by the liquid surface tension in the dry processing.

Figure 2.16 are SEM pictures for some SU-8 microstructures patterned with *h*-line dominated UV exposure and the processing step as the above. These SEM pictures demonstrate the UV lithography capability for SU-8 high-aspect-ratio microstructures.

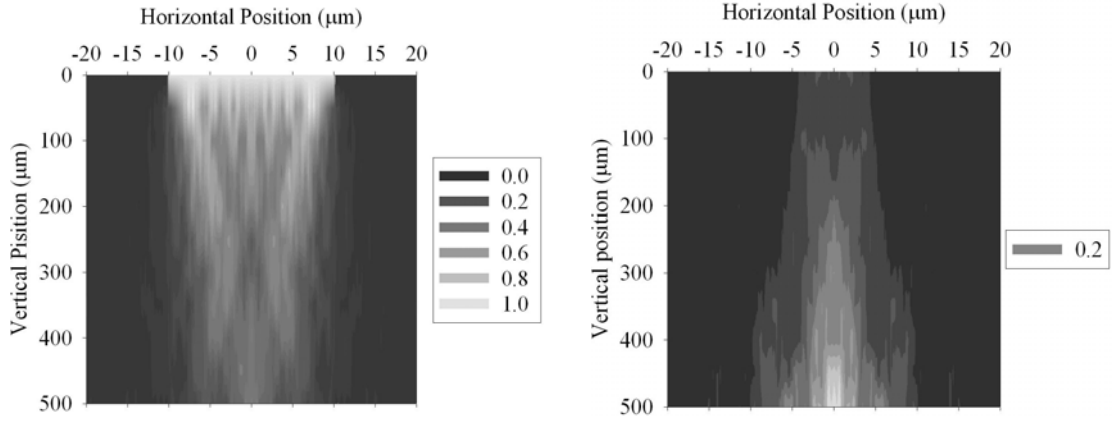
Both theoretical and experimental studies were conducted on UV lithography of ultra thick SU-8 resist. Specifically, the research efforts have focused on two important processing conditions: wavelength selection and air gap compensation. It has been proved that the wavelength selection plays a significant role in obtaining high aspect ratio microstructures using UV-lithography of SU8, while air gap compensation played a marginal one, with more effect at the top parts of the microstructures. It was also demonstrated that a thick PMMA plate could be used as a very effective filter to eliminate the *i*-line component of the light source. Because of the low absorption coefficient of SU-8 for *g*-line, the lithography process can then be treated as *h*-line dominated. By using optical filter to eliminate the *i*-line component of the light source in addition to gap compensation with glycerin, patterns with feature size 6  $\mu\text{m}$ , 1150  $\mu\text{m}$  high (aspect ratio more than 190:1), and high quality sidewall were obtained. The experimental results also showed that microstructures with thickness up to 2mm could also be produced using the reported technology.

## **2.4 Tapered Sidewall in *i*-line and *h*-line Lithography and Their Applications**

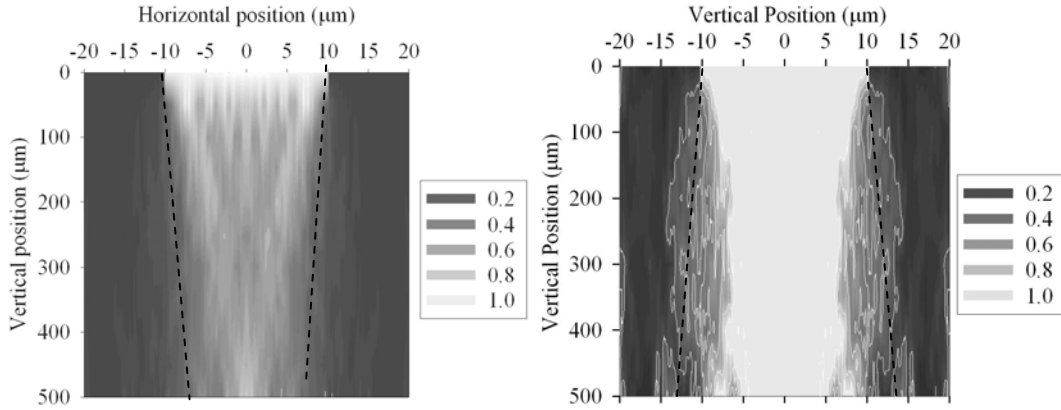
In most cases, the quality of vertical sidewalls obtainable with UV lithography of SU-8 is very good if the exposure dosage and dosage ratio between *i*-line and *h*-line wavelengths are well controlled. In some condition, when the resist thickness is too high or exposure dosage is too low for *i*-line dominated exposure or when the dosage is too high in *h*-line dominated exposure, the



sidewalls obtained can be tapered significantly. Research efforts were made to take the advantages of this phenomenon in MEMS and BioMEMS, such as the fabrication of tempered molding insert [43], micro needle array [47].



(A) Dosage distribution due to diffraction effects with *i*-line exposure (365nm). (B) Dosage distribution due to substrate reflection with *i*-line exposure (365nm).



(C) Total dosage distribution for a 20 $\mu$ m slot aperture with *i*-line exposure (365nm). The resulting structure shows a wider top and a narrower bottom. (D) Total dosage distribution for a 20 $\mu$ m slot aperture with *h*-line exposure (405nm). The resulting structure shows a narrower top and a wider bottom.

Figure 2.17. Simulation results for a 20 $\mu$ m slot aperture

In this section, we will study the physics behind the phenomenon and conduct a numerical simulation for the sidewall profile lithographed with *i*-line and *h*-line dominated light source. In the numerical simulation, refractive indices of SU-8 are  $n=1.668$  at  $\lambda=365$  nm (*i*-line) and  $n=1.649$  at  $\lambda=405$  nm (*h*-line), respectively. The effect of the substrate reflectivity (such as

silicon substrate, about 0.575 for vertical incident light with a wavelength of 365nm, and 0.473 for a wavelength of 405nm) was considered in the numerical simulations. Its transmission versus thickness curve is shown in Fig. 2.3 at these two selected wavelengths. For a given mask pattern, the entire SU-8 resist is divided into different numerical layers. Light intensity distribution within different numerical layers were calculated with ZEMAX, and imported to SigmaPlot (Systat Software, Inc. Point Richmond, CA, USA) to generate the contour of light energy distribution in the entire resist layer. It was assumed that the SU-8's absorbance of the UV light is directly proportional to the local energy intensity. The dosage contour is therefore congruent with that of the energy distribution. The contour of the total exposure dosage and the development condition combine to determine the final sidewall profile of the SU-8 pattern.

Numerical simulations were conducted for two different mask patterns, shown schematically in Fig. 2.2 (A) and (B). One is an open slot aperture and another is an obscuration. These produce, in negative resists such as SU-8, a protrusion and an open channel, respectively. When displaying the simulation results, light intensities were normalized by its value at the resist surface: the light intensity at the same level or higher than the incident lithography light is denoted as 1 and shown as a bright gray; lower light intensity areas in resist are denoted with smaller numbers and shown as darker gray. Figure 2.11 shows simulation results for dosage distributions corresponding to a 20 $\mu$ m slot aperture with *i*-line (365 nm) and *h*-line (405 nm) exposures, respectively. In all simulations, a resist thickness of 500  $\mu$ m and a zero air-gap were assumed. Brighter and darker regions represent, respectively, higher and lower exposure dosages. Dashed lines indicate the boundary between regions with or without sufficient dosage to cross-link the SU-8 resin, and therefore potential sidewalls of the final SU-8 structure after development. Figure 2.17a shows the dosage distribution produced by light exposure through the

20  $\mu\text{m}$  slot aperture considering only diffraction effects. Figure 17b shows the dosage distribution caused by substrate reflection, assuming a reflectivity of 0.85 under normal incident for the gold-coated plating seed-layer surface. Figure 17c shows the total exposure dosage distribution, combining diffraction and reflection effects. Figure 17d shows the total dosage distribution for *h*-line (405 nm) exposure.

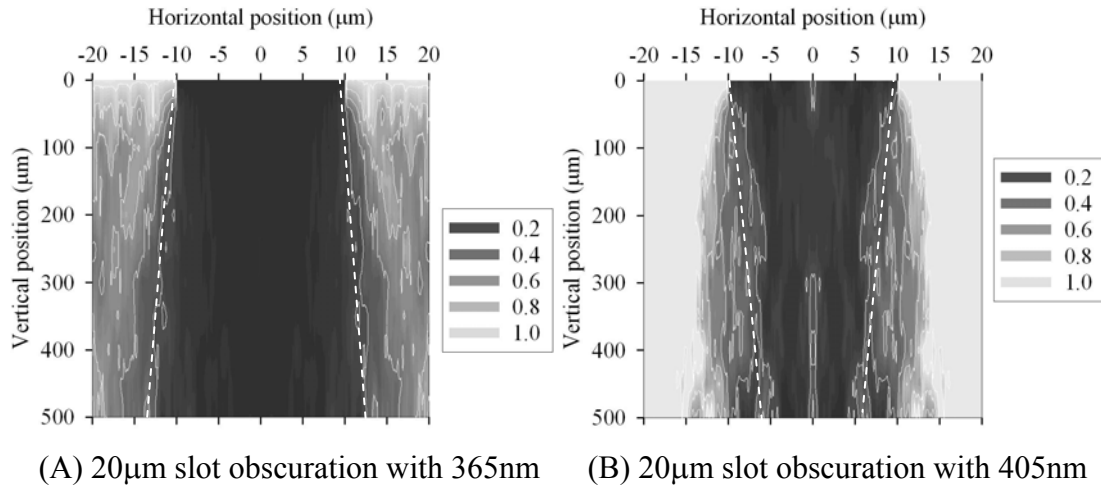


Figure 2.18. Dosage distributions for generating SU-8 channels: (A) a 20  $\mu\text{m}$  slot obscuration with *i*-line exposure (365nm); (B) a 20  $\mu\text{m}$  slot obscuration with *h*-line exposure (405nm).

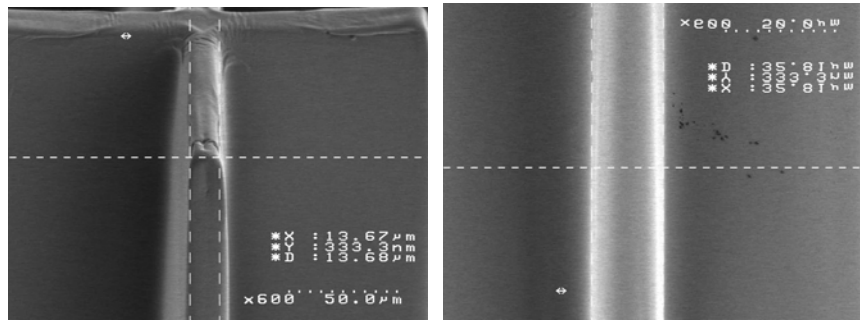
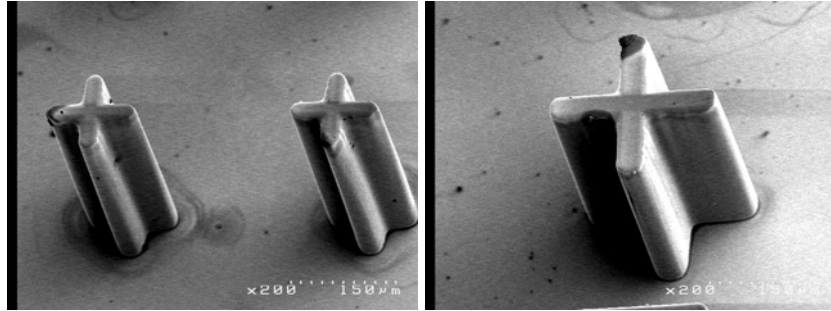


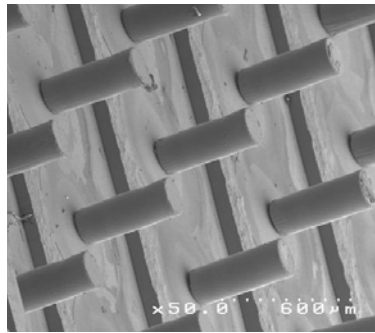
Figure 2.19 SU-8 protrusions with tapered sidewalls (narrower top and wider bottom)

Simulation results for a 20  $\mu\text{m}$  wide slot obscuration with *h*-line and *i*-line exposures are shown in Fig. 2.18 (A) and (B), respectively. Because of the negative tone of the SU-8 resist, patterns obtained with a slot obscuration exposure will be channels. As shown in Fig. 2.18 (A)

and (B), the channel obtained with i-line exposure will be narrower at the top and wider at the bottom. Using h-line exposure, the channel will be wider at the top and narrower at the bottom.



(A) 375  $\mu\text{m}$  high, 10  $\mu\text{m}$  wide cross pattern (B) 375  $\mu\text{m}$  high, 20  $\mu\text{m}$  wide cross pattern



(C) SEM images of an electroplated prototype Ni two-level molding insert

Figure 2.20 microstructure with tapered sidewalls (narrower top and wider bottom)

To obtain the desired tapering angle in the SU-8 plating mold for mold insert fabrication or micro needle array, an exposure wavelength of 405 nm should be selected with exposure from resist's top to bottom [43]. If using backside exposure, an exposure wavelength of 365 nm should be selected [47]. Fig. 2.18(B) shows that a narrow strip at the middle of the obscured region is also significantly exposed. This localized high dosage strip within the obscured region is responsible for the fact that, when the desired channel pattern becomes too narrow, full development becomes very difficult. Figure 2.19(A) and (B) show a SU-8 protrusion cross with a designed width of 20  $\mu\text{m}$  and a height of 1,150  $\mu\text{m}$ . This structure was obtained with h-line exposure. The scanning electron microscopy (SEM) images show that the width of the SU-8

cross varies from 13.5  $\mu\text{m}$  at the top to 19.7  $\mu\text{m}$  at about 75  $\mu\text{m}$  from the top, finally to 32.8  $\mu\text{m}$  at the bottom. This represents a taper angle of  $\sim 1^\circ$ . Figure 2.20 is two SEM picture for 375  $\mu\text{m}$  high, 10  $\mu\text{m}$  m wide cross pattern and 375  $\mu\text{m}$  high, 20  $\mu\text{m}$  wide cross pattern. All of them have a smaller top and bigger bottom. This technology has been used to fabricated two-level metal mold insert. Figure 2.20.(C) shows one SEM image of an electroplated prototype Ni two-level molding insert with tapered angle.

## 2.5 Tilted Lithography of SU-8 and Refraction Compensation

SU-8 is well suited for the fabrication of three-dimensional microstructures using tilted exposure. A variety of SU-8 resist structures such as slop, trapezoids, dovetails, as well as various conical shapes, can be fabricated using tilted lithography (or called inclined lithography) [24-31, 37, 48-54]. Tilted lithography of SU-8 can be used to fabricate reflective mirror and beam-splitter [53], cell filter [54], mixer [24, 48, 49], etc. We have designed, fabricated, tested, and analyzed the micromixer based on arrays of impinging micro jets [24], out-of-plane microlens [26, 28, 30], out-of-plane microlens array [27, 31], fiber bundle coupler [29], and three-dimensional hydrofocus component [25] using tilted lithography of SU-8. They will be presented in Chapter 4, 5, 6 and 7.

Because the refraction of the light at the surface of the SU-8 resist, light beam projected on the resist at an incident angle may propagate at a reduced refraction angle. Based on the refraction index of the SU-8 ( $n=1.668$  at  $\lambda=365\text{nm}$ ,  $n=1.650$  at  $\lambda=405\text{nm}$ ), the refraction angle can be approximately calculated based on the Snell law, such as  $25.08^\circ$  for  $i$ -line with  $45^\circ$  incident angle as shown in Figure 2.15(A). The critical angle is about  $36.8^\circ$  at 365nm,  $37.3^\circ$  at 405nm. If a larger refractive angle is needed, optical liquid and a coupling prism are used to compensate for the light refraction.

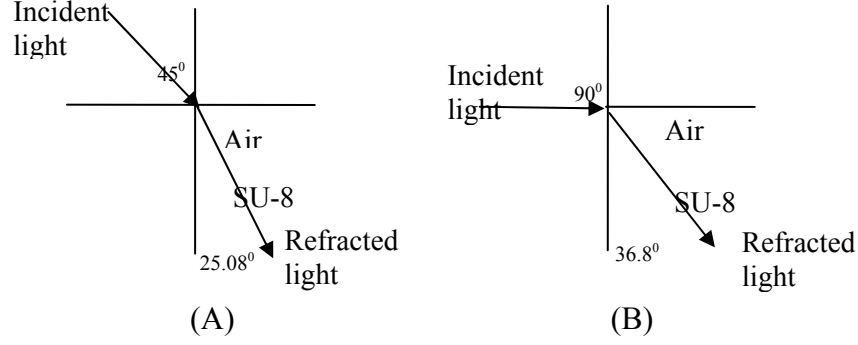


Figure 2.21. The refraction of the SU-8 resist may cause the projected light beam to bend over and therefore leading to reduce angle of the light projection. SU-8's refraction and the critical angle (critical angle is about  $36.8^\circ$  at 365nm,  $37.3^\circ$  at 405nm)

The working principle to obtain larger exposing angle than the critical angle in SU-8 lithography is schematically shown in Figure 2.22. The positions of the prism, mask, SU-8 and the substrate are as shown in Figure 2.22. Based on the similar principle, some researchers also reported to use glycerin solution [53] or water [54] as interface medium to obtain bigger exposing angle more than critical angle in SU-8 lithography. For these two methods, the theoretical maximum refractive angles are  $71^\circ$  for glycerin solution and  $56.2^\circ$  for glycerin solution and water respectively (the theoretical minimal angle between the structure and the substrate are  $19^\circ$  for glycerin solution and  $33.8^\circ$  respectively). With solid material, prism, used for the compensation as shown in Figure 2.22 or Figure 2.23, higher achievable refractive angle can be obtained.

In Figure 2.22, if the angle at which the light enters SU-8 resist, needs to be  $\theta_1$ , from Snell's law,

$$n_1 \sin \theta_1 = n_2 \sin \theta_2 = n_3 \sin \theta_3 = n_4 \sin \theta_4 = n_5 \sin \theta_5, \quad (2.6)$$

$\theta_5$  can be obtained as

$$\theta_5 = \sin^{-1}\left(\frac{n_1 \sin \theta_1}{n_5}\right) \quad (2.7)$$

From geometry relationship, we know

$$\theta_6 = \theta_5 - 45^\circ = \sin^{-1}\left(\frac{n_1 \sin \theta_1}{n_5}\right) - 45^\circ \quad (2.8)$$

From Snell's law,  $\theta_7$  can be obtained:

$$\theta_7 = \sin^{-1}\left(\frac{n_6 \cdot \sin \theta_6}{n_7}\right) = \sin^{-1}\left\{\frac{n_6}{n_7} \cdot \sin\left[\sin^{-1}\left(\frac{n_1 \sin \theta_1}{n_5}\right) - 45^\circ\right]\right\} \quad (2.9)$$

$$\theta = 45^\circ + \theta_7 \quad (2.10)$$

In Figure 2.22, the substrate therefore needs to be kept  $\theta = 45^\circ + \theta_7$  with the horizontal level (because the light beam in the UV station is always in vertical direction) to completely compensate for the refraction at the interface to obtain a  $\theta_1$  degrees refractive angle inside SU-8 photoresist.

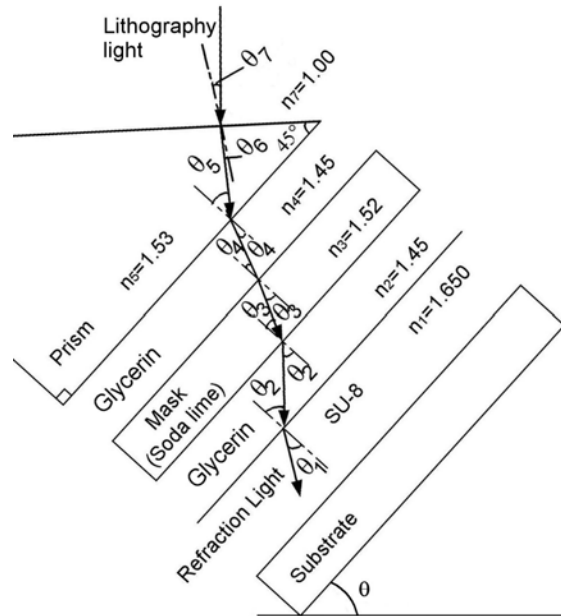


Figure 2.22 Tilted lithography setup for refractive angle more than SU-8's critical angle

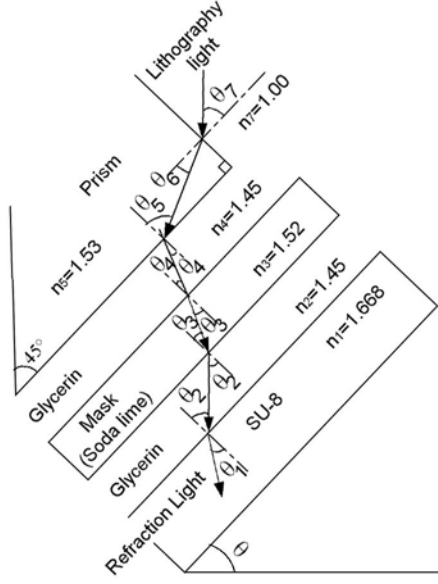


Figure 2.23 Tilted lithography setup for larger refractive angle

In Figure 2.23, the relationship between the  $\theta_1$  and  $\theta_5$  are the same as the equation 2.7.

From geometry relationship, we know

$$\theta_6 = 90^\circ - \theta_5 = 90^\circ - \sin^{-1}\left(\frac{n_1 \sin \theta_1}{n_5}\right). \quad (2.11)$$

From Snell's law,  $\theta_7$  can be obtained:

$$\theta_7 = \sin^{-1}\left(\frac{n_6 \cdot \sin \theta_6}{n_7}\right) = \sin^{-1}\left\{\frac{n_6}{n_7} \cdot \sin\left[90^\circ - \sin^{-1}\left(\frac{n_1 \sin \theta_1}{n_5}\right)\right]\right\}. \quad (2.12)$$

$$\theta = 90^\circ - \theta_7 \quad (2.13)$$

In Figure 2.23, the substrate therefore needs to be kept  $\theta = 90^\circ - \theta_7$  with the horizontal level (because the light beam in the UV station is always in vertical direction) to completely compensate for the refraction at the interface to obtain a  $\theta_1$  degrees refractive angle inside SU-8 photoresist.



## **CHAPTER 3. USING CURED SU-8 MICRO-MOLD INSERT TO REPLICATE BIODEGRADABLE (PLGA) MICROSTRUCTURES FOR DRUG DELIVERY**

### **3.1 Implantable Drug Delivery Systems and the Advantages of PLGA**

Implanted drug delivery systems are widely used and have some unique advantages: improved efficiency, reduced side effect, on-spot delivery, and convenient therapy. Most implanted drug delivery systems are based on three basic delivery mechanisms: swelling control, osmotic pumping, and diffusion. Of the three, osmotic pumping and diffusion have been the most successful in delivering drug in a linear process. The drug dosage released is proportional to square root of the release time. In drug delivery systems based on swelling control, solvent penetration into the matrix of the drug device is normally much slower than diffusion of the drugs, which then results in a lowered release rate. Delivery systems based on the osmotic principle can provide a constant release rate as seen with the simple oral tablets commonly used. Miniature sized osmotic drug delivery systems currently used are based on membrane fluid flow. They have the unique advantage of providing linear delivery for long periods of time, from a few weeks to many months. Monolith diffusion regulated drug delivery systems normally offer nonlinear release rates.

In the past few years, several research efforts were reported in the literature in the area of microfabricated devices for implanted drug delivery [55-57]. Most of the reported researches have concentrated on using an active pump to deliver the drug and the approaches require much more complicated designs. The major disadvantage of these micro drug delivery systems is that they all have to be surgically removed after the drugs are delivered.

Using polymers for implantable drug delivery purposes has been a very important research area for many years [58]. Bio-degradable polymers, such as PLGA, have been the most

attractive one because it does not require removal after the drug has been released. Polylactide (PLA) and its copolymers with glycolide (PLGA) were originally used in the medical field to make bio-absorbable structures. However, their unique properties, such as versatile degradation kinetics, established safety, and biocompatibility, have made them ideal materials for drug delivery applications. In comparison with other types of MEMS drug delivery systems, another advantage of using PLGA structures for drug delivery is that it can be used in a passive delivery system.

Up to today, most of the fabrication technologies for PLGA based drug delivery reported in the field are achieved by solvent evaporation. PLGA was used to make coated micro particles for drug delivery [59-61]. Qian, Nasonngkla, and Gao reported an effort in making PLGA polymer millirods for sustained release of 5-fluorouracil [62]. In their approach, micro-particles containing the drugs to be delivered were cast into millimeter-sized PLGA miniature structures. The applications in their work were to deliver drugs to targeted spots in organs of patients.

Vozzi et al. [63] also reported a research work to microfabricate PLGA scaffolds for tissue engineering applications. In their work, micro-PLGA scaffolds were made using micro insert mold made with lithography method. Their work proved the feasibility of micro-molding of PLGA polymer though the quality and the depth of the reported structures may not be suitable for drug delivery purposes.

The research effort reported in this chapter targets to design and fabricate truly 3-D micro-sized PLGA structures using UV-LIGA technique [41, 64]. Our research work took a unique approach to integrate the advantages of bio-degradable polymer as used in microsphere drug delivery and the LIGA microfabrication technology for high precision batch production. The prototype design utilized multilayer of coaxial rings. The microstructures with micro

chambers were fabricated and filled with the actives to be delivered, and then bonded together by hot-pressing as shown schematically in Figure 3.1.

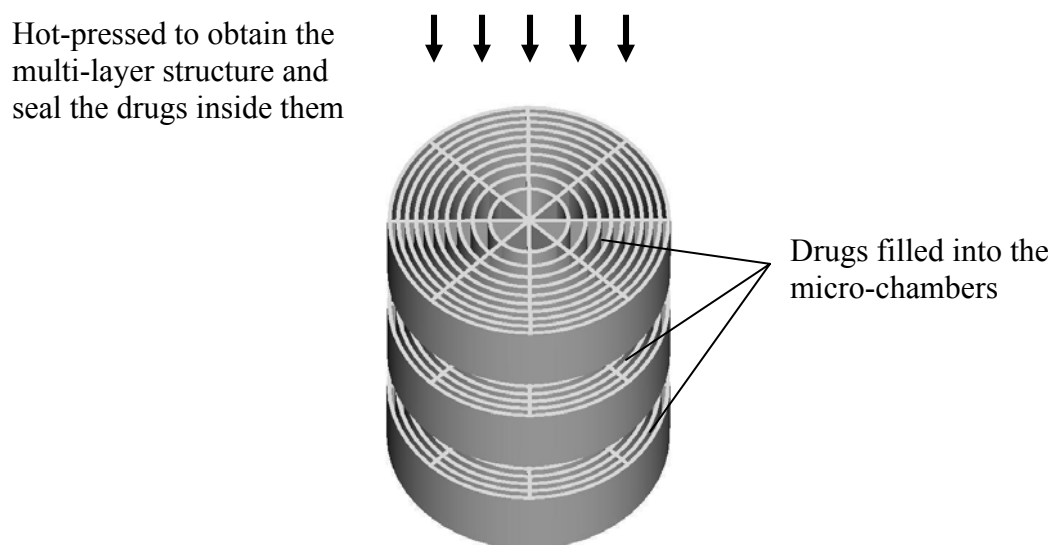


Figure 3.1. Sandwiched multi-layer PLGA microstructures for drug delivery.

This type of drug delivery system has some unique advantages in controlled long-term drug delivery. It can be used to intelligently obtain timely and linear delivery of drugs. The flexibility of the multi-layer and large array of micro drug chambers make it possible to obtain long term simultaneous delivery of multiple drugs, which may have significant advantages in some clinic applications. Careful study of the material properties and design can help to achieve linear delivery.

### 3.2 Design and Fabrication of the Prototype Drug Capsule

In order to obtain a linear delivery rate, a prototype design as shown in Figure 3.2 was adopted for the drug capsule. When the PLGA packaged with a specific drug, the PLGA capsule would degrade gradually from the outermost section in a biodegradable environment. To obtain a linear drug release rate, it is obviously necessary for the capsule to have about equal volume between each layer of the ribs and sidewalls along the radial direction. In the preliminary design,

the PLGA microstructures were formed in a series of coaxial rings. These rings formed the sidewalls for the drug chambers with all of the sidewalls at the same thickness. The volumes of the chambers in each ring along radial direction were designed to be equal.

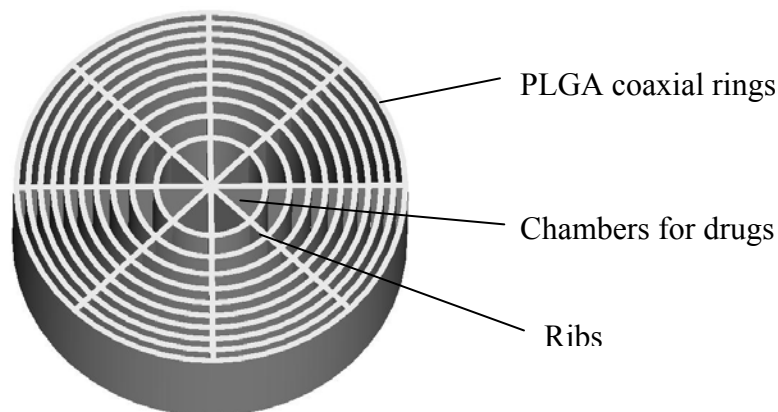


Figure 3.2. The coaxial rings form the chambers for the drug delivery

Assume that the released actives and degraded PLGA will not have any significant effects on the biological environment, then any potential influences of the circumstance conditions on the degrading rate of the PLGA can be neglected. Then degradation rate of PLGA microstructures can be treated as constant as the PLGA sidewalls of the capsule dissolves into the saline solution and the actives released gradually. If it is assumed that the covering layers in the axial direction are thick enough or are made of no-degradable materials such as glass or silicon (for testing purposes only as used in this work), the degrading process may only happen along the radial direction. These PLGA micro-chambers would then degrade layers at the same rate in radial direction. With an equal amount of actives released as each layer of micro chambers broke down, a linear delivery rate can be expected. To improve the physical strength of the PLGA coaxial rings, reinforcement ribs are added in the design as shown in Figure 3.2. Compensation is then required for the volume change of the drug chambers caused by the added ribs.

The PLGA microstructures were fabricated using UV-LIGA fabrication process. The general flow chart for the microfabrication is shown in Figure 3.3.

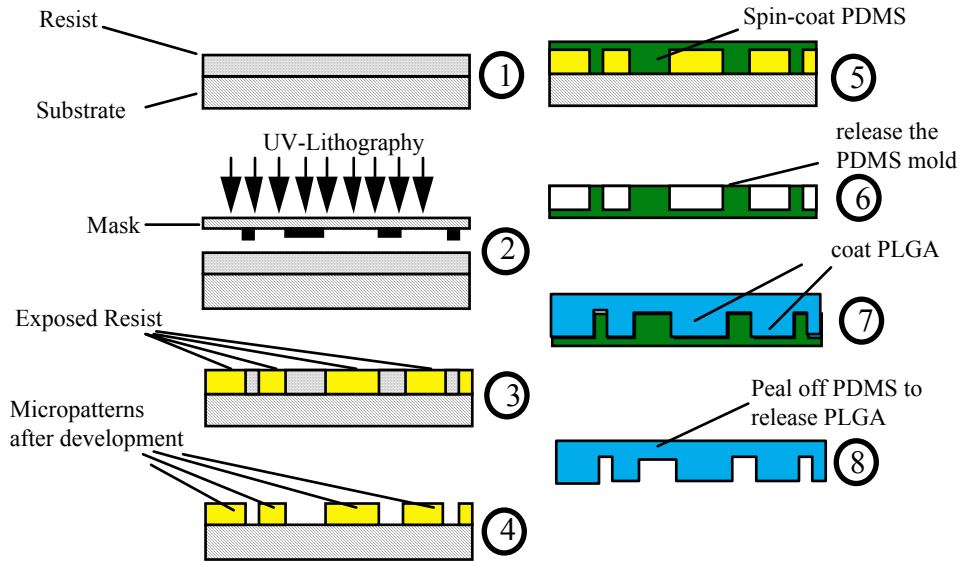
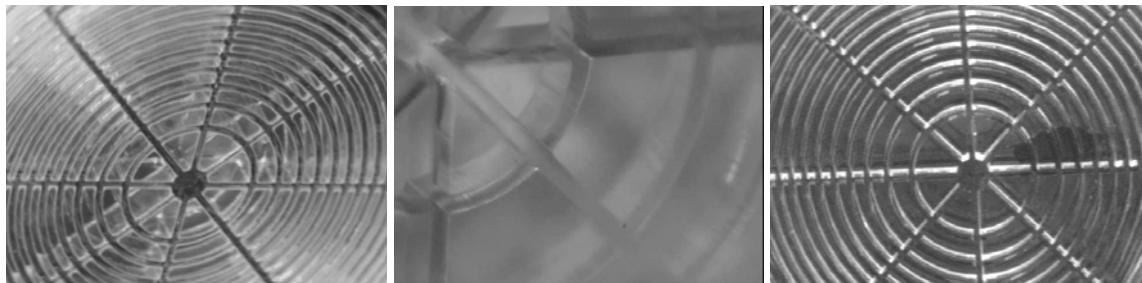


Figure 3.3. UV-LIGA Fabrication flow Chart for the PLGA microstructures

An optical mask was used to lithographically pattern the SU-8 insert-mold as shown in steps 1, 2, 3, and 4. A thin layer of PDMS (polydimethylsiloxane) was then coated on the SU-8 micro patterns. The PDMS layer is mechanically peeled off to obtain the final mold. This PDMS mold was then used to fabricate the PLGA structures. Because PDMS is very flexible, it can be easily removed from the coated PLGA without causing significant deformation of PLGA structures. Liquid nitrogen may also be used to help to remove the PLGA structures from PDMS insert mold because of the stress generated by dramatically lowered temperature. In addition, other special materials may also be coated on the PDMS to reduce adhesion and make it easier to release the PLGA structures in molding process.

The detailed fabrication procedure for PLGA microstructures is as follows: (1) Clean Si wafer with acetone, IPA, DI water clean, dry the wafer, then do plasma ash; spin coat SU-8, pre-bake at 96°C with enough time, then cool down; (2) Exposure SU-8; (3) Post-bake at 96°C 20

mins, then cool down the sample; (4) Develop SU-8; (5) Mix prepolymer and catalyzer for PDMS in 10:1 w/w ratio, vacuum to remove bubbles created in mixing; the mixed PDMS solution is then poured on the SU-8 model and put into vacuum oven again to permit the PDMS solution to fill the deep structures and remove the bubbles; bake the samples in oven for 2 hours at 85°C, then cool down to room temperature; (6) Remove the PDMS micro-patterns from the SU-8 mould with high-pressure gas; (7) Clean PDMS moulds with IPA and rinsed with DI water. After the PDMS moulds become dry, they were cleaned with plasma-ash at a temperature below 50°C; soak PDMS moulds in DI water, then placed in vacuum oven again to help to fill all of the micro gaps; rinse PDMS moulds by IPA for another 20 minutes, then rinsed by acetone for 10 minutes to fill up all of the micro-sized holes in the PDMS moulds with acetone which serves as the solvent of PLGA solution; prepare the PLGA solution by dissolving solid state PLGA into acetone in 1:8 ~ 1:15 w/w ratio and then pour the PLGA solution on the PDMS moulds which were covered by acetone; (8) Use hot-plate to bake the samples for 1 hours at 60°C, cool down, and finally the PLGA microstructures are peeled from the PDMS model.



(A) SU-8 structure

(B) PDMS mold.

(C) Molded PLGA structure.

Figure 3.4. Photographs of coaxial microstructures with reinforcement ribs.

In comparison with the results previously reported by other researchers, the microstructures fabricated in this research work have much higher aspect ratio, achieved a height of more than 300µm. Bubble generation problems and the related effects on the quality of the

PLGA microstructures were also successfully overcome by eliminating residual air in the microstructures during the molding process. This has proved to be the key reason that most of the reported results have much lower aspect-ratio in the microstructures.

The thickness of the PLGA sidewall in figure 3.4(C) is 50 $\mu$ m, and the depth of the chamber is 300 $\mu$ m and 8 ribs have been added to improve the mechanical strength. The bottom layer thickness of this PLGA microstructure is about 500 $\mu$ m. The rib's width is 50 $\mu$ m. Comparing with an open geometry pattern, these structures in Figure 3.4 (C) with closed geometry pattern are more difficult to be peeled off.

The chamber volumes between two neighbored rings were designed to be same. The main motivation for this design choice was to lease a constant amount of active species after each layer of cells is degraded. This design also helps to achieve a linear delivery.

The PLGA microstructures fabricated this way only have the bottom layer and the sidewalls of the micro-chambers. A covering layer needs to be made separately. A thin layer of PLGA solution was then coated on a flat PDMS sheet and baked in oven to make the covering layer that was used to seal the testing actives into the micro-chamber. The bottom part with honeycomb micro-chambers filled with actives and the covering layer were then bonded together by pressing them at raised temperature. Another optional way is to simply stack these PLGA microstructures to form multi-layer structure.

### **3.3 Experimental Results and Discussions**

To test the degrading process of the multi-layer PLGA microstructures and the release rate, a simple experiment has been designed. Sugar powder was used in the preliminary tests. Sugar powders were packaged in the micro-chambers of the sandwiched PLGA microstructures. Applying a mechanical load on the top PLGA cover layer, with 60°C for 30mins, the PLGA cover layer was sealed to the PLGA microchambers to form the drug capsule. Figure 3.5 shows a

photograph of a packaged PLGA capsule filled with sugar powder. Because the top cover layer and the bottom of the PLGA capsule are transparent, in Figure 3.5, the dark area is the coaxial ring and the ribs, the bright area is sugar powders.

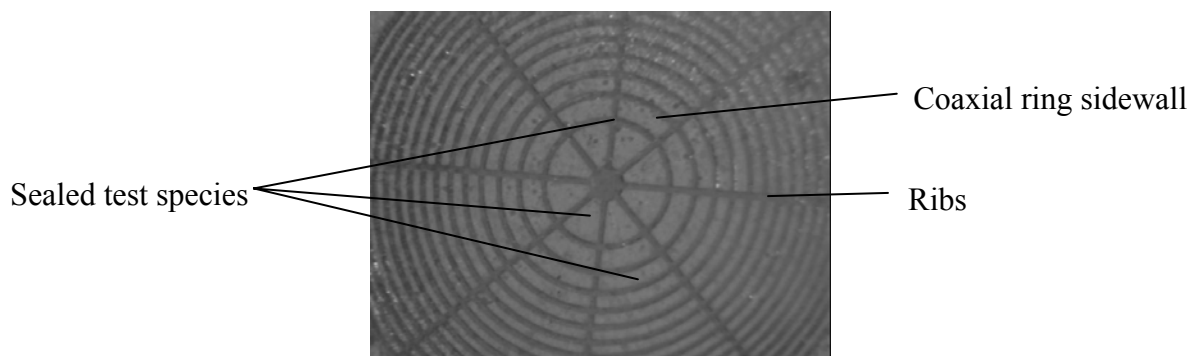


Figure 3.5 Top view of PLGA drug capsule filled with the dye powder

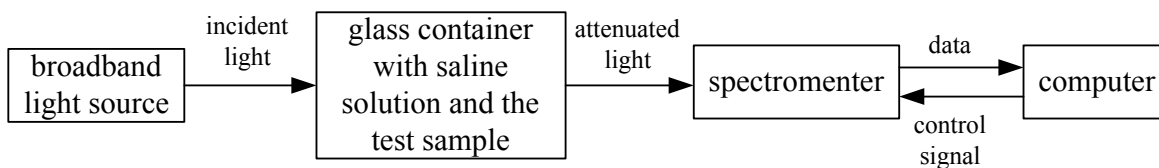


Figure 3.6 Schematic diagram of the test set-up

A simple optical measurement system was used to test the release rate of actives in saline water as shown schematically in Figure 3.6. The sealed PLGA capsule with sugar powders was dipped into 100ml 0.9% normal saline solution. A spectrometer (Ocean Optics S2000 spectrometer) was used to monitor the absorbance of the solution at a specific wavelength. If the concentration of the active material dissolved into the saline solution is proportional to the absorbance of the solution, the measurement of the absorption can be used to indirectly monitor the concentration of the released active material.

The top layer and bottom layer of sealed PLGA capsule sample are sandwiched between two silicon plates in order to avoid degrade in the vertical direction. The main reason for this is to better calibrate the degradation rate and avoid cross-talk errors. A small clap is used to provide



pressing force to hold the silicon plates and the PLGA capsules together. Two glass plates with a thickness slightly less than the sealed capsule are used to support the PLGA capsule as shown in Figure 3.7. When the PLGA polymer structures were loaded with a mechanical force of a clip, small reduction of heights may result until the silicon plates touched the supporting glass plates.

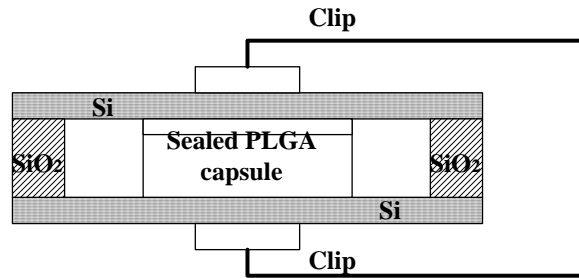


Figure 3.7. Test set-up to keep the dissolution along the radial direction of PLGA coaxial rings.

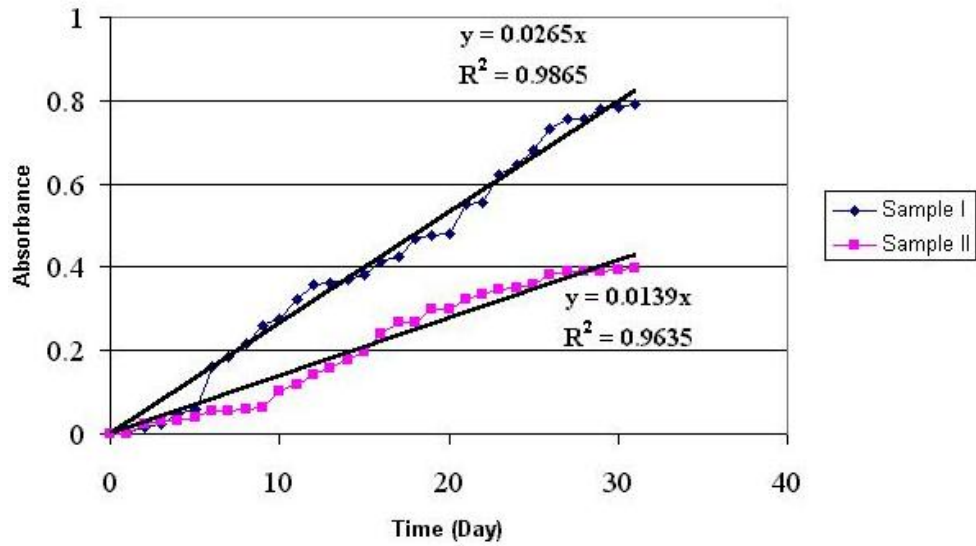


Figure 3.8. Experimental results for measured absorbance of the solution vs. time.

In the practical case of implanted drug capsules, multiple layers of microstructures are to be sealed to form a truly three-dimensional design for the capsule. In such general case, detailed mathematical model needs to be developed to numerically simulate the degradation rate of the sample capsule in implanted environment. Based on the numerical simulation results, optimal design can be developed for linear release of targeted drug. However, the one-dimensional test

model set up here is good enough for test the release rate and the degradation process of the PLGA capsule.

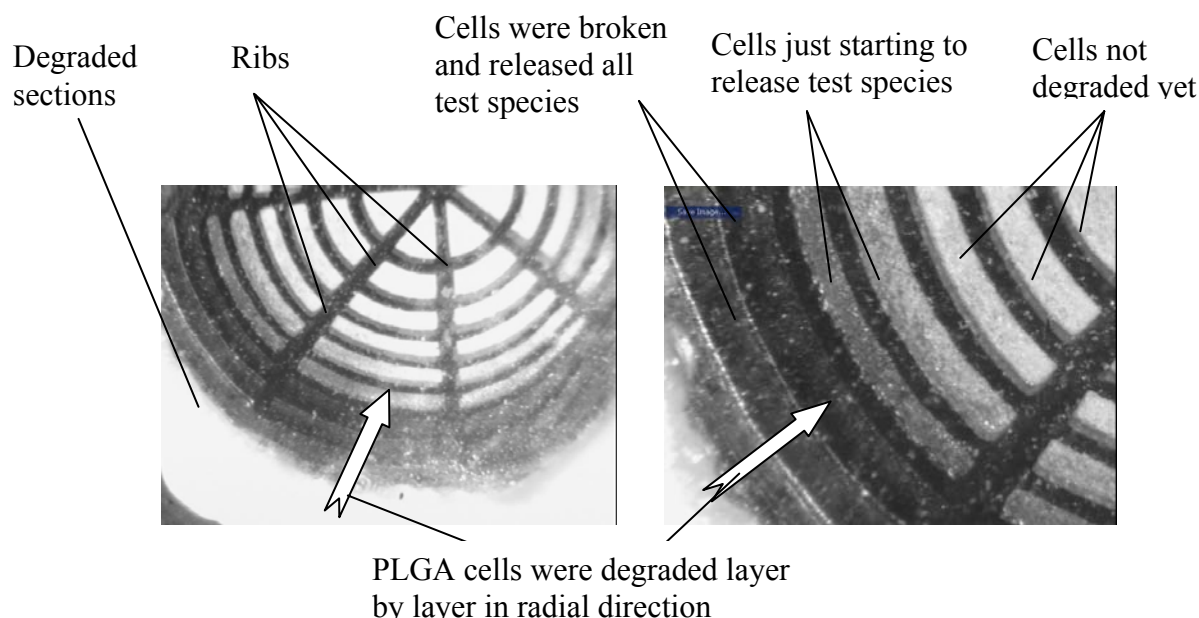


Figure 3.9 Bio-degraded drug cells (30 days in 0.9% saline water). The PLGA coaxial rings are 150  $\mu\text{m}$  wide, and 8 ribs are also 150  $\mu\text{m}$  wide.

Figure 3.8 shows a typical set of experimental results recorded for packaged sugar powder in PLGA capsule. The experiment was conducted for a period of thirty days. The sample I contains twice amount of sugar powder as in sample II, and therefore the released amount is about two times of that released from sample II. The first outer coaxial ring of sample I had some defects, which might have caused the jump in released sugar at day 5. From the experimental results, it can be seen that the degradation and the release rates are highly linear. The regression coefficients  $R^2$  for two trend-lines in Figure 3.8 for samples I and II are 0.9865 and 0.9635 respectively.

From the experimental results shown in Figure 3.8, another important observation can also be made. It seems that during a period of about five days, the measured concentration of the sample in the solution is at very stable level, then followed by a suddenly increased level. This

may be caused by the periodic degradation of PLGA sidewalls layer by layer. This is exactly what has been expected in our design and proved the feasibility of using microfabricated capsule for linear release rate of targeted actives in implanted applications.

After 30 days watch on the test species' release of the biodegradable PLGA cells in 0.9% saline water at room temperature (20°C), the sealed PLGA capsule was taken out from the saline water and remove the clip and the top and bottom Si pieces. Two photographs of the sample PLGA microstructure are shown in Figure 3.9. From the pictures, it can be seen that the coaxial rings were gradually degraded from the outermost section in a biodegradable environment. The outer sub-domains were degraded first and the actives released. At the end of the experiment, the micro-chambers in three outmost rings were completely broken; the micro-chambers in the next two rings were partially broken with saline water leaked inside. The micro chambers in central area were still in very good condition, and no saline water entered these micro-chambers. It can also be observed that the micro-chambers on the same coaxial ring seem not to be degraded at the same time. This might have been caused by the not perfect sealing conditions.

The experimental results obtained have shown that highly linear degradation and release rate can be achieved in in-situ test. Preliminary results obtained so far seems to confirm the feasibility of using this approach to achieve linear release of targeted species in a biological environment. Further experiments are still under way in our laboratory to study the release dynamics of microcapsule made with the multilayer PLGA microstructures.

## **CHAPTER 4. APPLICATIONS OF UV LITHOGRAPHY OF SU-8 IN FABRICATION OF 3D MICRO MIXER / REACTORS WITH ARRAYS OF IMPINGING MICRO JETS**

### **4.1 The Challenges in Micromixing and the State-of-the-Art in Design and Fabrication of Micro-mixers/Reactors**

The applications of the microelectromechanical systems (MEMS) technology have been spreading to all different fields of engineering and science. Micromixer and microreactor are widely used in biological and chemical Microsystems for mixing and reaction. Higher mixing efficiency is always required to increase the reaction speed and improve the sensitivity of these systems. Rapid and complete mixing of samples and reagents of micro-volumes is vital for these micro chemical and biological systems.

Unfortunately, to mix micro volumes of fluid samples in microfluidic systems is always a very difficult task. There are two basic mixing mechanisms: diffusion and convection. When the Reynolds number is high, the flow is turbulent and convection type of mixing happens. Macroscopic motion of fluids carries species from one region to another. Convection mixing is therefore very efficient.

When two flows with different concentrations of chemicals or species are brought into physical contact, redistribution of the concentrations will happen because species or chemicals will diffuse into the flow with lower density of such chemicals or species. The diffusion process can be described by the following equation:

$$x = \sqrt{2Dt} \quad (4.1)$$

where  $D$  is diffusion,  $x$  is the distance a particle travel in fluid, and  $t$  is the time span. Diffusion  $D$  of various species in water is on the order of  $1 \times 10^{-9} \text{ m}^2/\text{s}$ . For a laminar flow, the time needed for species to diffuse 1mm in water theoretically may take about 500seconds!

Because the flow in all micro-fluidic systems is laminar and has low Reynolds number, diffusion is the dominant mechanism. Various efforts have been made to improve the mixing process by introducing geometric irregularities in fluidic channels to create localized eddies and turbulences. Vijayendran, et al, suggested a three-dimensional design for micromixer consisting of a straight and a serpentine micro-channels [65]. This design forced the two samples to be mixed to flow cross each other and effectively caused the chaotic disturbance and enhanced diffusion efficiency. K. P. Kamper, et al., descried a static mixer, which took the advantages of the enlargement the interface of fluid to enhance diffusion mixing [66]. This micromixer has a long and serpentine-shape channel to maximizes the interfaces of the sample fluids. The fluids are subdivided, twisted, distorted, mixed in a LIGA fabricated micro mixer array. Schwesinger at el. [67] reported an integrated modular micromixer system by creating two cross-over flow channels that with zig-zag patterns. Two different samples are then driven to flow through the cross-over channels and forced to flow across each other and mix. M. Koch, at el. [68] presented an improved technique for mixing two different fluids by using a scheme of dividing the flow into multiple channels and then recombination. Their mixer is still mainly based on the diffusion mechanism.

Because it is very difficult to obtain high mixing efficiency with diffusion mechanism, some reported efforts used active disturbance to create turbulence in the microfluidic systems. Zhen Yang, at el. [69], proposed to use an active disturbance method with ultrasonic actuator. The ultrasonic vibration of the PZT diaphragm propagates in the flow channel and stirs the fluid

to enhance the mixture. Vivek, Zeng, and Kim [70] used a Fresnel Annular Sector Actuator (FASA) to produce and focus the acoustic vibration in their micromixer. The actuator was made with patterned Fresnel annular electrodes pairs on the both side a PZT substrate. The much stronger lateral acoustic pressure pushed and pulled the fluid for mixing.

According to the scaling law, the most effective way to maximize the effective surface area of liquid is to convert them into plumes of stream. Ryo M., et al. [71] used an array of micro-nozzles on the bottom of a wide shallow channel on a silicon substrate. The sample fluid was supplied into the channel and the reagent was ejected through these micro-nozzles into the sample at high speed. Because the micro-nozzles converted the reagent into micro-plumes, the effective contact surfaces with the sample were significantly improved. The design utilized the mechanics of both molecular diffusion and convections. The limitation of this design is that the sample itself is not converted into micro-plumes of stream because of the restriction of the planar design and fabrication technology used.

This chapter reports a new type of passive micromixers that take the advantages of both diffusion and turbulence mechanisms to improve the mixing efficiency. Compared with other types of micromixers, this new type of micromixers takes a three-dimensional approach in design and based on a fabrication process using UV lithograph of a negative type of thick resist, SU-8. It can also be easily integrated in other biochemical, biological, and chemical analysis systems.

## **4.2 Design for the Three-Dimensional Micromixers/Reactors Based on Impinging Micro-jets**

Impinging-jet mixing technology is used in chemical industry at larger scales. Mahajan and Kirwan [72] presented their research work about two-impinging jets (TIJ) mixing in which two liquid coplanar jets impinge face to face upon each other inside a mixer chamber. The mixer

is reported to have very high mixing efficiency. However, applications of TIJ based MEMS mixers have not been reported in literature so far. The main reason for it may have been due to the fact that most of the micromixers reported so far have been made using planar technologies and effective utilization of the impinging jets mixing would be too complicated.

The design for the micro mixer/reactor presented in this chapter is shown in Figure 4.1. Two arrays of micro-nozzles are located in opposite directions. These micro-nozzles are in parallel with the substrate plane. Because large arrays of micro-nozzles are used in the design of the mixer, there are two possible ways to arrange the opposite arrays of nozzles: directly opposite orientations, or to have a designed offset.

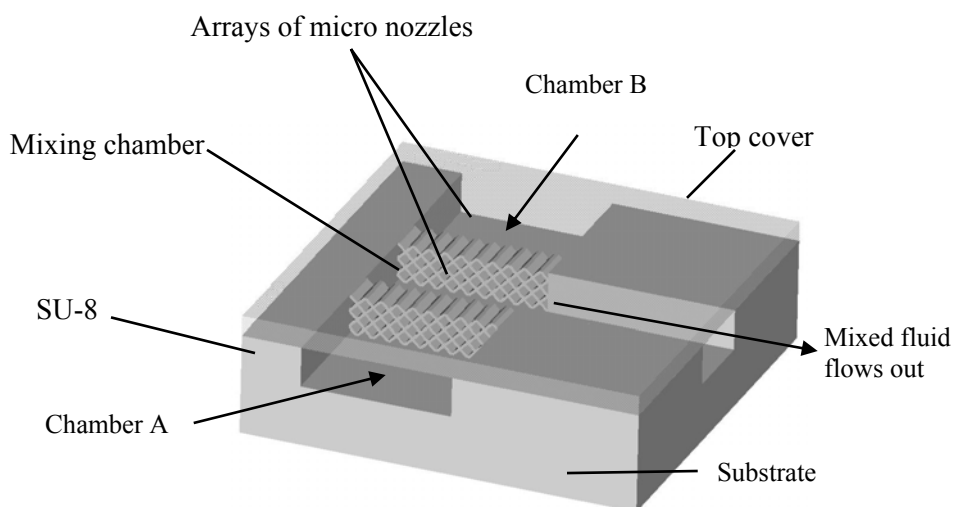


Figure 4.1. Schematic design of the proposed micro mixer/reactor.

The working principle of the micromixer reported in this chapter is similar to but better than a simple TIJ mixer. Instead of using just one pair of such jets, large arrays of spatially impinging micro-jets are used in our design. The sample fluid and the reagent are delivered to the chamber A and chamber B respectively. They are then driven into the mixing chamber via two arrays of micro nozzles. These nozzles help to convert the mixing liquids into plumes of

streams. Because these plumes of streams are injected into the mixing chamber in opposite directions, they have to pass through the surrounding outflow prior to impinge upon each other (with face-to-face nozzles) or pass by other (with offset nozzles). The large arrays of impinged micro-jets help to improve the mixing efficiency.

Figure 4.2 (A) shows a schematic diagram for the face-to-face impinging jets, and Figure 4.2(B) shows a mixer with a fixed offset. In Figure 4.2 (B), the each bunch of liquid jets from one sidewall of the mixer with a fixed offset is surround by four bunches of another kind of liquid jets from another sidewall, as shown in Figure 4.2 (C). The mixing processing is three-dimensional in both designs. This mixing process can be better understood from the following theoretical analysis based on the fundamental study presented by Mahajan and Kirwan [72].

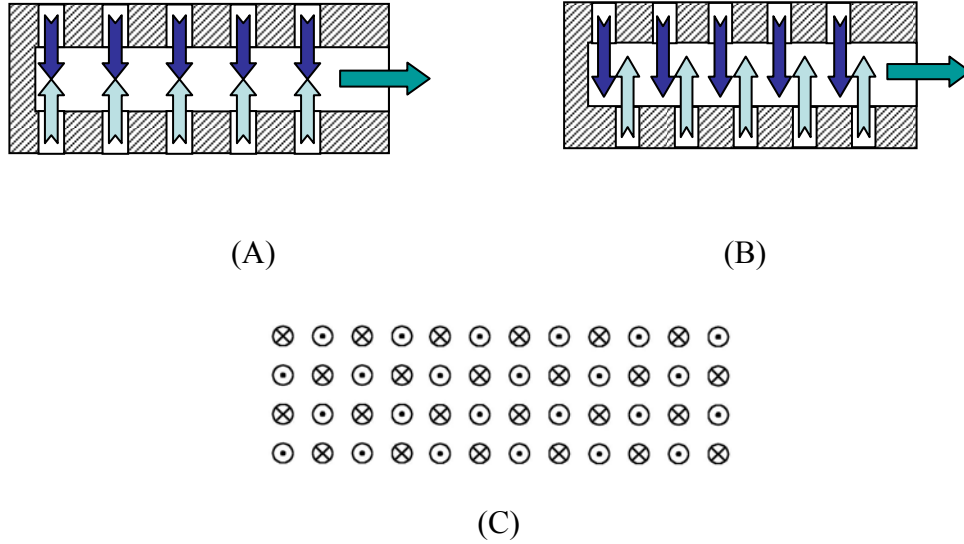


Figure 4.2. The schematic diagrams of the impinging jets. (A) Without offset; (B) With offset; (C) Cross-section view of mixing chamber as shown in (B) along the middle line,  $\odot$  stands for the jets in the direction out of the chapter and  $\otimes$  stands for the jets in the direction entering the chapter.

The time constant  $T_m$  for micromixing process can be defined as a function of diffusion  $D$  of a fluid and Kolmogoroff length  $\lambda$ ,



$$T_m = (0.5\lambda)^2 / D, \quad (4.2)$$

where  $\lambda$  can be expressed as,

$$\lambda = [\rho V \nu^3 / P]^{1/4}, \quad (4.3)$$

with  $\rho$  the mass density of liquid, P the energy dissipation rate, V the volume of liquid within which the energy is dissipated, and  $\nu$  kinetic viscosity of the fluid. P and V can only be estimated for a specific design of micromixer.

To simplify the analysis, it can be assumed the kinetic energy is completely dissipated into the mixed solution when two micro fluid jets are impinged upon each other and the velocity is reduced zero. The energy dissipation P of the fluids can then be calculated as follows,

$$P = \frac{\pi}{8} \frac{\text{Re}_1^3 \rho_1 \nu_1^3}{d_1} \left( 1 + \frac{m_1}{m_2} \right), \quad (4.4)$$

where  $m_1$  and  $m_2$  are the mass of the fluid 1 and fluid 2 to be mixed,  $\text{Re}_1$  is the Reynolds number for sample 1, and  $d_1$  is the diameter of the fluid jet 1.

If the physical properties ( $\rho$  and  $\nu$ ) of the two fluid jets are assumed to be equal, the relationship for time constant can be simplified by plugging Eqs. (4) and (3) into Eq. (2) to obtain the proportionality,

$$T_m \propto \frac{d_1^{0.5} \nu^{0.5}}{\text{Re}_1^{1.5} (1 + m_1 / m_2)^{0.5}}. \quad (4.5)$$

From Eq. (5), it can be seen that to obtain smaller mixing time constant, i.e., faster mixing, there are several options in mixer design for rapid mixing and high efficiency mixing: (1) to increase Reynolds number of the flow, a task not easy to achieve in microfluidic systems

as commonly known; (2) to reduce the diameter of the micro-jets; and (3) to reduce the volume of the jet flow, this means to reduce the total volume to be mixed.

In steady state, the mixing chamber is always filled with solution. Each pair of micro-jets must flow through the fluid in the mixing chamber before they can be impinged. The resultant flow from one particular pair of impinging jets also has to pass through the neighboring pairs of impinging jets to flow out the mixing chamber. The three-dimensional design of the TIJ array helps to form more vortexes in flow [73], and results in rapid mixing.

The mixing mechanism of the impinging jets with a given offset is much more complicated. A rough, but physically insightful explanation can be tried as follows. The offset in the design helps to make the interfacial areas between the impinging jets larger which enhance the diffusion process. The offset also permits the micro-jets to flow across the mixing chamber from one side to another to generate more vortexes. These characters make the impinging jets with offset have higher mixing efficiency than the design with face-to-face impinging.

The three-dimensional design with multilayer spatially impinged jet arrays helps to enhance the Reynolds number, increase the effective interfacial areas, convert higher percentage of the kinetic energy in microscopic molecular motions, therefore effectively boost the eddies and flow turbulences, increase Reynolds number in the micromixer chamber, and improve the diffusion effects for mixing.

#### **4.3 Fabrication of the Micro-mixer/Reactor**

The micro-mixer was fabricated using UV lithography of SU-8. Cured SU-8 is a physically strong polymer. It has excellent thermal stability and highly resistive to a wide variety of chemicals. It is also bio-compatible and can be treated with other types of bio-materials such as parylene if desired. The fabrication process to be used in fabricating this mixer

is also compatible with other micromachining process and can be easily integrated with other processes to make complicated micro fluidic systems.

A total of two lithography masks were needed. One was used to form the inlet and outlet channels, and sidewalls. Another one was used to fabricate the large arrays of micro-nozzles. The SU-8 arrays of micro-nozzles were fabricated by using a non-conventional lithography method in which a thick layer of SU-8 is exposed at 45 degree and  $-45$  degree (or other designed angles) with the designed mask [30].

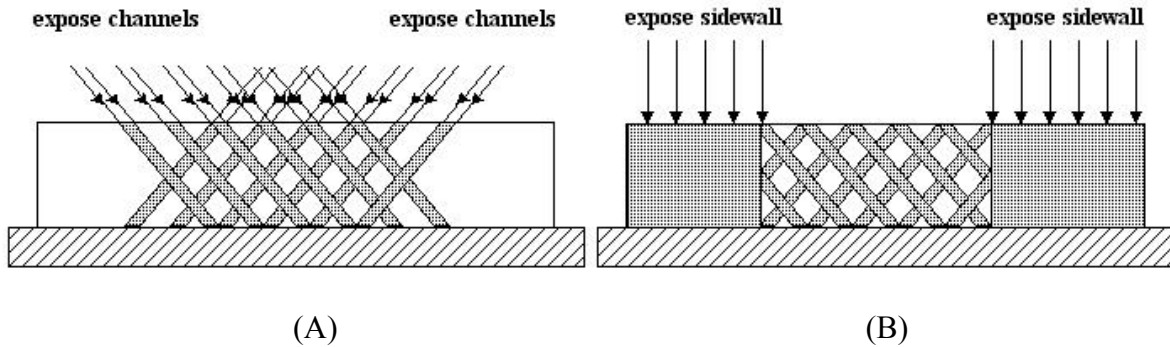


Figure 4.3. (A) Using tilted lithography of SU-8 to produce the horizontally oriented large arrays of micro-nozzles for the proposed micro-mixer, two exposures at different angles are required. (B) Using second mask to fabricate the inlet- and outlet-channel sidewalls.

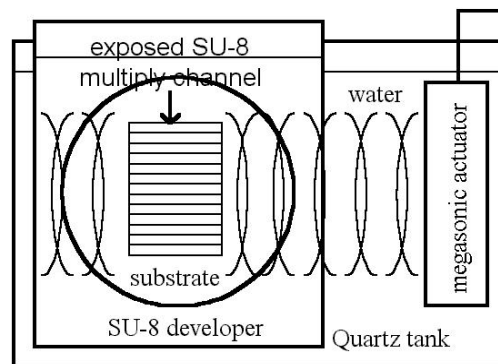


Figure 4.4. Graphic representation of the developer bath setup used in this experiment.

The tilted lithography process is schematically shown in Figure 2.15 and the principle is explained in Chapter 2. A specially designed chuck is used to hold the mask and the substrate.

The chuck permits a rotation angle of 90 degrees. As shown graphically in Figure 4.3, when two arrays of narrow strips of light beams are projected on the photo-resist, the intersection forms an array of micro channels. A conventional lithography was followed to fabricate the inlet and outlet flow channels' sidewalls as shown in Figure 4.3 (B).

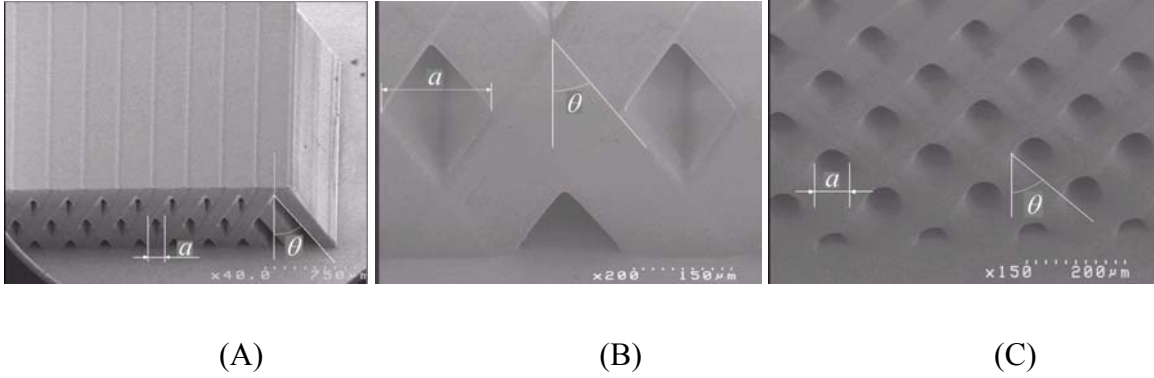


Figure 4.5. 1100 $\mu\text{m}$  thick and 2000 $\mu\text{m}$  long closed channels exposed using broadband UV lithography and developed on thin exposed SU-8 under layer using mega-sonic development. The angles and the diagonal lengths are measured by Nikon MM-22U microscope. (A) light incident angle  $\theta = 28.1^\circ$ , the horizontal diagonal of the micro-nozzle  $a = 87.4\mu\text{m}$  (B)  $\theta = 30.9^\circ$ ,  $a = 153.2\mu\text{m}$  (C)  $\theta = 45.1^\circ$ ,  $a = 45.6\mu\text{m}$ .

In the fabrication process, silicon substrate was spun-coated with SU-8 100 negative photoresist at 400rpm for 1100 $\mu\text{m}$  thickness and bake at 110 $^\circ\text{C}$  for 10 hours then cooled to room temperature over an 8 hour time interval. Exposure was completed on an Oriel UV exposure station. After exposure the substrates were postbaked at 96 $^\circ\text{C}$  for 25 min. and cooled to room temperature again over an interval of 8 hours.

It is very difficult to fully develop horizontally orientated micro-nozzles. The development solution cannot effectively work into deep and narrow structures with simple stirring. The development may take many hours, damage fine features, and may still not be fully developed. This has been one of the challenging issues in SU-8 based fabrication process. Development was performed using a SONOSYS megasonic actuator driven with a 250 W power

supply. The megasonic transducer was placed in a water bath supporting a quartz tank in which the developer and substrate were located. Wafers were perpendicular with the megasonic actuator face to make the channels along with the propagation direction of the megasonic wave. Figure 4.4 shows a schematic diagram of the experimental setup.

Figure 4.5 shows some developed multi-layer of micro channels fabricated with the UV lithography of SU-8. The channels in Figure 4.5 (A) are 125 $\mu$ m width and 2000 $\mu$ m length. In Figure 4.5 (B) is close-in picture of the channel with 75 $\mu$ m width and 2000 $\mu$ m length. In Figure 4.5 (C) the channels are about 30 $\mu$ m wide.

The fabrication flowchart for production of the micro-mixer/reactor is shown as: (1) Clean the substrate using acetone, IPA, and plasma ash; spin coat SU-8 and bake the sample at 1100C for 10 hours, followed by 8~9 hours cooling down; (2) Using Mask #1 to do +45 degrees title exposures; (3) Using Mask #2 to align and exposure the sidewalls, inlet and outlet channels; (4) Development using megasonic agitation; (5) Bonding the cover glass; (6) Using glues to seal the inlet and outlet with flow connectors

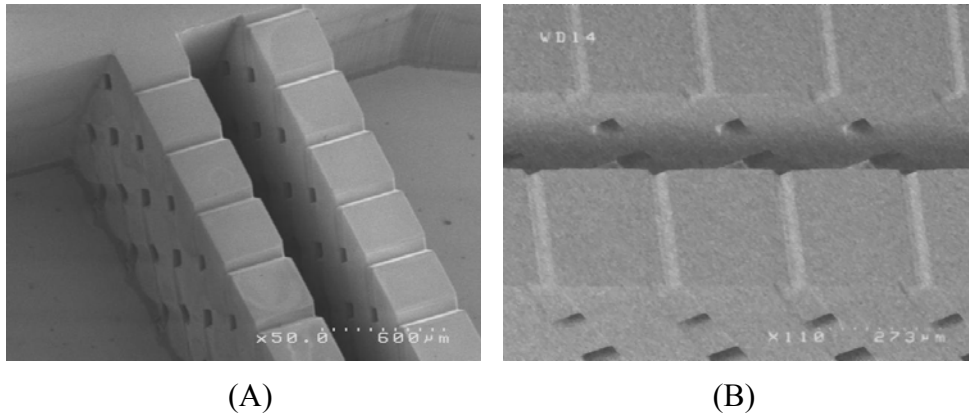


Figure 4.6. (A) SEM image of the bottom part of a typical prototype micro-mixer made with cured SU-8 polymer. (B) A close-in image of mixing chamber and nozzles.

Figure 4.6 shows a fabricated micromixer with inlet and outlet tubes. The cover glass is fueled silicon. The inlet and outlet tubes are sealed with epoxy.

#### 4.4 Experiments and Discussions

The measurement setup is shown in the Figure 4.7. Two BD plastic syringes were seated on a syringe pump. One syringe contains DI water and another contains fluorescein dye (Aldrich Chemical Company, Inc. Catalog # F245-6) solution with 1.2 mMol/L concentration. The syringe pump (Harvard Apparatus' PicoPlus) was used to control the flow rate of the two syringes so that the flow rate at left-inlet and right-inlet are the same. Fluorescein dye solution and DI water are pumped through the arrays of the micro-jets into the mixing chamber. The mixed solution flows out the outlet channel. A mercury lamp was used to project illumination light through the microscope onto the mixing chamber. The emission light and the reflected light from the mixing chamber were filtered using an optical filter, which permits mainly the emission light to pass through. The images of mixing flow are magnified with a microscope. A Nikon CV-252 digital video camera was used to monitor the mixing process. This standard NTSC video camera catches 30 frames (actually 29.97) per second, and two fields per frame.

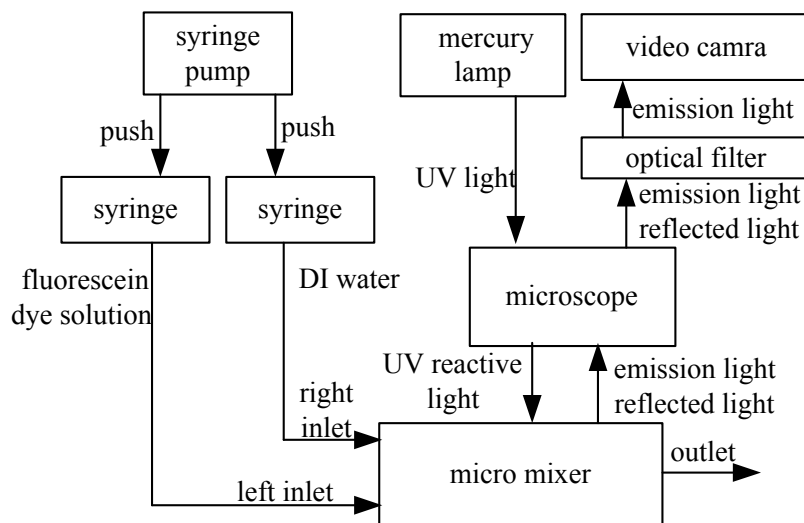


Figure 4.7. Experiment setup

Fluoresce dye solution was pumped from left-side array of micro nozzles and DI water from the right-side array of nozzles into the mixing chamber. The mixing efficiency can be monitored based on the gray scale distribution in the photo images of the CCD camera video. In the photo image of the mixing chamber, the region with high concentration of fluoresce dye would be brighter than that with lower fluoresce dye concentration. Because the video camera used in the experiments has very limited depth of focus (DOF), the images of the mixing process obtained are only a thin layer liquid in the mixing chamber. For all of the pictures shown, only one layer of jet nozzles' image are visible, the images of other layers are vague.

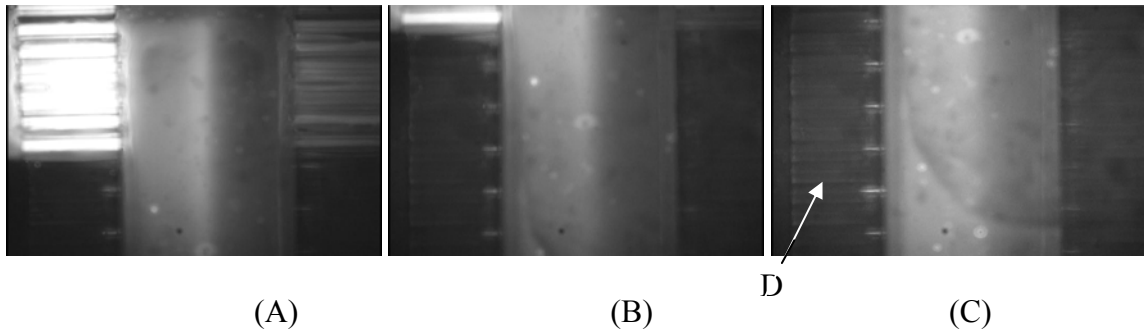


Figure 4.8. Experimental results for one of the prototype micro-mixer based on arrays of impinging jets without offset. (A) Photograph of the flow in the mixing chamber; (B) Photograph was taken 1mm down stream; (C) Photograph taken 2mm down stream along the outlet channel. (D) Because the SU-8 in these structures has different exposure dosage and different optical refraction index, they look like jet channels but no holes inside.

Figure 4.8 shows the test results for a prototype micromixer based on spatially impinged TIJ arrays without offset (normal impinging conditions). The distance (width of the chamber) between two arrays of nozzles is  $1000\mu\text{m}$ . The depth of the mixing chamber is  $1000\mu\text{m}$ . The cross-section area of the nozzles for the mixer shown in Figure 4.9 is  $70\mu\text{m}$  by  $70\mu\text{m}$ . The flow rate used was  $20\mu\text{L}/\text{min}$ . Pictures were taken out from the video using Adobe Premiere Pro software [Adobe Systems Incorporated, San Jose, CA]. The video is in NTSC format, with 30 frames per second. Fluoresce dye solution and DI water were normally impinged and seemed to

form a boundary region in the center of the mixing chamber as can be observed in Figure 4.8 (A). The photographs of (B) and (C) were taken from 1mm and 2 mm downstream along the outlet channel. As can be seen from photographs (B) and (C), the solution is fairly well mixed only very short distance downstream.

In the photographs shown in Figure 4.8 (B) and 4.8 (C), the images of the sidewalls seem to contain some imbedded nozzles. These structures are not through-holes and formed by multiple exposures during fabrication process. For simpler mask designs, regions immediate outside the mixing chamber were also covered by patterns of micro-nozzles during the first exposure. These regions were then exposed again using the second mask to form the outlet sidewall. The double-exposed regions on sidewalls have slightly different optical properties and formed the channel-like images.

Figure 4.9 shows the test results for a prototype micromixer with a designed offset between impinging micro-jet arrays as shown in Figure 4.2 (B). Fluoresce dye solution and DI water were pumped into the mixing chamber in opposite directions. The distance between two arrays of nozzles is  $210\mu\text{m}$ . The depth of the mixing chamber is  $1000\mu\text{m}$ , and the length of the chamber is  $5000\mu\text{m}$ . The physical sizes of the nozzles and the flow rate used are the same as used in the prototype micromixer shown the Figure 4.8.

The photographs shown in Figure 4.9 were taken at different times as fluoresce dye solution and DI water were pumped into the mixing chamber. The flow rate of the inlet fluoresce dye solution and DI water was at  $20\mu\text{l}$  per minute. From the experimental results as shown in Figure 4.9, it can be seen that mixing process is completed within less than one second for this particular prototype mixer at the specified test conditions.



For all of the prototype mixers with offset, the mixing process is completed locally inside the mixing chamber. For the prototype mixers without offset (normally impinged TIJs), experiments show that the mixing process is finished only a short distance downstream along the outlet channel.

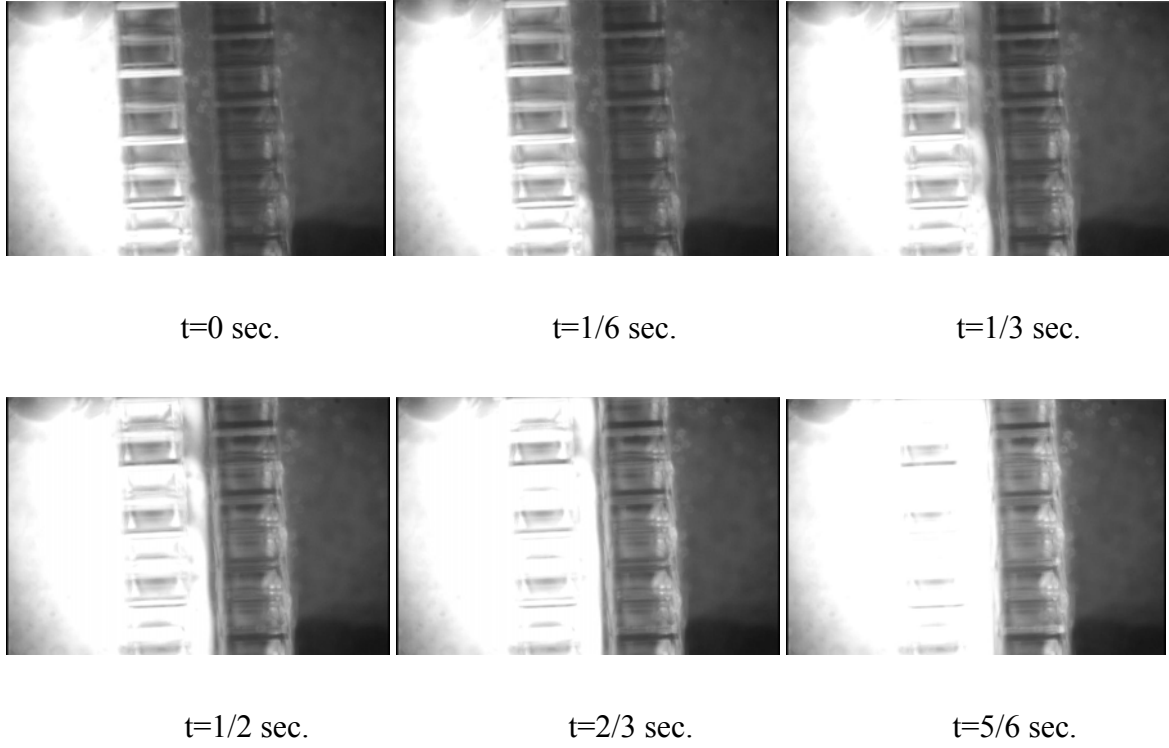


Figure 4.9. Experimental results for one of the prototype micro-mixer with offset

The Reynolds number in the micro nozzles of the micro mixer/reactor can be estimated for the given test conditions to help to understand the mixing mechanism.

If the incident angle of the lithography angle is  $\theta$  in SU-8 photoresist, the micro-nozzles fabricated may have a no-square cross-section as shown in Figure 4.5 (B) as a function of angle  $\theta$ . Assuming  $a$  is the diagonal of the micro-nozzle in the plane of the substrate as show in Figure 4.5,  $V$  is the flow velocity, and  $d$  is the hydraulic diameter,  $Q$  is volume flow rate,  $A$  is the cross-

sectional area of the micro-nozzles,  $N$  stands for number of the nozzles, the equation for Reynolds number is shown as following:

$$\text{Re} = \frac{\rho V d}{\mu} = \frac{\rho Q \cdot a \cdot \cos \theta}{\mu \cdot A \cdot N}, \quad (4.6)$$

where  $\rho$  is the density of the liquid,  $\mu$  is the dynamical viscosity, and assuming the flow can wet the corner of the nozzles' cross sectional area. Equation 4.6 shows the relationship between the number of nozzles and cross-sectional area.

For the prototype micromixers tested in Figure 4.8 and 4.9, the length of the micro-nozzles is 300 $\mu\text{m}$ . The structures used for the experiments shown in Figure 4.9, the lithography angle  $\theta$  inside SU-8 is about 28°; the depth of mixer chamber is 1000 $\mu\text{m}$ , length of the mixing chamber is 5000 $\mu\text{m}$ , the diagonal of the cross-section area of nozzle  $a$  is 70 $\mu\text{m}$ . With input flow rate  $Q = 20\mu\text{L}/\text{min}$ , the flow velocity in the nozzles can be estimated as about 0.00167m/s and the Reynolds number can also be estimated to be about 0.1456 based on the geometry dimensions. Compared with the Reynolds number of 0.0002 at the input channels of DI water and fluoresce dye solution just before liquid enter the nozzles, the Reynolds number in the nozzles increases about 728 times.

With Reynolds number at this low level, it would normally be expected that the mixing process would be extremely slow. However, experimental results show that the prototype micro mixers based on spatially impinged jet arrays with an offset still can locally mix the two flows in less than one second. Very obviously, the diffusion mechanism should not be what behind this rapid mixing process.

For the prototype micromixers tested in Figure 4.8 and 4.9, the cross-section area of the micro nozzle is 9215.56  $\mu\text{m}^2$ , the inlet flow rate  $Q = 20\mu\text{L}/\text{min}$ . There are about 21.7 micro-

nozzles, and the flow rate in each micro nozzle can be estimated as  $20\mu\text{L}/\text{min}/21.7=0.9217\mu\text{L}/\text{min}=1.536\times 10^{-11}\text{m}^3/\text{s}$ . The pressure drop caused by the micro nozzle can be estimated as:

$$\Delta P = N \cdot \frac{\rho}{2 \cdot C_d^2 \cdot A_0^2} \cdot Q^2 = 21.7 \cdot \frac{10^3 \text{ kg/m}^3}{2 \cdot 0.62^2 \cdot (9.216 \cdot 10^{-9} \text{ m}^2)^2} \cdot (1.536 \cdot 10^{-11} \text{ m}^3/\text{s})^2 = 78.4 \text{ Pa}, \quad (4.7)$$

where  $N$  is the total number of nozzles on each sidewall,  $C_d = 0.62$  is the discharge coefficient,  $A_0$  is the cross-section area of the micro nozzle,  $\rho$  is the liquid density.

The pressure drop between the inlet and outlet were measured using a Netscanner Pressure Systems. For an inlet flow rate  $Q$  of  $20\mu\text{L}/\text{min}$ , the inlet flow pressure was measured at 14.72963 psi and outlet flow pressure at 14.7psi. So the pressure drop between the inlet and chamber outlet was 0.02963psi (204.3Pa). Compared with the estimated pressure drop caused by the micro nozzle array, this number is larger, because the micro-channels and the mixer chamber also caused some pressure drop. The measured pressure drop confirmed that the pressure drop involved with the mixer is very low.

A complete fluid dynamic analysis for what exactly happens in the mixing chamber is out of the scope of this research project. However, there are still some basic observations can be made based on the observation of the experimental results. First, the mixers based on arrays of TIJ with offset seem to have better mixing efficiency. This may be caused by increased flow eddies generated and increased interfacial contacts. Second, it seems that mixers with a narrower mixing chamber (shorter gap between facing micro-jets) seem to provide higher mixing efficiency. This may be caused by the higher possibility for micro-jets to travel to the opposite side of the chamber to achieve better interfacial contacts with coming jets to be mixed. Last, smaller size and larger number of micro-nozzles seems to boast the mixing efficiency. This is

very understandable because the smaller and more evenly distributed streams help to boost the interfacial contacts of flows to be mixed.

The experimental results show that very rapid mixing with low pressure drop can be achieved. Because of the complex nature of fluid dynamic problems involved, only a qualitative explanation was provided at this stage. Further study is needed to fully understand the fluid dynamics involved in these impinging jet arrays.

## CHAPTER 5. FABRICATION OF A NOVEL HYDRO-FOCUSING UNIT FOR MICRO FLOW CYTOMETRY USING UV LITHOGRAPHY OF SU-8

### 5.1 Basic Principle of Conventional Flow Cytometry and the Advantages of a Truly Three-Dimensional Hydrofocusing Unit

Flow cytometric devices are very important for a wide range of biomedical research and clinical diagnostics. Conventional-sized flow cytometers are not novel and are widely used both in research and for clinical diagnostic purposes. Currently available commercial flow cytometers tend to be large and very expensive. The analytical sample is injected into the system, diluted, labeled, hydro-focused, and the cells are counted and sized by fluorimetric and electrical means. Figure 5.1 shows the principle of operation for the hydro-focusing unit of conventional flow cytometers. The cells are labeled and driven to flow through a nozzle so that light scattering or fluorescence measurements can be used for analyses.

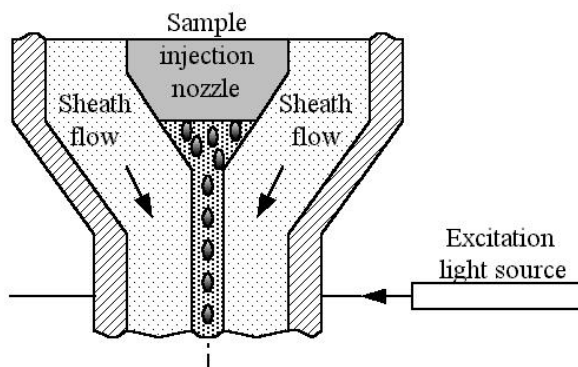


Figure 5.1 The operation principle of the conventional flow cytometer based on sample focusing and optical measurement principles

Many research efforts have been made in developing different types of micro-cytometry systems [74-84]. Micro-sized flow cytometry devices and components offer many potential benefits, including the ability to reduce device and sample sizes, development of low cost,

single-use disposable devices, and improved device portability for field use along with low consumption of sample and buffer fluids, and reduction in the biohazard risk level.

In microfabricated flow cytometers, micro grooves are etched on a substrate such as silicon or glass. With a glass or polymer cover bonded on the top, micro channels are created to form a chamber with a size that permits cells to pass through a sensing unit for categorization and enumeration [79]. Because it is very difficult to develop a truly microfabricated cytometer, some researchers have tried to avoid the difficulties of complicated microfluidic systems and micro optical systems. Weigl, Bardell and et al. [74, 77, 80-84] have used a simple design based on fluid/fluid extraction and developed a complete passive fluidic device that can be used to separate cells. The principle of hydro-focusing in a microchannel is based on the laminating cells with sheath flow. Their sample focusing system is only focused in the plane of substrate, not in the vertical direction between the top and bottom planes. In the vertical direction, fluid friction may make the cells not well focused. The cells along vertical direction therefore have different flow velocities. Lee, Lin, and Chang reported a microfabricated flow cytometer with a planary flow focusing unit and optical fiber based counter [78]. Takagi et al. [75, 76] reported based on new type of sheath flow chamber with developed using micro machining. The chamber is formed by laminating three 100- $\mu\text{m}$ -thick, photo etched, metal plates. Ramsey et al. [85, 86] also reported successful development of microchip flow cytometry using electrokinetic focusing principle.

Most of the reported focusing units for cytometers based on sheath flow are two-dimensional ones. In these designs, the sample is only focused in the plane of substrate. In the vertical direction, the fluid friction may cause the cells not well focused as shown in Figure 5.2(A). In an ideal situation, it would be much better to have a truly 3-D system so that sample is

focused in both the substrate plane and the vertical direction as shown schematically in Figure 5.2(B).

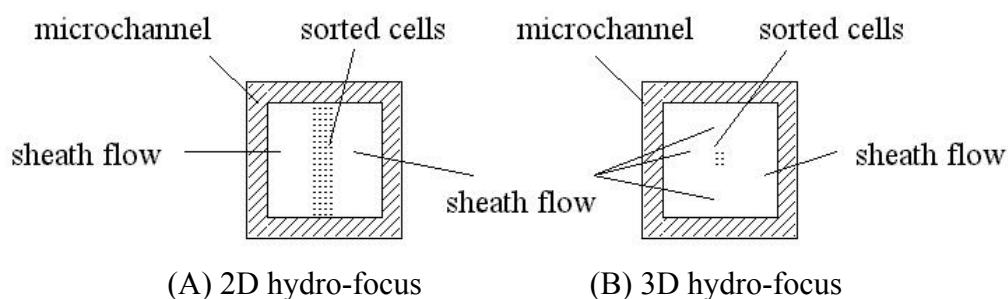


Figure 5.2 Difference in 2D versus 3D hydro-focusing in the cross-section of flow stream

Goranovic et al. [87] microfabricated a micro cell sorter with a “chimney” structure in silicon by reactive ion etching (RIE). Three-dimensional flow sheathing was obtained by injecting a sample into the sheath flow in a perpendicular direction. The limitations are that design requires a quite complicated fabrication process and is silicon based. For many biomedical/biochemistry applications, however, polymeric materials such as cured SU-8 offers unique advantages because of lower cost and good biocompatibility. Like most of the polymer-based systems, cured SU-8 may be used to construct complete systems rather than as simply a resist for the lithography process.

This chapter presents a true three-dimensional hydro-focusing microstructure made within cured SU-8, which allows the cells to flow in the core stream with an almost uniform velocity.

## 5.2 Design of the Three-dimensional Hydro-focusing Microfluidic Unit

All conventional flow cytometers are designed to have a flow chamber with a nozzle, and are based on the principle of laminating cells with the sheath flow. The microfluidic unit in a flow cytometer needs to have cells in suspension flow within a single column (if possible) through an illuminated volume. In most instruments, this function is accomplished by injecting a

small volume of sample flow through a small (50-150  $\mu\text{m}$ ) nozzle into a much larger volume of sheath fluids. Both the sheath flow and sample flow require a small Reynolds number (when  $\text{Re} < 2300$ , flow is always laminar).

In order to achieve 3-dimensional hydro-focus, the sample needs to be injected into the microfluidic unit, which then manipulate the flow rates using a gradually shrinking cross-sectional area along the flow direction to obtain a pressure gradient. Sheath volume flow rate normally is much larger than the sample volume flow rate. In the micro flow cytometer, the flow rates of sample and sheath flows are determined by the sizes of the microchannels and the focusing core stream. In addition, the section of the outlet microchannel serves as the illumination point for fluorescent emission. Compared with the other three types of flow channel in flow cytometers (jet-in-air, closed-cross-flow, and open-flow-across-surface), microchannels with a flow-through cuvette have both cell sorting function and excellent optical properties. Thus, it is the best choice for an integrated micro cytometer.

Based on the working requirements and the microfabrication limitations of UV lithography in SU-8, a 3D hydro-focusing unit for micro flow cytometry was designed as shown by the schematic diagram in Figure 5.3 (A). There are three inlets for the hydro-focusing microfluidic unit. Left-side and right-side inlets are for the sheath flow, the center inlet is for the sample flow. In the center of the end of this sample flow inlet, there is a diamond-shaped nozzle with a width of 100  $\mu\text{m}$ . There are three slopes formed by tilt-exposed, cross-linked SU-8 polymer in which the center slope is configured to a  $30^\circ$  angle with the substrate. The flat covering glass and sloped-bottom help to focus the flow upward to a central region in the direction perpendicular to the substrate. The left-side slope, right-side slope, and the two sloped-sidewalls



perpendicular to the substrate assist in achieving flow to the central region in a horizontal direction.

The sample flow is injected from the center inlet into the hydrofocusing chamber. Because of the symmetry of the left sloped-sidewall, the right sloped-sidewall, the left-side slope, and the right-side slope, the sample flow will be focused in the center axis of the outlet channel from the top view, as shown in Figure 5.3 (B). If the focusing chamber is sealed using a flat surface, the design is not symmetrical in the vertical direction, and thus the focused sample will be pushed upward, and there will be a slight off-set between the focused sample flow and the central axis of the outlet channel, as shown by the side view schematic diagram in Figure 5.3 (C). The outlet channel consists of cured SU-8 polymer and a glass plate, both of which have good optical properties and are suitable for an integrated micro optical measurement system to be incorporated in the future [24, 26].

Figure 5.4 shows schematically how hydro-focusing occurs as a laminar flow enters the three-dimensional hydrofocusing unit as shown in Figure 5.3. If the liquid is incompressible, nonviscous, and has laminar flow, the flow passing section AB and CD will be focused on section A'B' and C'D' respectively. From Figure 5.4(B), it can be seen that as sample stream flows along the channel, the vertical dimension of the chamber is reduced by the bottom slope, similar to what happened in the substrate plane. This means that some vertical focusing is achieved, though not as good as in the horizontal plane.

Another option is to replace the flat covering glass with a modified structure similar to the bottom part. The only difference is the sample injection nozzle is removed onto the axis of the outlet channel. The hydrofocusing function can then be achieved equally in both vertical and horizontal directions, the system becomes truly three-dimensional.

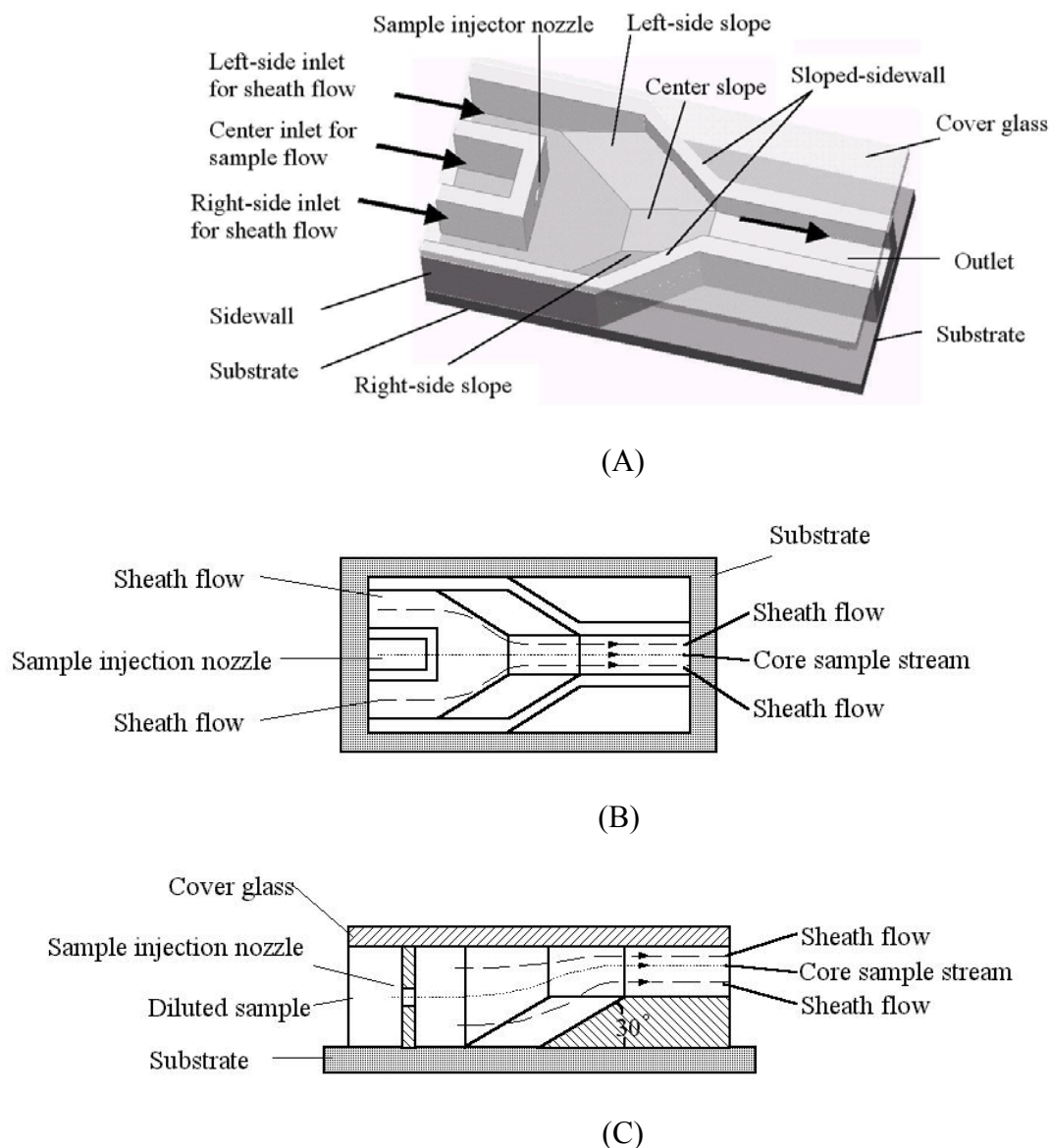


Figure 5.3. (A) Schematic of the 3D hydro-focusing unit (B) Top view of the hydrofocusing function (C) Cross-section view of the hydro-focusing function, in which ▨ stands for the cured SU-8, ▩ stands for the substrate, ▤ stands for the cover glass.

This approach may slightly improve the focusing effect in the perpendicular direction. However, it also increases the difficulty of assembly.

The 3-D hydro-focusing unit was fabricated using UV lithography of SU-8. Cured SU-8 is a physically strong polymer and is well suited as a structural material for this application. It has excellent thermal stability and is highly resistive to a wide variety of chemicals. It is also

biocompatible and can be treated with other types of biomaterials such as parylene, if desired. The process used in fabrication of this 3D hydro-focusing unit is also compatible with other micromachining processes and can be easily integrated with other processes to create complicated micro fluidic systems.

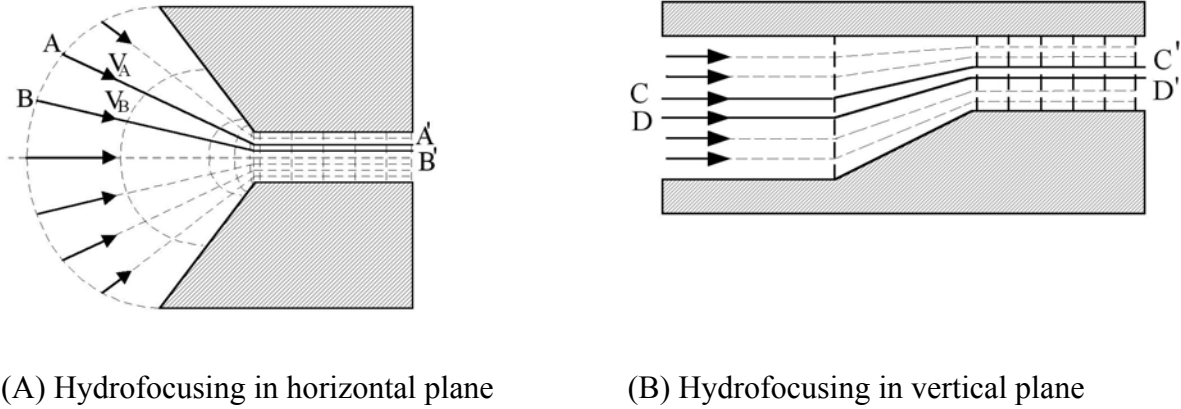


Figure 5.4. Schematic diagrams showing laminar flow in the prototype three-dimensional hydrofocusing unit with flat top cover.

Three lithography masks were needed. The first was used to form the three slope surfaces; the second was used to make the sample injector nozzle; and the last one was used to fabricate the channel sidewalls.

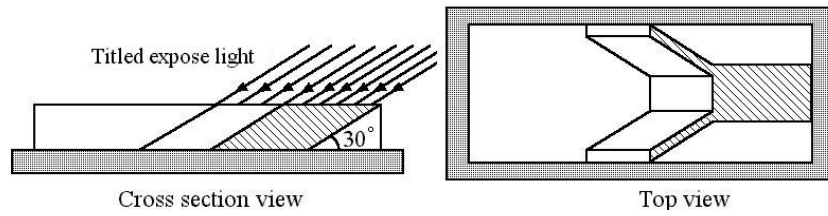
The sloped surfaces of SU-8 polymer in the hydro-focusing unit were fabricated using a non-conventional lithography method in which a thick layer of SU-8 was exposed at a specific tilted angle with respect to the substrate surface. Because SU-8 is a negative resist, exposed regions were kept and unexposed regions were removed in the development process.

The fabrication process for the hydrofocusing unit is schematically shown in Figure 5.5 (A) and (B). A specially designed chuck was used to hold the mask and the substrate. The chuck permits a rotation angle of up to 90 degrees. As shown graphically in Figure 5.5 (A), when light source is projected on the photoresist at 60 degrees respective to the substrate, three sloped

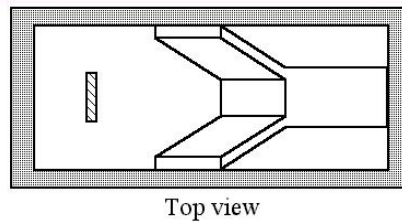
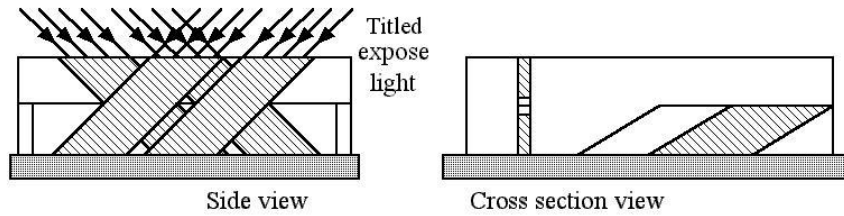
surfaces are formed. In the second step of the fabrication as shown in Figure 5.5 (B), the resist was exposed at 45 degree and -45 degree respectively to have two narrow strips of photoresist exposed. After development, the intersection forms a diamond-shaped sample injection nozzle (center inlet in Figure 5.4(A)). Finally, conventional lithography was utilized to fabricate the inlet and outlet flow channels in Figure 5.5 (C). This last step aids in fabricating all of the vertical sidewalls as shown in the diagrams of Figure 5.4.

The basic principle of tilted lithography for SU-8 can be explained using the schematic diagram in Figure 2.15 and Figure 2.16 in Chapter 2. Because the refraction of the light at the surface of the SU-8 resist, a light beam projected on the resist at 45 degrees may propagate at a reduced angle. Based on the refraction index of SU-8 ( $n=1.668$  at  $\lambda=365\text{nm}$ ,  $n=1.650$  at  $\lambda=405\text{nm}$ ), it was calculated to be roughly at about 25.24 degrees as shown in Figure 2.15. In some applications, if the channel's design requires the intersections with an angle greater than  $36.8^\circ$  at 365nm,  $37.3^\circ$  at 405nm (critical angle), a coupling prism and optical liquid are required to compensate for the refraction effect [16-18] as shown in Figure 2.16 in Chapter 2. If the diamond-shaped nozzle with intersection less than 37 degrees is acceptable, the lithography can be done without compensation provided by a coupling prism and optical liquid.

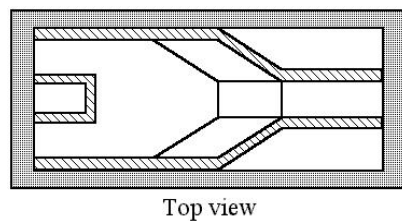
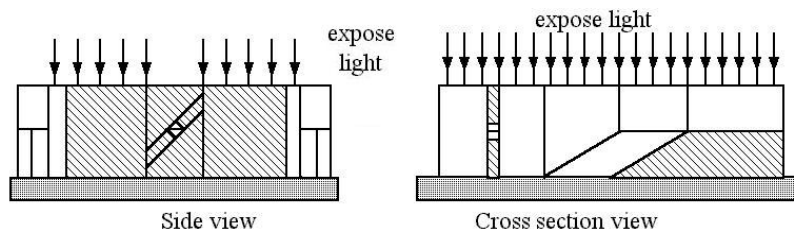
If a 90 degrees intersection is needed for a square-shaped sample injector nozzle, the required prism and the compensation principle[24, 26, 28] are shown in Figure 2.16 in Chapter 2. The geometrical relations are shown in Equation 2.6 to 2.10. The substrate therefore needs to be kept at  $45^\circ+8.32^\circ=53.32^\circ$  with respect to the horizontal plane as shown in Figure 2.16 to completely compensate for the refraction at the interface to obtain a 90 degrees intersection as required for a square-shaped injector nozzle.



(A)



(B)



(C)

Figure 5.5. (A) 60° angle tilt exposes SU-8 to obtain slopes having 30° angle with the substrate (B) 45° angle tilt exposes SU-8 to obtain suspended sample injector nozzle in the center position of the sample inlet end (C) expose all of SU-8 sidewalls. In (A), (B) and (C), ▨ stands for the cured SU-8 cross-section area, ▩ stands for the substrate, ▤ stands for the cover glass.

To obtain the slopes of 30 degrees in SU-8 with respect to the substrate,  $\theta_7$  is calculated as  $41.67^\circ$  based on the position relationship as shown in Figure 2.16. Thus, the substrate needs to be maintained at  $86.674^\circ$  with respect to the horizontal level, which is too difficult to achieve. If the prism position is rearranged as shown in Figure 2.17, the required tilt angle for substrate can be reduced to a reasonable range as shown in Figure 5.6.

If  $\theta_1$ , the exposure angle of SU-8 resist, needs to be  $60^\circ$ , from Snell's law as shown in Equation 2.6 in Chapter 2,  $\theta_5$  can be obtained as

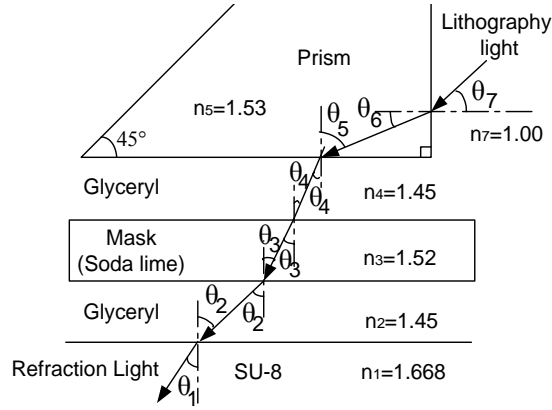


Figure 5.6, Position of prism, optical liquid, mask and resist for  $30^\circ$  slope

$$\theta_5 = \sin^{-1}\left(\frac{n_1 \sin \theta_1}{n_5}\right) = \sin^{-1}\left(\frac{1.668 \times \sin 60^\circ}{1.53}\right) = 70.76^\circ. \quad (6.1)$$

From geometry relationship, we know

$$\theta_6 = 90^\circ - \theta_5 = 90^\circ - 70.76^\circ = 19.24^\circ. \quad (6.2)$$

From Snell's law,  $\theta_7$  can be obtained:

$$\theta_7 = \sin^{-1}\left(\frac{n_6 \sin \theta_6}{n_7}\right) = 30.279^\circ. \quad (6.3)$$

The substrate therefore needs to be kept  $90-30.28=59.72^\circ$  with respect to the horizontal plane in the lithography process to completely compensate for the refraction at the interface to obtain a  $60^\circ$  incident angle in SU-8 (to get  $30^\circ$  slopes with the substrate).

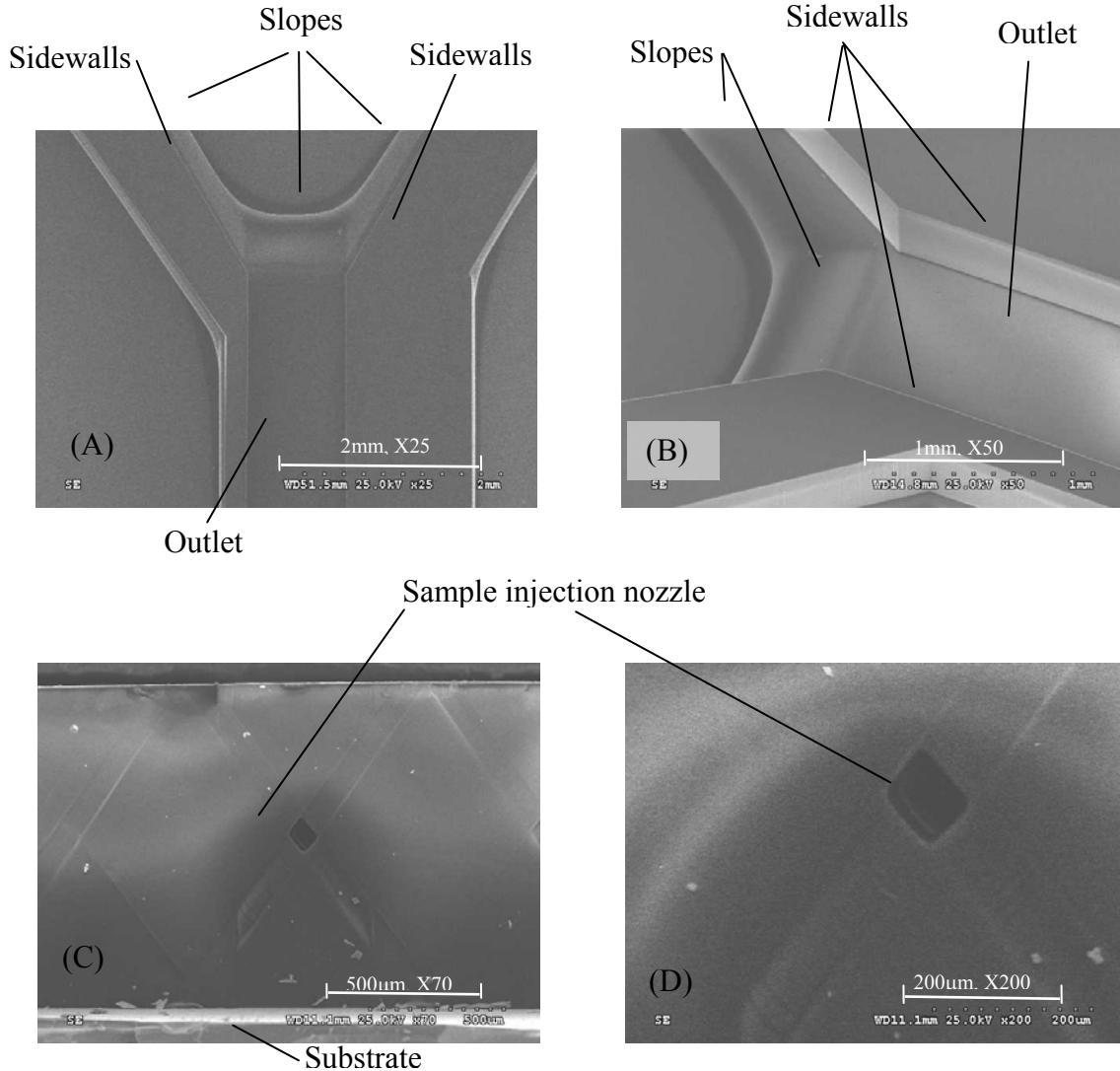


Figure 5.7. SEM photographs of the fabricated hydrodynamic focusing unit

The fabrication procedures are as follow: (1) clean the Si wafer or glass substrate; (2) spin-coat SU-8 100 photo resist with 890 rpm to obtain 500  $\mu\text{m}$  thick resist layer; (3) pre-bake at  $96^\circ\text{C}$  for 5 hours, cool down to  $60^\circ\text{C}$  within 1 hour and remain at  $60^\circ\text{C}$  for 3 hours, then cool down to room temperature in 2 hours; (4) conduct a  $60^\circ$  tilted-exposure of SU-8 with the help of

prism and optical liquid for refraction compensation. This produced slopes tilted at  $30^\circ$  with respect to the substrate [24, 26] as shown in Figure 5.6 (A); (5) post-bake the sample at  $96^\circ\text{C}$  for 20 minutes, cool down to  $60^\circ\text{C}$  in 1 hour and remain at  $60^\circ\text{C}$  in 3 hours, then cool down to room temperature in 2 hours; (6) spin coat SU-8 100 photo resist with 890 rpm to obtain the second  $500\text{ }\mu\text{m}$  thick resist layer; (7) pre-bake the sample at  $110^\circ\text{C}$  for 5 hours, cool down to  $60^\circ\text{C}$  in 1 hour and kept at  $60^\circ\text{C}$  for 5 hours, then cool down to room temperature in 3 hours; (8)  $45^\circ$  angle tilted-exposure of SU-8 with correction prism and optical liquid to obtain suspended sample injector nozzle in the center of the sample inlet end, as shown in Figure 5.6 (B); (9) expose all of the SU-8 sidewalls, as shown in Figure 5.6 (C); (10) post-bake samples at  $110^\circ\text{C}$  for 20 minutes, then cool down to  $60^\circ\text{C}$  in 1 hour and remain at  $60^\circ\text{C}$  for 5 hours, then cool down to room temperature in 3 hours; (11) development in SU-8 developer for 2 hours, rinse with IPA and DI water, dry in air; (12) bond cover glass, seal inlet and outlet tubes. The SEM images of a prototype microfabricated hydrofocusing unit (without covering glass) are shown in Figure 5.7.

The total dimensions of this hydrofocusing unit are about 10mm long, and 8mm wide. The inlet for sheath flow and center inlet for sample flow of the fabricated hydrofocusing unit are 1mm wide. Sample injection nozzles with several different sizes ( $100\mu\text{m}$ ,  $200\mu\text{m}$ , and  $150\mu\text{m}$ ) were tried on a single wafer. The outlet channels of different widths ( $100\mu\text{m}$ ,  $300\mu\text{m}$ ,  $500\mu\text{m}$  and  $1000\mu\text{m}$ ) and the same depth of  $500\mu\text{m}$  were also made for comparison purpose. The outlet channel of the prototype unit as presented in this chapter is 1 mm wide and  $500\mu\text{m}$  deep; the diagonal width of the sample injection nozzle is  $150\text{ }\mu\text{m}$ .

### **5.3 Experiments and Discussions**

The experimental setup is schematically shown in Figure 5.8. Three BD plastic syringes were seated on a syringe pump. For testing purpose, the sample flow was injected using a 1cc



BD plastic syringes. Sheath flow was pumped in with two 20cc BD plastic syringes. Two tests were conducted. In the first experiment, a fluorescent dye (Aldrich Chemical Company, Inc. Catalog # F245-6) solution with 1.2 mMol/L concentration was used as the sample flow and DI water was used as the sheath fluid. This experiment was used to check the hydrofocusing capability of the prototype. The second experiment was conducted to check the functionality of the prototype in sorting microscopic objects such as red blood cells. In the second test, diluted, labeled, tanned sheep erythrocytes (red blood cells) were used as the samples and a saline solution was used as the sheath flow.

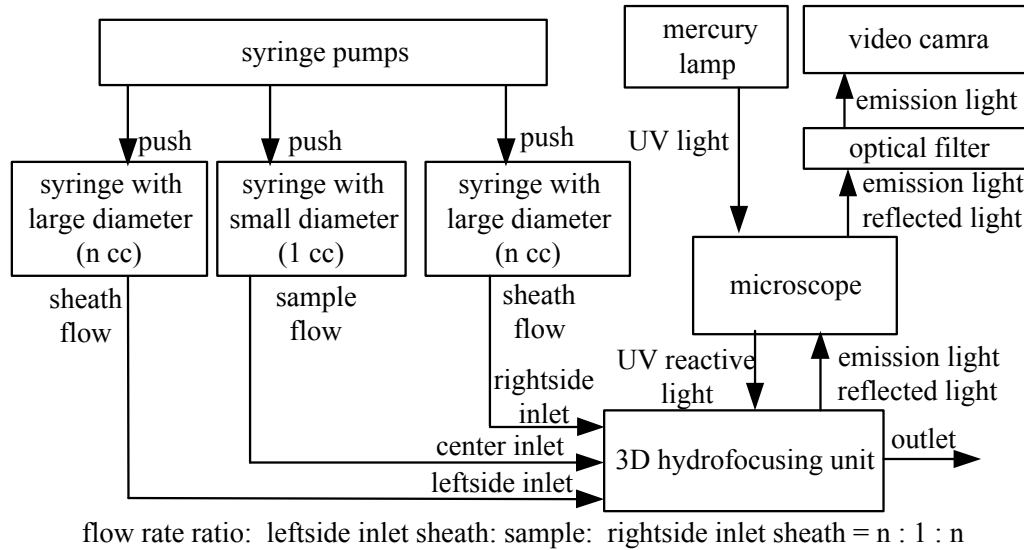


Figure 5.8. Experiment setup

The three syringes used were of the same length and different cross-sectional areas. The cross-section of 20cc BD syringes is 20 times that of the 1cc syringe. A syringe pump (Harvard Apparatus' PicoPlus) was used to drive all three syringes at the same speed. The flow rates of the left-side sheath fluid, the right-side sheath fluid, and the sample fluid at the center were therefore in the ratios of 20:20:1. A change of syringe diameters (syringe volume) would change the sheath-sample ratio. Sample solution and sheath flow were pumped through the inlets into the

hydrofocusing unit. The three-dimensional laminar sheath flow hydro-focused the sample flow into the core stream of the outlet micro-channel. A mercury lamp was used to provide illumination through the microscope onto the outlet microchannel. The emission light and the reflected light from the outlet microchannel were filtered using an optical filter, which permitted mainly the emission light to pass through. The images of focusing flow were magnified with a microscope. A Nikon CV-252 digital video camera was used to monitor the hydrofocusing process. This standard NTSC video camera collects 30 frames (actually 29.97) per second, and two fields per frame.

In the first experiment (using a fluorescent dye), the dye solution was pumped from the center inlet through the injector nozzle into the hydro-focusing chamber, and DI water (sheath flow) was pumped from the right and left inlets into the hydro-focusing chamber. The three-dimensional hydro-focusing effect can be measured by inspection of the gray scale distribution in the photo images of the CCD video camera. Single frames were selected from the hydrofocusing video by Adobe Premiere Pro software [Adobe Systems Incorporated, San Jose, CA]. In the pictures of the hydro-focusing chamber, the regions with high concentration of fluorescent dye (sample flow) are brighter than that without fluorescent dye and thus (sheath flow) would be dark. The hydro-focusing function in the horizontal direction was shown in Figure 5.9 (A). The video camera and microscope used in the experiments has very limited depth of focus (DOF). The bright images of the center core stream would disappear when the video camera and microscope were adjusted up or down away from the position to take the pictures as in Figure 5.9 (A). This means the flow with high concentration of fluorescent dye was only in one level. Figure 5.9 (B) shows the side-view image of hydro-focusing function in the vertical direction as the sheath flow and the sample enter the hydrofocusing chamber. The dash lines in Figure 5.9 (B) show the boundary of the hydro-focusing chamber and the outlet channels. From

Figure 5.9 (A) and (B), it shows that the sample flow was focused in both the vertical direction and the horizontal direction.

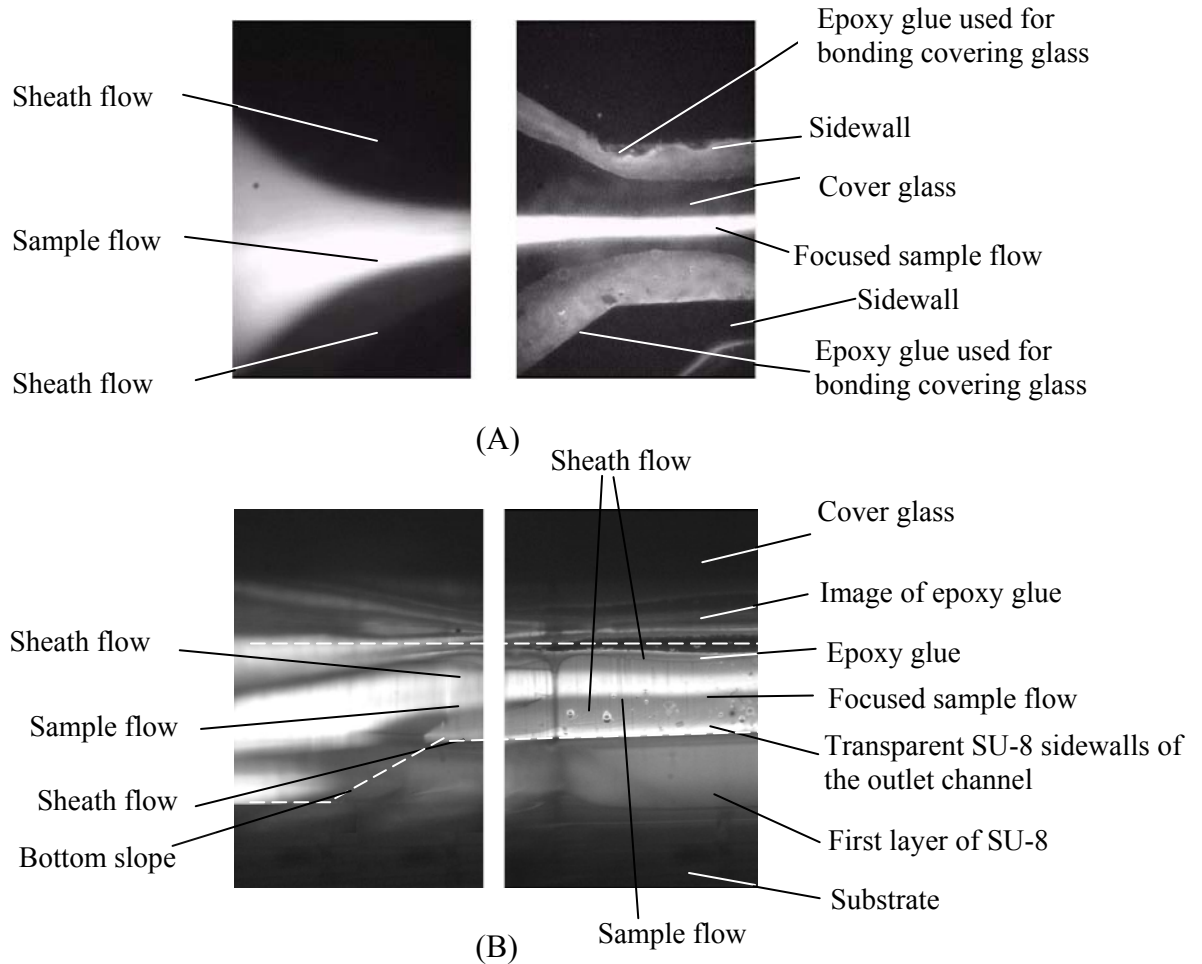


Figure 5.9, Images of fluoresce dye solution was focused (x4). (A) Top view image showing the hydrofocusing function in horizontal plane; (B) Side-view image showing the vertical focusing function.

In the second test, diluted liquid of labeled tanned sheep erythrocytes (red blood cells) was used as sample fluid and the saline water was used as the sheath fluid. A single frame picture was selected from the video of hydrofocusing labeled erythrocytes by Adobe Premiere Pro software as shown in Figure 5.10. It shows an image of the labeled tanned sheep erythrocytes (red blood cells) as they were focused and sorted in the chamber of the three-dimensional hydrofocusing unit. From the photograph in Figure 5.10, it can be seen that cells were lined up along

the central line in the photograph. Because this standard NTSC video camera is only capable of catching 30 frames of images (actually 29.97) per second, the image quality dramatically reduced when a single frame is taken out from the movie video. The movement of these cells was clearly visible in the video. However, only blur images of these high-speed moving cells could be seen in the picture.

The erythrocytes (red blood cells) used in the test are microscopic biconcave disks with a diameter approximately 6-10  $\mu\text{m}$ . When these cells were hydro-dynamically focused in the chamber of the prototype unit, any slight differences in flow velocity across the stream may pull the cells to rotate around and be aligned with the direction of the stream. Eventually, all the cells were pulled to orient their long axis along the stream to achieve dynamic balance. The shear stresses in the flow also cause cells to be elongated along their long axes. Based on video of hydrofocusing labeled erythrocytes, all sample cells were animatedly oriented, deformed, and focused by the hydrodynamics force.

The experimental results presented have proved the feasibility to utilize 3-D lithography technology to fabricate the device with cured SU-8 polymer as the structural material. The sample flow was very effectively focused and cells were neatly lined up along the axial line of the central stream. Further improvement can be made by replacing the flat cover with a similarly designed top part (no sample inject nozzle required) as the bottom piece. The fluid stream can then be focused equally in both vertical and horizontal directions. This hydrofocusing unit can be integrated with other micro flow and micro optical systems to be incorporated into a micro-sized blood cell categorizing and counting system for use during space flight and in other remote point-of-care applications including military field operations. Because the focus of the research

work presented in this dissertation is on the aspect of the design and microfabrication, no further discussion on the micro-fluid dynamics will not be provided.



Figure 5.10, Cell sorting images of hydro-focusing unit. The image was a frame taken out from the video taken with NTSC CCD camera (x4), the bright dots are images of labeled tanned sheep erythrocytes.

## **CHAPTER 6. OUT-OF-PLANE, FREE-SPACE, PREALIGNED REFRACTIVE MICRO-OPTIC COMPONENTS BASED ON UV LITHOGRAPHY OF SU-8**

### **6.1 Out-of-Plane Micro-optic Components and the Advantages in Integrated Optical Systems**

Integrated free-space optical benches have wide applications in military, telecommunication, metrology, biochemistry, etc. For integrated free-space optical benches, the optical components, such as microlens, cylindrical lens, beam splitter, prism, reflective mirror, light sources, etc, are needed.

Microlens is a very important component in the integrated microoptical system and microlens arrays are widely used in optical systems and devices. There are many methods to fabricate microlens and microlens arrays including: (1) surface tension at re-flow temperature of the polymer [88, 89]; (2) isotropic wet-etching [90]; (3) ink-jet ultraviolet (UV) curable epoxies or photoresist [91]; (4) hot-embossing to imprint micrlens or microlens arrays in PMMA (Polymethylmethacrylate) or similar materials [92]; and (5) molding UV curable epoxies or photoresists with rigid or elastomeric molds [93].

The microlenses or microlens array fabricated with the conventional methods are normally in the same plane as the substrate because it is based on regular lithography process and surface technologies. However, integrated optical systems often require the lenses' principal plane to be perpendicular to the substrate on which the system is constructed. One approach to obtain such out-of-plane microlenses is to use a flexible hinge [94-96]. Microlens arrays suspended on a mechanical hinge are fabricated using surface technologies and then driven up to the vertical position either electrostatically or electromagnetically [94-97]. Microstereolithography is another technology used to fabricate microlenses [98, 99]. It makes high-aspect-ratio, three-

dimensional microstructures by sequentially adding thin layers of polymer lithographically based on a numerically sliced two-dimensional mathematical model. The basic principle of fabricating microstructures layer by layer and the inherently serial process obviously limits the surface quality, material homogeneity, and production rate.

Fabrication of micro-optical components and devices using x-ray lithograph of PMMA offers very high quality but carries much higher expenses [100-102]. As an economical alternative, UV-lithograph of SU-8 (a negative tone photoresist from MicroChem Inc., Newton, MA) has been widely used in Micro Electromechanical Systems (MEMS) and Micro Optoelectromechanical systems (MOEMS) in recent years [1, 2, 10, 14-18, 26, 29, 37, 38, 41, 42, 45-48, 50, 78, 103-113]. Cured SU-8 polymer has very good mechanical properties, relatively high thermal stability (glass transition temperature  $> 200^{\circ}\text{C}$ ), high chemical stability, and very good optical properties. It was used as structural material for many MEMS applications. There were some prior efforts to utilize the advantages of the optical properties of cured SU-8 by using it as a structural material to fabricate planar wave-guides [104, 114, 115], gratings [116], prisms and other optical components. Fabrication of optical components with planar or cylindrical surfaces is relatively easy in lithography-based processes while it is extremely difficult to obtain spherical or aspherical surfaces with optical axis parallel to the substrate. The research work presented in this chapter uses a novel 3-D fabrication method to obtain the spherical/aspherical surface for out-of-plane pre-aligned polymer microlens or microlens array. The technology uses a multiple UV-lithography of SU-8 and carefully controlled development process. Alignment and assembly are commonly used in conventional optical systems and affect their performances significantly. For some high precision optical instrument, such alignment and assembly are often done manually, therefore increasing the cost and limiting the achievable precision. This out-of-plane polymer microlens or microlens array can be easily pre-aligned with

other optical components with no additional adjustment and assembly required, and therefore dramatically reduce the running cost and improve the quality and performance of the optical system.

Other optical components, such as prism, cylindrical lens, plano-plate, can also be fabricated by directly UV lithography of SU-8 similar to the technology used for the microlens, as shown in Figure 6.1. When the mask for the optical bench incorporating such microlens and microlens array is designed, all the optical components are pre-aligned in mask design. No changes and adjustment between the mask and the photoresist on the substrate are needed during lithography. The precision of the pre-assembled system is therefore limited by that of the optical mask used. Without any assembly and alignment, this microlens' optical axis is parallel to the substrate on which the whole optical system may be built. This unique advantage makes it possible to design and fabricate free-space, pre-aligned integrated optical bench for a wide variety of applications without any assembly and alignment. It helps to reduce the running cost, save time, and improve the quality and performance of the integrated optical systems.

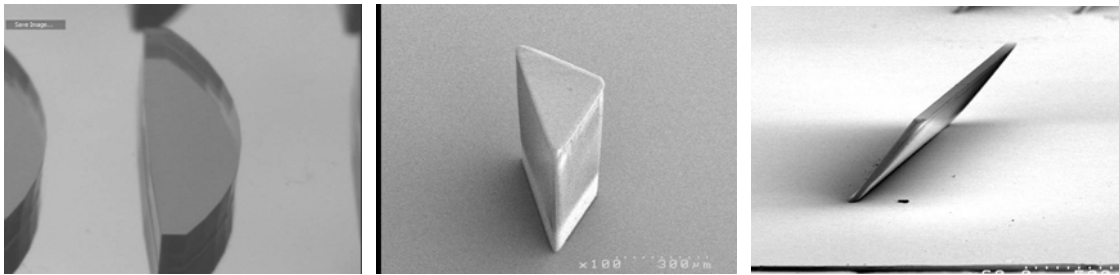


Figure 6.1 Cylindrical lenses, prism, and a reflective mirror with 45° angle with the substrate

In the following sections, the design, simulation, 3-D UV lithography fabrication, test and analysis for the out-of-plane pre-aligned polymer refractive microlens and microlens array will be presented [26-28, 30, 31]. This out-of-plane polymer microlens is designed and optimized through simulation, and then successfully microfabricated using a unique UV lithography

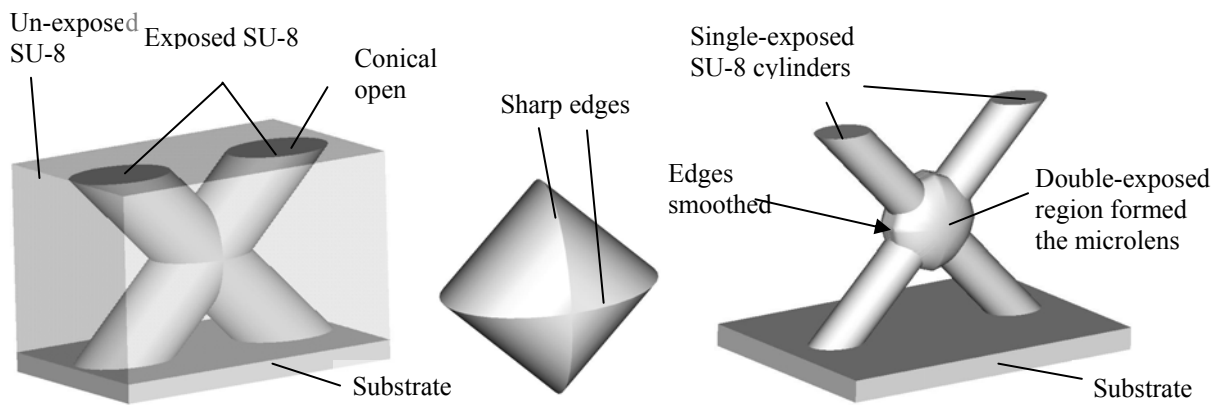


technology. In this fabrication technology, the desired surface profile is obtained by a controlled SU-8 development after two tilted exposures. The microlens' backside focal length, diameter of focal pad and surface curve were measured, analyzed, and compared with the simulation results.

## **6.2 Principle of the Out-of-Plane Microlens and Microlens Array Fabricated Using Direct Lithography**

The basic fabrication principle for the out-of-plane, pre-aligned polymer refractive micro lenses can be best explained using the schematic diagrams shown in Figure 6.2. To obtain a cylindrical light beam in a tilted exposure of SU-8 at 45°, the opening in the photomask must be a conic curve. The conic curves associated with various values of the conic constant, such as ellipse, circle, parabola, and hyperbola, can be used for the mask pattern of the out-of-plane microlens or microlens array, depending on the requirements for the microlens' surface profile. Here ellipse is used to explain the principle to fabricate the out-of-plane microlens or microlens array. For an incident light with 45 degrees tilt, the ellipse's semi-major should be  $\sqrt{2}$  times length of the semi-minor. When two light cylindrical beams in perpendicular are projected on SU-8 resist, the intersected region of the resist is double-exposed. Because SU-8 is a negative resist, two perpendicular cylindrical structures are formed, each with a 45 degree angle with respect to the substrate. If each beam used has only half of normal exposure dosage for SU-8, only the intersection will have double exposure dosage and forms the shape as shown in Figure 6.2 (B). This faceted surface includes four pieces of cylindrical surfaces. The intersection region forms two perpendicular sharp edge lines. Both of the single exposure regions and double exposure regions have less dosage to fully cured the SU-8 resist, so both of these two regions can be developed with different etch ratio, but much lower than the un-exposed SU-8. In the development, the un-exposed SU-8 is developed with a much faster ratio than exposed but un-fully-cross-linking SU-8. The exposure dosage needs to be optimized based on the experiments.

During the development process, the development solution tends to work in our advantage and helps to reduce sharp edge between the two regions. Because the single and double exposed regions are developed with different ratio, the intersection area is the base of the microlens. By careful control of the exposure dosage and the optimized development time, the transitional area between the region of “single-exposed area” and the “double-exposed area” become much smoother than schematic diagram shown in Figure 6.2(B). The final result that can be expected in a practical lithography process is a quasi-parabolic shape with smooth surface profile as shown in Figure 6.2(C). The fabrication principle of microlens array is shown in Figure 6.3. In the UV lithography both of microlens and microlens array, *h*-line dominated broadband UV light are used. The spectrum of the light source is shown in Figure 2.6 (marked as “light intensity after PMMA”)



(A) Before development. (B) The intersection region is double-exposed and formed the lens base. (C) After development, the sharp edges were rounded and smoother surface profile is obtained.

Figure 6.2, (A) Two cylindrical light beams intersect in 90 degrees. (B) The double exposed area has a faceted surface consisting of four pieces of cylindrical surfaces. (C) Possible surface profile of quasi-parabolic microlens after lithography and development processing.

The central region of the microlens represents the paraxial area for the lens and is the working area for most of the applications. When collimated light beam enters the central area

along the optical axis, the light can be focused. The major plane of the microlens obtained by this way is perpendicular to the substrate.

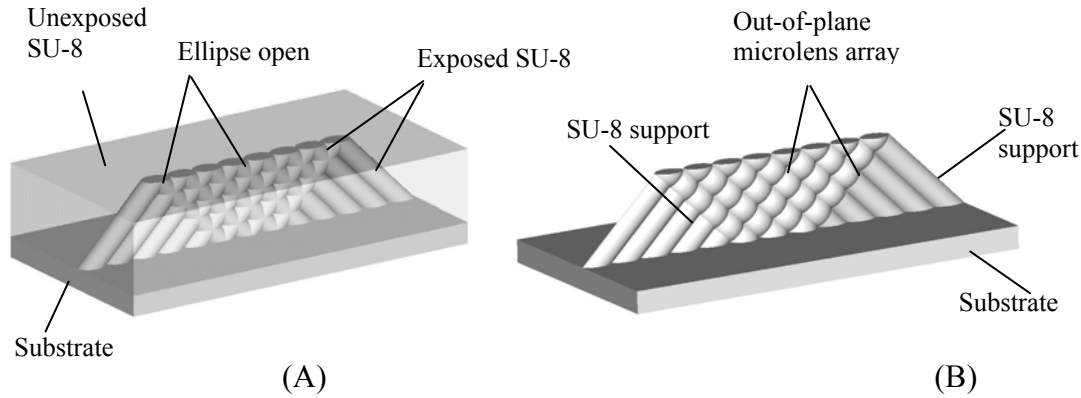


Figure 6.3, Fabrication principle of the microlens array

### 6.3 Simulation for the Surface Formation of the Out-of-plane Microlens

Numerical simulation is an indispensable tool in the development process of micro optical system, which provides us better insight in the functions and performances. In addition, it may also help to optimize the design before the fabrication process and therefore substantially reduces costs and turnaround times.

The surface profile control of the out-of-plane microlens is very important research work for control the focal length, diameter of the focal pad, and the repeatability for the surface profile. So physically understanding the procession for the surface formation is very important for the surface profile control. A simple mathematics modeling will be given first.

During development process, it is well known that not only the un-exposed SU-8 is removed. The exposed regions may also been dissolved though at much lower rate. Because half dosage was used in the lithograph process, only the intersection region is double-exposed as shown in Figure 6.4. During the development process, the half-exposed region obviously is dissolved at much higher rate than that for the fully exposed region. Because the unexposed SU-

8 is normally developed many times faster than the exposed SU-8, it can be assumed that the development of the unexposed SU-8 will not affect the development of the exposed SU-8 for being neglected in numerical simulation.

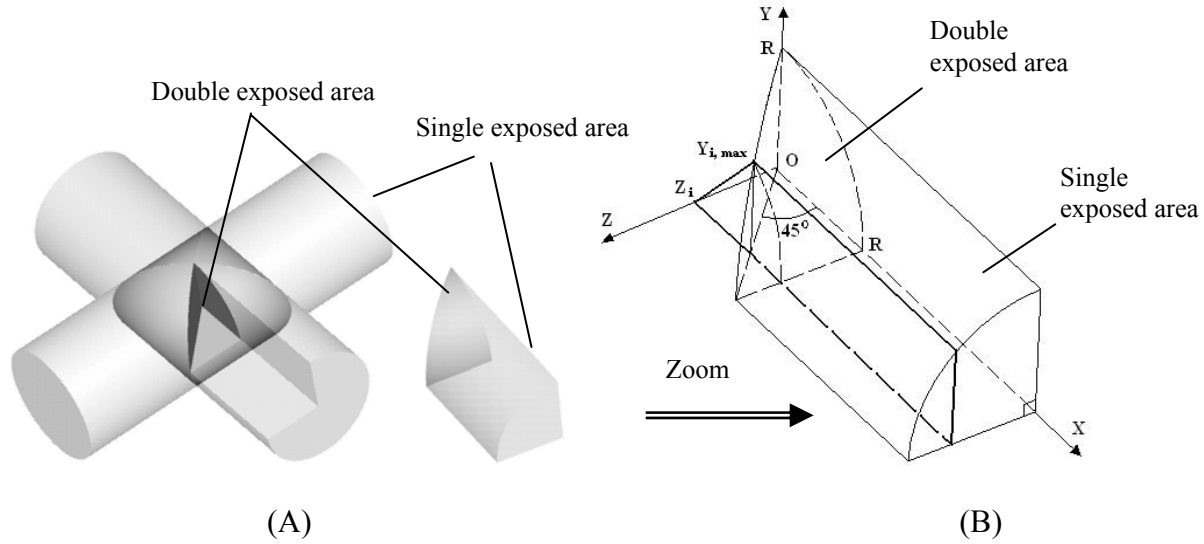


Figure 6.4, (A) Because of the symmetry of the exposed region formed by two perpendicularly intersected beams, one eighth of the structure needs to be studied. (B) Schematic diagram showing the interested region and the Cartesian coordinate system.

From the experimental results for the prototype samples fabricated, the development rate of the SU-8 in the double-exposed region of the microlens is measured to be about 50%~80% (0.5~0.8 times) of that for the single exposed area depending on the specific dosage used. For the regions around the intersection, the single-exposed layers cover the double-exposed section. In the development process, as soon as the single-exposed part is developed, development solution starts to attack the double-exposed part. After a given development time period, the final surface profile obtained is the combined effects of development of both the single-exposed and double-exposed regions at different rate and thickness.

To better understand the fabrication process and the effects of different exposure dosages and development times on the surface profiles of the microlenses, a simple numerical simulation

was conducted. This study is very important for further improvement of the microlenses and to provide guidelines for the fabrication of the microlenses.

The basic principle of the simulation can be best explained by the schematic diagrams shown in Figure 6.4 and Figure 6.5. Because of symmetry as shown in Figure 6.4(A), only one sixteenth of the intersection region needs to be studied in numerical simulation as shown in Figure 6.4(B). A Cartesian coordinate system is assigned as shown in Figure 6.5 with the origin located at the cross-point of the two axes of two beams. The schematic diagram of Figure 6.5(A) is the projected view of the intersected region along the positive X-axis of Figure 6.4(B) while the diagram shown in Figure 6.5(B) is the side view along the Z axis direction.

Two major assumptions were made in simulation: 1) developing rates of both the single- and the double- exposed SU-8 resists do not change during development; and 2) both the single-exposed and double-exposed SU-8 surfaces will be developed uniformly along the radial direction of exposed cylindrical surfaces. From Figure 6.4, it can be seen that double-exposed region in most part is covered by single-exposed resist layer. The thickness of the covering SU-8 layer changes from zero at the vertex point of the lens to the maximum thickness at the edge. During development, the single-exposed-layer in the intersection region needs to be developed before the double-exposed region is attacked by the developing solution. According to the two assumptions made previously, the developing rate is constant along the radial direction as viewed from x-axis direction in Figure 6.4(B). As the single-exposed region is developed, more and more double-exposed region starts to be developed (first at the vertex point). The development rate is much lower, and is assumed to be constant in the radial direction as viewed from the z-axis in Figure 6.4(B). The final surface profile of the microlens is the combined result of developments of both the single- and double- exposed resists at different rates.

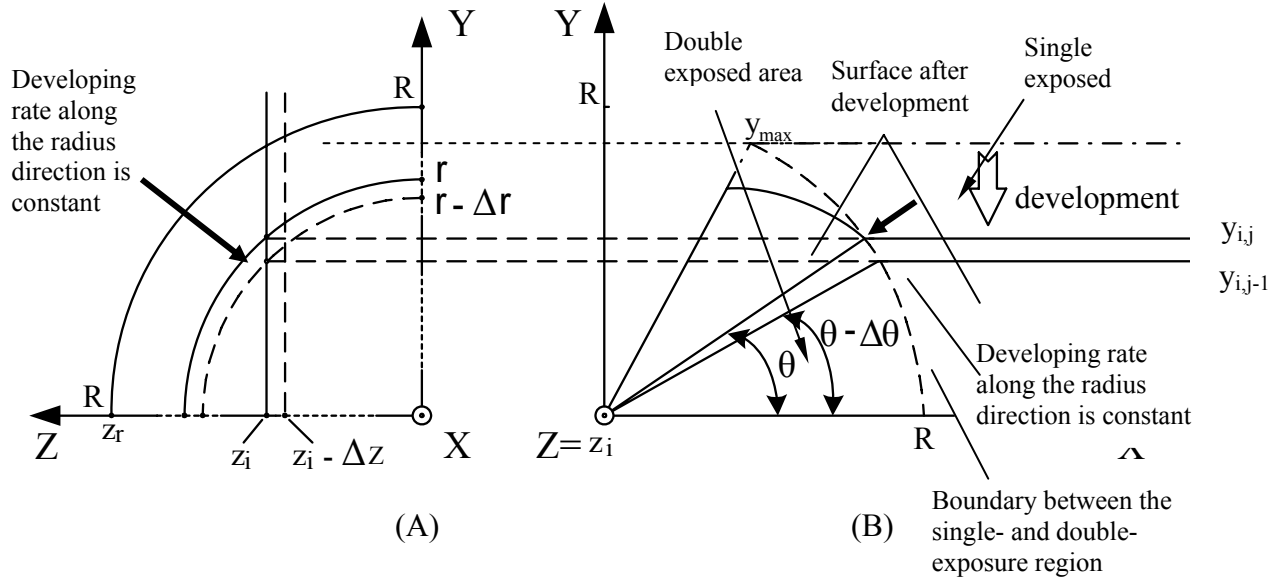


Figure 6.5, Integrate the development effect on the surface

Figure 6.5(A) shows the projected view as observed from the positive x-axis direction of Figure 6.4(B) during the development. Figure 6.5(B) shows the cross-sectional area marked in Figure 6.4(B) viewed from the positive z-axis direction. In Figure 6.5, the radius of the lithography beam is  $R$ . Along  $Z$  direction,  $R$  is numerically sliced into many sub-sections:  $Z_r, Z_{r-1}, \dots, Z_i, \dots, Z_2, Z_1, Z_0$ . When the single exposed SU-8 is dissolved from radius  $r$  to  $r - \Delta r$ , assume a vertical plane numerically sliced the model at  $z = z_i$ , the cross-section formed as shown in Figure 6.6(B) can be further divided into a series sub-domains with  $y$  positions at:  $y_{i,r}, y_{i,r-1}, \dots, y_{i,j}, \dots, y_{i,2}, y_{i,1}, y_{i,0}$ . As the angular position changes from  $\theta$  to  $\theta - \Delta\theta$ , the vertical coordinate changes from  $y_{i,j}$  to  $y_{i,j-1}$ . As the double-exposed region gradually exposed to the developing solution, these sub-domains will dissolve along the radial direction of the dashed curve as shown in Figure 6.5(B). The flowchart of numerical simulation algorithm is presented in Figure 6.6.

A program following the flowchart in Figure 6.6 was developed to carry out the calculations. A grid of position points was calculated numerically by slicing the model in  $z$

direction and along angular direction. The data points obtained as the model was numerically sliced along z-axis are shown graphically in Figure 6.7(A). After obtaining the coordinate positions for all of the interested points ( $z[i]$ ,  $x[i][j]$ ,  $y[i][j]$ ), a commercial software, Pro/E (PTC Inc., Needham, MA), was used to connect the coordinates of the points to obtain the surface profile as shown in Figure 6.5(B) for the simulated one sixteenth of the microlens. Finally the simulated surface profile for the entire microlens is obtained using the geometrical symmetry as in shown in Figure 6.7(C). In the simulation presented in Figure 6.7, the ratio of the development rates between the single exposed area and the double exposed regions are assumed to be 1:0.55.

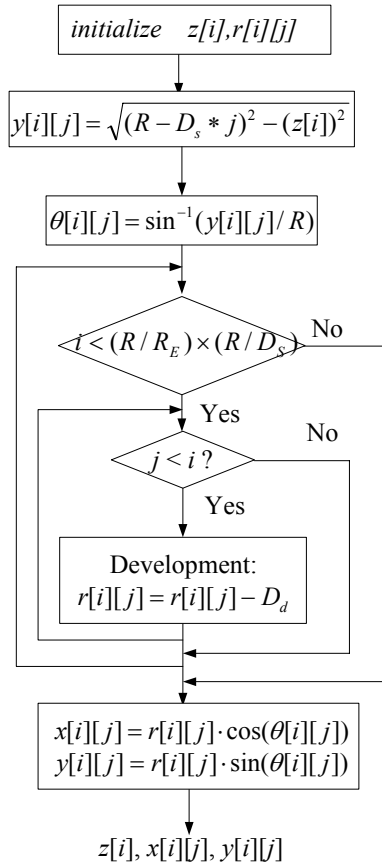


Figure 6.6. The flowchart of the simulation algorithm, in which  $D_s$  stands for the development rate of the single exposed area, the  $D_d$  stands for the development rate of the double exposed area, the  $R_E$  stands for the radius of the single exposed SU-8 cylinder at the end of the development.

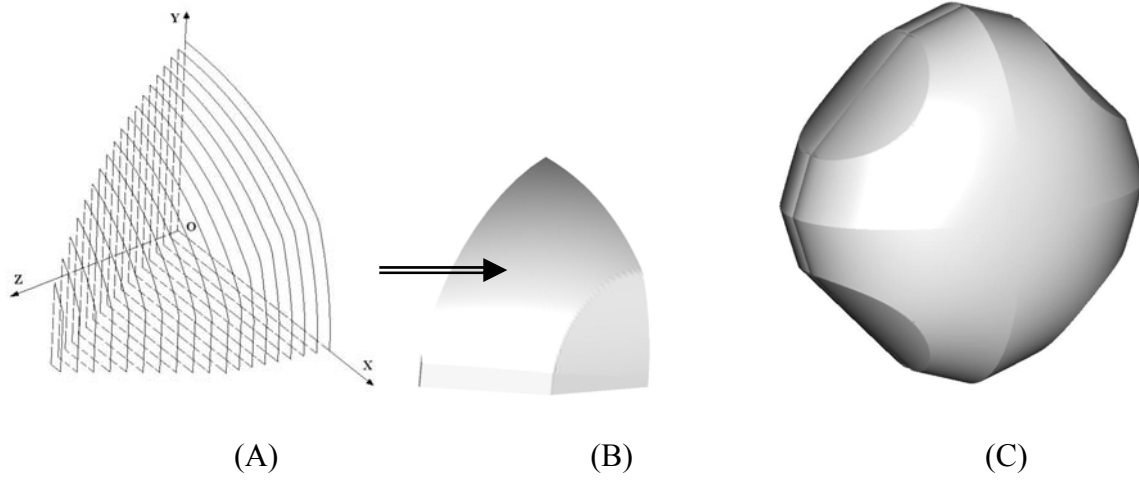


Figure 6.7. The simulated surface with assuming the development rate ratio between the single exposed area and the double exposed area is 1:0.55. (A) The simulated curves on the double exposed surface. (B) 1/16 blended surface based on the simulation curves in (A). (C) View of the microlens from a random angle.

From the simulated results shown in Figure 6.7(B) and (C), slight edge lines between each of the sections of the microlens can still be observed. In practical situation, these lines will be much smoother than they are shown here. The main reason is that uniform development rate was assumed in radial direction. However, dissolution of a solid surface is a process strongly related to volume, sharp corners are always dissolved faster than a planar surface. In real SU-8 development, the sharp edges along the  $45^\circ$  dividing lines between the X or Z coordinates are smoothed by the SU-8 developer.

The curve shown in Figure 6.8 is the simulated surface profile at  $Z=0$  cross-section when the radius of the single-exposed cylinders is developed to 50% of the original size. The polynomial trend line with  $R^2 = 1$  for the dot line curve in Figure 6.10 for  $Z=0$  is as equation (6.1):

$$y = -2 \times 10^{-11} x^6 + 4 \times 10^{-9} x^5 - 4 \times 10^{-7} x^4 + 2 \times 10^{-6} x^3 - 0.0016 x^2 + 0.0005 x + 71.95. \quad (6.1)$$

Neglecting the higher order terms, a parabolic curve is obtained as equation (6.2):



$$y = -0.0016x^2 + 0.0005x + 71.95, \quad (6.2)$$

where the constant term is the y-axis offset.

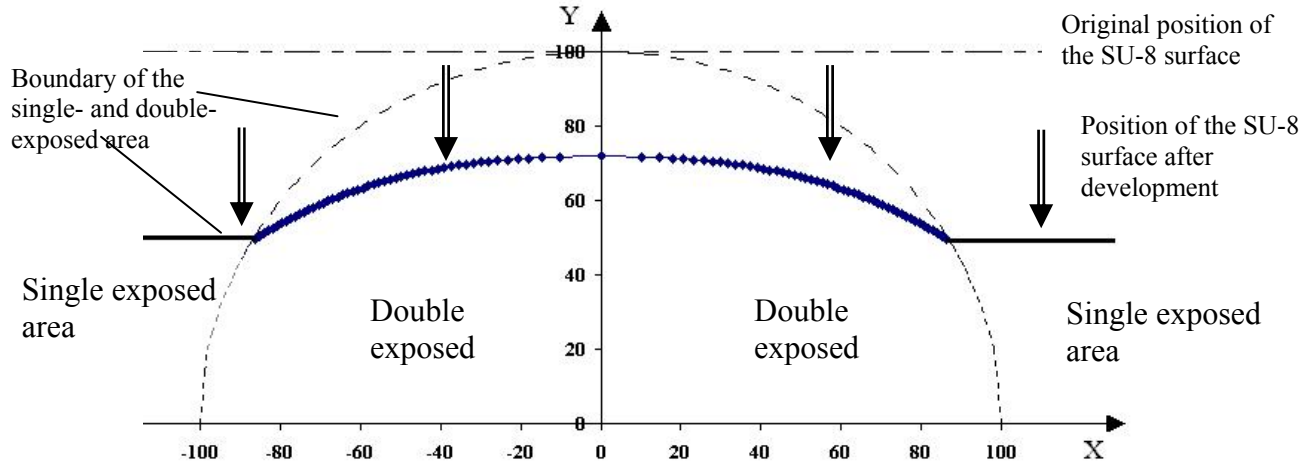


Figure 6.8, the simulated surface profile at the  $z=0$  cross-section when the single-exposed cylinder is developed to about 50% of its original size.

The diameters of the prototype microlenses fabricated in this study range from  $100\mu\text{m}$  to  $1000\mu\text{m}$ . In this range, the optical diffraction can be neglected in the simulation for visible light source. There are many kinds of modern optical design software available for simulating the free-space optical systems. In our study, a commercial named ZEMAX (ZEMAX Development Corporation, San Diego, CA) was used.

Figure 2.1(B) in Chapter 2 shows the transmission spectra of 1.108mm thick cured SU-8 film measured in our laboratory with Ocean Optics' S2000 spectrometer. From Figure 2.1(B) it can be seen that the transmission coefficient of the cured SU-8 is very high within a quite broad range of wavelength. This range covers the whole spectrum from near UV to infrared. Figure 2.1(D) is the refractive index of the cured SU-8 film measured Synowicki in J.A. Woollam Co., Inc. with M-2000 spectroscopic ellipsometer.

The surface profile as shown in Figure 6.7(C) was used in numerical simulation with ZEMAX EE. The quasi-parabolic surface profile of the microlens was converted into a data file with Pro/E \*.igs format and then imported into the ZEMAX\OBJECTS directory. The simulations were conducted in Non-Sequential Model of ZEMAX EE.

Because cured SU-8 is not a standard optical material and not listed in ZEMAX's catalog, a new glass catalog was defined specifically for cured SU-8 by entering the transmission data and the refractive index data as shown Figure 2.1(B) and Figure 2.1(D). A database with 100 points for the transmission and refractive index values between 301.34~670.27nm were entered. Only visible light (F, d and C lines with wavelength 486.13nm, 587.56nm, 656.27nm respectively) was used in simulation and the primary wavelength is d line.

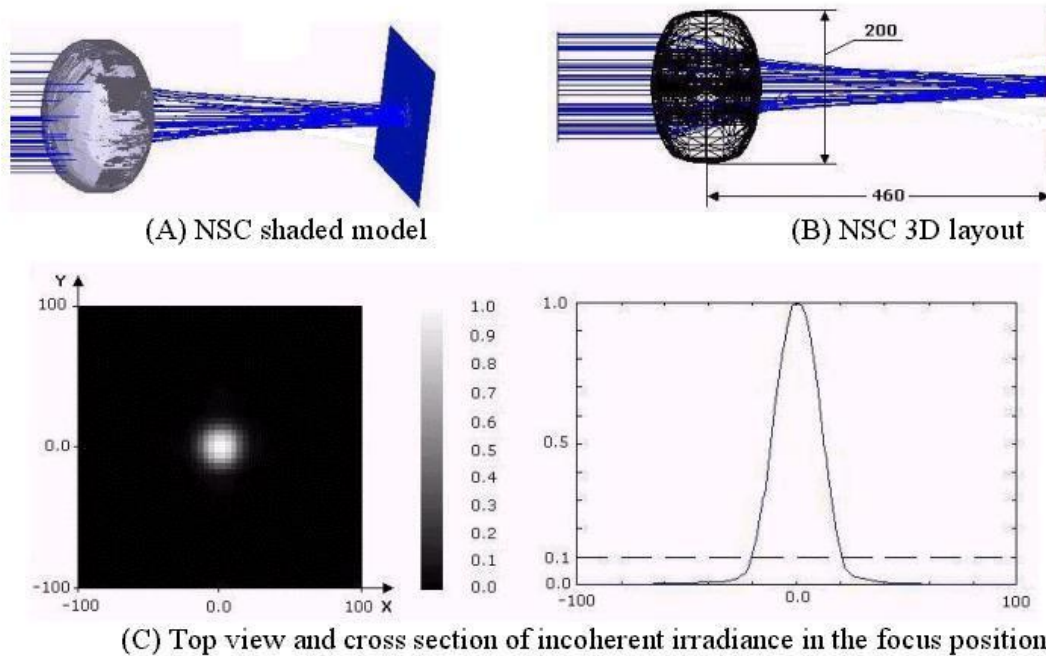


Figure 6.9, Light trace for the developed curved SU-8 structure shown as Figure 6.7(C)

To obtain a general solution, dimensionless numbers were used in the simulation. The diameter of the lithography beam used to fabricate the microlens was assumed to be 200 units. Figure 6.9 shows the simulation results for the lens surface profile as shown in Figure 6.7 (C). A

square collimated light source of 160 units by 160 units is projected to the quasi-parabolic lens along the optical axis. The display screen (detector viewer) used has a dimension of 200 units by 200 units. By moving the detector screen along the optical axis, the focus position was found to be 460 units away from the surface of the microlens, as shown in Figure 6.9(B). By tracing the rays, the energy distribution at the focal position is obtained on a screen as shown in Figure 6.9(C). With the focal pad defined as the area within which the light intensity falls to 10% of the maximum light intensity, the diameter of the focal pad is calculate to be about 40 units, 20% of the diameter of the lithography beam.

The surface profile control is an important work for the out-of-plane microlens and microlens array. The relationship between the surface profile and the lithography condition is very complex. But in our research, we find the surface profile can be controlled by the pattern shape on the lithography mask if same lithography conditions, such as expose dosage, development condition, pre-baking and post-baking condition, etc., are maintained.

The numerical model built in section 6.3 is a very simple one because several assumptions were made for the simulations as stated earlier: 1) developing rates of both the single- and the double- exposed SU-8 resists do not change during development; 2) both the single-exposed and double-exposed SU-8 surfaces will be developed uniformly along the radial direction of exposed cylindrical surfaces. In fact, the development rate not only depends on the cross-linking state of the resist, it also depends on the geometry of the surface under study. Sharp corners tend to be developed in a much higher rate than the flat regions. The development direction is along the normal direction of the local spot under consideration, which is not necessarily always in the radial direction of the exposed cylindrical surface. Further study needs

to be conducted to better understand and simulate the surface forming and profile control mechanisms using the dosage and development rate control techniques.

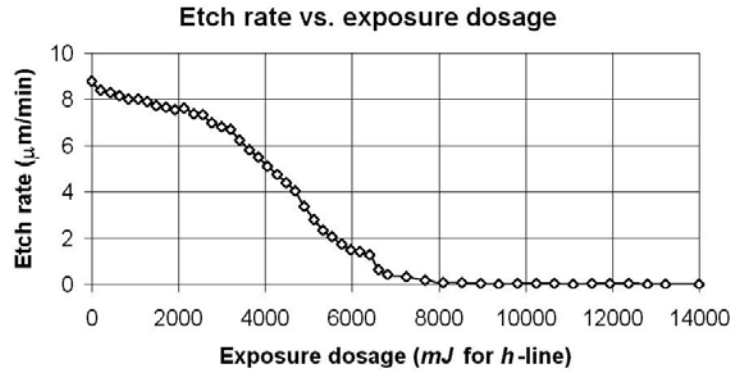


Figure 6.10 Development rate vs. exposure dosage for SU-8 with *h*-line exposure

To be able to control the surface profile of the out-of-plane microlens and microlens array is very important to improve the quality of the integrated free-space optical benches. The commercial lithography simulation software, such as Solid-E (from Sigma-C, German), etc, may need to be used to conduct the three-dimensional surface profile simulation for the tilted lithography using two intersected beams. This simulation is essential to finding the relationship between the mask pattern shape and out-of-plane surface profile under particular pre-bake, exposure, post-bake, and development conditions. The SU-8 development rate under particular experiment conditions needs to be measured, as shown in Figure 6.10, in addition to other lithography properties of SU-8, such as, transmission-wavelength curve, photo-chemical reaction and post-bake properties, etc. These parameters are the key data required in using the commercial lithography simulation tools to study the sidewall profile of the out-of-plane microlens.

## 6.4 Microfabrication Process and Results

The non-conventional mask and substrate exposure method are shown schematically in Figure 6.2. A clutch is used to hold the mask and the substrate. The clutch is designed in such a way so that it may permit a rotation angle of 90 degrees. As shown graphically in Figure 6.2, when two cylindrical light beams in perpendicular to each other are projected on the photo-resist, the intersection forms the base of the microlens or pixel of microlens array.

Two tilted exposures, inclined at  $45^\circ$  with respect to the substrate and perpendicular to each other to obtain a 90 degrees intersection, are required for lens fabrication. The inclined exposure principle is shown in Section 2.5 of Chapter 2, and the exposure setup was as shown in Figure 2.16. If a cylindrical beam is needed in the resist, the opening in the photomask needs to be an ellipse curve, the mask opening shape must be the ellipse cross-section area formed when the designed beam is cut in a 45 degrees tilt to the axis of the beam. For an incident light with 45 degree tilted, the ellipse's long axis length should be  $\sqrt{2}$  times of the short axis length.

The transmission of a 1mm thick un-exposed SU-8 100 is measured as shown in Figure 2.1(B) in Chapter 2. The absorption coefficient of unexposed SU-8, as shown in Figure 2.1(A), at the *h*-line ( $\lambda = 405$  nm) is about 1/4 that at the *i*-line ( $\lambda = 365$  nm), and 3 times that at the *g*-line ( $\lambda = 436$  nm). The light components of shorter wavelengths are primarily absorbed in the surface region while the longer wavelength components penetrate further down and expose the bottom region. It is therefore desirable to filter out the wavelengths shorter than 365 nm to improve the uniformity of the microlens' surface profile or uniformity of microlens array's pixels, and avoid over-exposure in the surface layer. Longer wavelengths (either *g*-line or *h*-line) with much lower absorbance were used to permit more energy to reach the bottom part of the thick SU-8 resist layer and to achieve much better uniformity of the absorbance. In our lithography, a 4.538 mm

thick PMMA sheet was used as a filter and an Oriel UV station was used for the lithography. The transmission of this PMMA sheet is about 0.3% at the *i*-line, 82% at the *h*-line, and 82% at the *g*-line as shown in Figure 2.6 in Chapter 2. The light intensities before and after the PMMA filter and the transmission of the PMMA filter are also shown in Figure 2.6 in Chapter 2. Because the absorbance at the *h*-line is about three times that of the *g*-line, the *h*-line is regarded as the primary lithography light.

The thickness of the SU-8 to be spin-coated is determined by several factors, including the size of the lenses and the desired height of the lenses at which the light beam is going to be coupled to. In the applications that may require multiple parallel light beams to be coupled and focused, microlens array is needed. Then the total thickness of the resist to be coated needs to be equal to the sum of the lens' height, the additional height adjustment for coupling purposes, as well as the space required for multiple light beams.

In fabrication process for the prototype out-of-microlens, SU-8 100 resist is spin-coated with 400 rpm, pre-baked at 110°C for 13 hours, followed by 8 hours cooling period. The sample was then exposed with 2J/cm<sup>2</sup> dosage with *h*-line dominated UV broadband light for each + and – 45 degree tilted exposure, then post-baked at 110°C for 30min and followed by another 8 hours cooling period. The exposure dosage used in the lithography process was carefully controlled to improve the surface profile and uniformity of microlens array's each pixel. Finally the sample was developed with SU-8 developer for 2 hours at 20°C, rinsed with fresh SU-8 developer, IPA and DI water and dried naturally. The double-exposed regions of resist formed the out-of-plane, pre-aligned (at desired position) refractive polymer microlens or microlens array, the sizes of the single exposed regions are slightly reduced, and the unexposed regions were completely removed in development. Scanning electron microscope (SEM) images of a typical set of out-of-

plane pre-aligned refractive polymer microlens and microlens array are shown in Figure 6.11 and Figure 6.12. By comparing with Figure 6.1(C) and Figure 6.2(B), it can be observed that the intersected regions formed out-of-plane microlens and pixels of the out-of-plane microlens array in Figure 6.11 and Figure 6.12 respectively.

Multiple exposures were used to overcome the over-exposure, diffusion, and scattering problems at the surface of the resist. The exposure dosage used in the lithography process can be carefully controlled to improve the surface profile of the faceted lens. After exposure and development, the surface profile of the faceted lens may become much closer to a perfect spherical/aspherical lens.

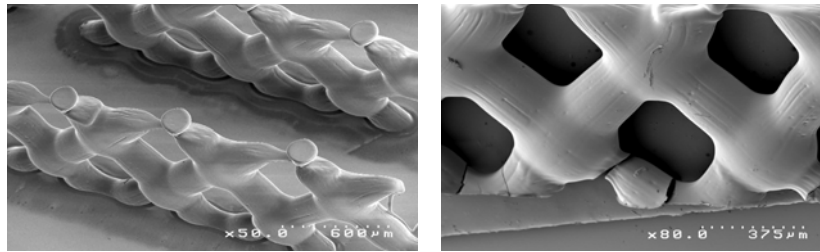


Figure 6.11 SEM pictures of the out-of-plane microlens with 250 $\mu$ m diameter lithography beam (A) out-of-plane microlens on Si substrate (B) microlens is removed from the substrate for measurement purpose.

To inspect the lens quality, individual lens was taken off the substrate and tested. The experiments show that 90 degree cross was achieved as expected after the prism was used to correct the refraction.

The microlens' focus length, DOF, and minimum focal pad are measured. A measurement diagram is shown as in Figure 6.13. The microlenses with the inclined SU-8 supporting post are carefully cut down with a sharp knife along the surface of the substrate, and put onto the glass. A collimation light goes through the glass on a precision stage and is projected on the backside of the lens. A high-resolution microscope is used to magnify the

image, and a CCD camera is used to take the image. By adjusting the stage, the diameter of the lens and the diameter of the focus pad can be measured. The focus length is also measured by using the translation stage, microscope, and CCD camera as shown schematically in Figure 6.13.

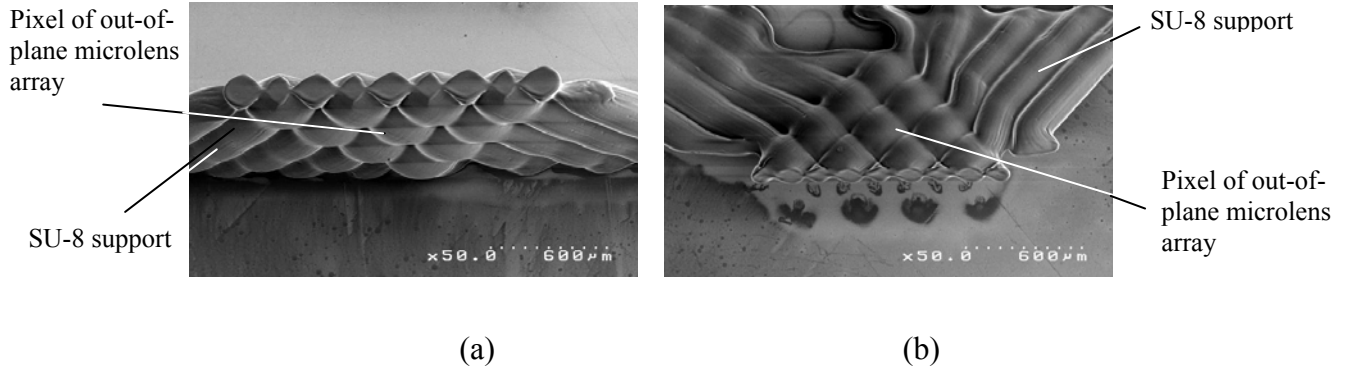


Figure 6.12 SEM pictures of the out-of-plane microlens array (a) Microlens array perpendicularly adhered on the substrate (b) Microlens array is mechanically removed from the substrate to measure the surface profile

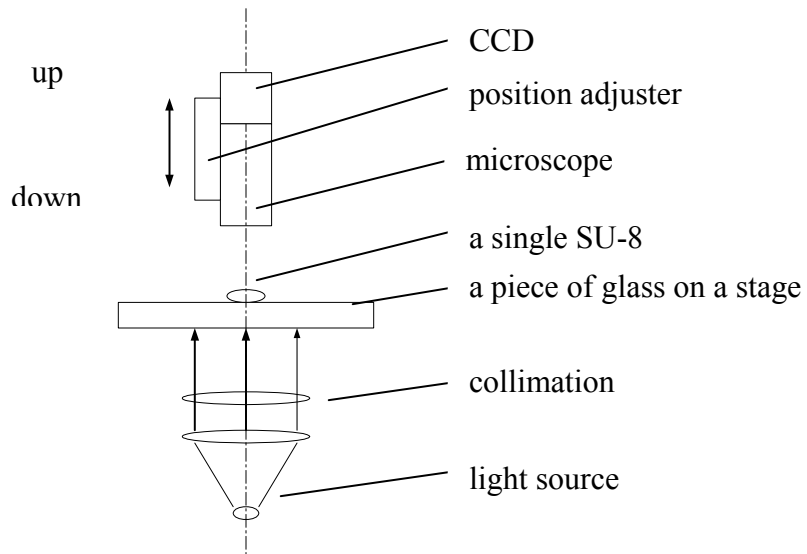


Figure 6.13 Schematic diagram for the measurement set

Figure 6.14 (A) shows close-in photo picture of one of the lenses. Figure 6.14 (B) shows a micro lens' minimum focal pad as shown in Figure 6.14(A). The microlens is linked with polymer microposts. These microposts were resulted from the fabrication process. The height of the posts can be controlled by the thickness of the resist and the mask design. This may also



provide the flexibility to integrate the lens in an optical measurement system. From Figure 6.14 (B), it can also be seen that the SU-8 supporting posts over the lenses does not affect the optical performance of the out-of-plane SU-8 microlens with collimation light. Because these SU-8 supporting posts over the lenses can guide light, if the incident angle on the out-of-plane microlens is not proper, the light will be guided through the supporting post as well as through the lens. This will set the limit for the angle of incidence. The backside of the microlens' quasi-spherical area will be regarded as the aperture of the microlens.

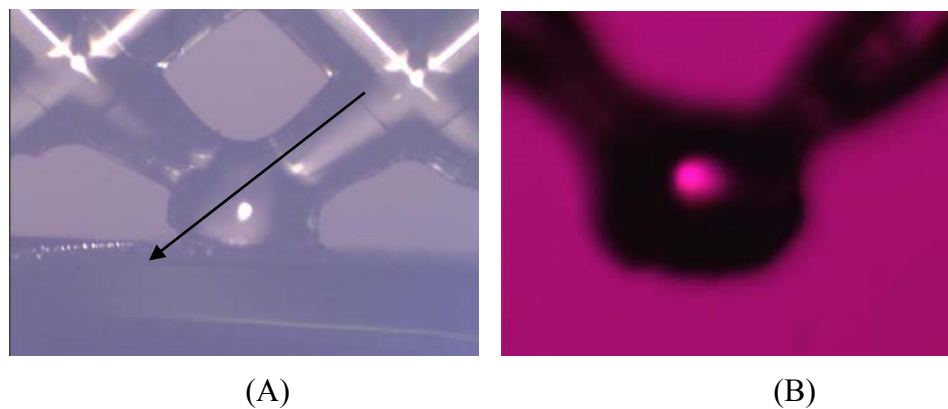


Figure 6.14. (A) An optical picture of the prototype out-of-plane quasi-ball lens tested. The arrow line in the picture shows the scanning direction of the surface profiler as shown in Figure 6.15; (B) The lens shown in (A) was mechanically taken off the substrate and tested with collimated red light.

The diameter of light beams used in the lithography process for this particular lens was 250 micrometers. The microlens was measured to have a focus length of 250-300 micrometers for both sides of the lenses, with the minimum focus pad of 26.3 micrometers. The depths of the focus (DOF) for both sides of the lenses are measured as around 10 micrometers. The lens medium can be regarded as homogeneous because of the same material with the same exposure dosage in a small area. Because of the limitation of the available equipment and the micro-sizes of the prototype microlens, the optical aberration was not measured at this stage and needs to be done as part of the future study.

Because of their small dimensions (smaller than or compatible with the interferometer's working beam) and elastic structure, the surface profile of the prototype lens cannot be measured directly using the conventional measurement methods, such as optical surface profiler (white light interferometer) or mechanical surface profiler. The surface profile of this polymer quasi-ball lens is measured using a Tencor Alpha-Step 500 surface profiler. The prototype lens as shown in Figure 6.14(A) was broken off the substrate and was scanned along the direction of the lithography beam as shown by the arrow line in Figure 6.14(A). The measurement result is shown in Figure 6.15. Based on the measurement data, the radius of the lens surface is 431.51 micrometers, which is different from the radius of the lithography beam, 250 micrometers. The main reason for this difference is the development process. It is believed that short development time contributed to increase radius of curvature. However, if the development time is too long, the developer tends to attack the lens surface and lower the surface quality significantly.

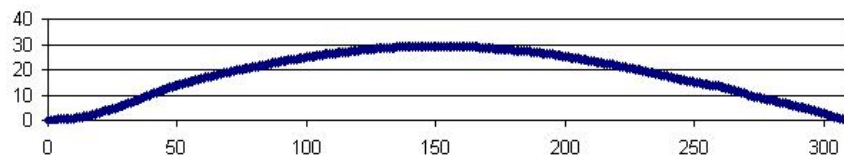


Figure 6.14. Surface profile of the SU-8 microlens (units: micrometers).

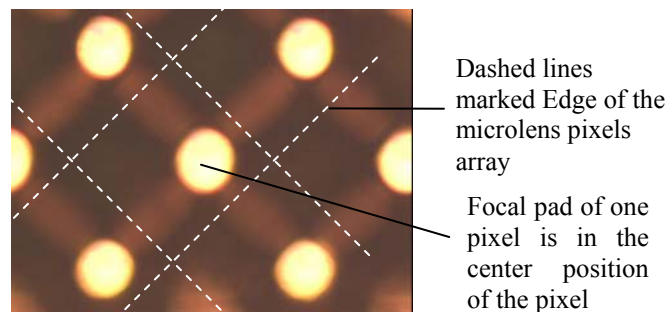


Figure 6.15, Microlens array's focal pads (the marked dot line stands for the edges of pixels)

Figure 6.15 shows the focal pads images of the microlens array. As shown in Figure 6.15, the focal pads for pixels of the microlens array are uniform. The boundaries for the square-shape

pixels of the microlens array are marked with dash lines. It can be seen that the measured focal pads are located in the centers of corresponding pixels. By manually adjusting the stage, the diameter of the lens, the size of the focus pad, and the backside focal length were measured and the average measurement results are shown in Table 6.1.

Table 6.1. Average measurement results for the out-of-plane polymer microlens array

Lithography beam diameter ( $\mu\text{m}$ )	150	200	250	300	350
Size of each pixel (square size) ( $\mu\text{m}$ )	150 x 150	200 x 200	250 x 250	300 x 300	350 x 350
Measured focal length (f) ( $\mu\text{m}$ )	110.3	191.0	249.0	276.4	388.0
Measured focal pad (d) ( $\mu\text{m}$ )	32.1	35.9	62.5	74.0	107.7
Measured depth of Focus (DOF) ( $\mu\text{m}$ )	46.2	55.1	54.7	47.2	41.7
$\text{NA} = n \cdot \sin \alpha$	0.693	0.595	0.579	0.609	0.638

The fill-factor of a microlens array is defined as the percentage of lens area to the total area, which is affected by the pixel geometry and lens layout. Except for a few technical literature [90] related to microlens array fabrication that discuss the square geometrical lens array with 100% fill-factor, most of the reported work discuss only circular geometrical lenses arrays. The fill-factor for a circular microlens pixel in an orthogonal lens array is at a maximum of  $\pi/4$ , in a hexagonally arranged array it is the maximum at about  $\sqrt{3}\pi/6$ . Both of these microlens array configurations have a smaller fill-factor number in comparison with this out-of-plane square microlens array presented herein. Each pixel's shape in the SU-8 microlens array is equivalent to a spherical surface cut and fitted into a square frame (the aperture of the microlens). This geometry can help to achieve a fill-factor of almost 100% and permits very high energy transmission efficiency.

For different fabrication runs, the shape, dimension, pixel uniformity and optical properties would not change when the same lithography (such as, pre-bake, expose dosage, wavelengths selection, post-bake, etc.) and development condition are maintained. Different expose dosage and development time may result in variations of the surface curvature and the focal length for each pixel of the microlens array.

The microlenses fabricated using direct UV lithography can be used for basic focus function and digital optics, such as optical relay. For some applications that may require a truly three-dimensional arrangement for focus of multiple light beams, this technology may offer unique advantages. With pre-aligned optical components in the mask design, it is possible to have all components integrated onto a single platform for an optical bench without assembly. Optimal selection of wavelengths and dosage in lithography may help compensate the absorbance difference (determined by the cross-linking difference) across the resist with the development rate from top to bottom layers and help to achieve uniformity of the surface profiles among all elements in the entire array. More work still needs to be done to optimize the relationship among the wavelength selection, exposure dosage and the development.

The successful fabrication of out-of-plane microlenses is very important to development of integrated free-space optical devices and systems. Other basic components such as mirrors, beam splitters, and the gratings may also be fabricated using the same thick resist lithography process. The fabrication presented here also makes it possible to have all components integrated on a single platform in a truly 3-D design. Other optical devices and systems such as tunable optical filter, Fabry-Parot interferometer, micro image system, and metrology such as position and displacement detection systems may also be developed. The technology may also lead to

competitive free-space optical measurement systems to the widely used optical waveguide principle for biological and bio-chemical sensing devices.

## **CHAPTER 7. MICROFABRICATION OF OPTIC FIBER BUNDLE COUPLER WITH INTEGRATED FOCUSING LENSES USING UV LITHOGRAPHY OF SU-8**

### **7.1 Limitations of the Conventional Technologies and the Advantages of Integrated Fiber Coupler Fabricated Using Direct Lithography of SU-8**

Optical fiber is widely used in telecommunication and optical sensors. Fiber coupler is a very important component for the optical communication system and fiber optical-based sensors. It is commonly used to manipulate light signal and to complete the connection of light-source-to-fiber, fiber-to-fiber, and fiber-to-detector to relay the optical propagation for illumination delivery or signal collection. By reducing back-reflection and alignment errors, fiber couplers can increase light throughput. The alignment of the optical components in most optical fiber applications is extremely critical for ensuring the maximum amount of light that flows through the coupled devices. Fiber coupling is subject to three types of misalignments: separation (longitudinal misalignment,  $z$  axis), offset (lateral misalignment,  $x$  axis), and tilt (angular misalignment,  $\theta$ ). In longitudinal misalignment, the end of the fibers may not be in the optimized position; if the end of the second optical fiber is positioned away from the image position of the end of the first fiber, light from one fiber core will spread and lose much of its intensity when coupled into the receiving fiber. In the case of offset error, the fiber cores may be displaced laterally along the direction perpendicular with the optical axis, light emitting from one core hits the cladding layer of the second fiber may also result in reduced light throughput. In the third case, one fiber may be tilted (rotated around the  $x$ - and  $z$ -axis) relative to the other and cause a signal transmission loss.

In a conventional fiber coupler with optical lenses and fibers, light from the source (such as, laser, diode, lamp, etc.) or the end of another fiber is focused by one or two optical lenses and

coupled into another fiber or a detector. In a conventional fiber coupler, a mechanical fiberport collimator is used to precisely adjust the position of the fiber with respect to the lens to obtain the maximum coupling efficiency. The fiberport collimator needs to be adjustable in several axes, normally  $x$ ,  $y$ ,  $z$  and  $\theta$ . The conventional types of mechanical fiberport collimators have a large size and are not easy to be integrated with other optical components. In conventional optical fiber systems, such alignment and assembly are often done manually, therefore increasing the complexity of operation. Additionally, the cost and the limit of achievable precision in these mechanical fiberports are determined by the complexity of the optical system (i.e., number of couplers and physical dimensions of the fiber) and the operator expertise, respectively.

Microfabrication of fiberport and coupling systems is an attractive approach for simplifying the optical system, which incorporate fiber optics. For example, silicon micromachined V-groove fiber couplers [117, 118] are attractive and simple devices that can be used to obtain precise alignment of optical fibers, and also can be directly integrated with other optical components. By etching a series of V-grooves on the silicon substrate, high precision coupling of many fibers to other optical devices can be achieved.

There are many methods to fabricate microlenses or microlens arrays and apply them in optical fiber systems. The most commonly used method is to fabricate a spherical tip on the optical fiber to enhance the coupling efficiency to a receiving fiber or other optical component. These ball lenses are fabricated by melting the optical fiber's end to form a lens, which is based on surface tension principles [119]. Micro-jet technology can also be used to place a lenslet at the end of a multimode fiber to improve coupling efficiency [120]. Ball lenses formed by thermal re-flowing of two polymer layers has been shown to be assembled into a silicon-based platform for fiber coupling [121, 122].

In this chapter, an approach using 3-D UV-lithography of SU-8 photoresist [24, 25] is presented for fabricating pre-aligned fiber bundle couplers. This fiber bundle coupler includes a pre-aligned out-of-plane refractive microlens array [26-28, 30, 31] and fiberport collimator arrays. With the optical axis of each pixel parallel to the substrate, each pixel of the out-of-plane microlens array can be pre-aligned with the corresponding pixels of the fiberport collimator arrays in the mask design. The microlens array and fiberport collimator arrays are made using photolithography so that precise alignment can be obtained without accumulation of tolerances. As a simple example of a pre-aligned integrated optical system [28], an out-of-plane polymer microlens array was pre-aligned to fiber collimator arrays in the mask design. In each pixel of the fiber bundle coupler, lateral misalignment and angular misalignment are minimized by this pre-alignment technology. The longitudinal misalignment also can be minimized by the stop function of the fiber-fixing groove in the coupler. As a result, no additional adjustment or assembly was required, leading to dramatically reduced running cost and significantly improved alignment quality and coupling efficiency. This technology for a fiber bundle coupler can also be used to fabricate pre-aligned fiber couplers for just single fiber-to-fiber junctions as well.

In the following sections, the design and working principles for the pre-aligned fiber coupler will be presented first, followed by the detailed fabrication process used to make the fiber bundle coupler. Finally, experimental results for the pre-aligned fiber bundle couplers fabricated with this principle are presented and discussed [29].

## **7.2 Design of the Fiber Bundle Coupler and Tilted Lithography of SU-8**

The research work presented in this chapter uses a 3-D fabrication method to obtain the pre-aligned fiberport collimator array and out-of-plane polymer microlens array. This technology is based on multiple-step UV-lithography of SU-8 and carefully controlled development process



for both the fiberport collimator array and the microlens array. Each pixel of this out-of-plane polymer microlens array is pre-aligned with the corresponding pixels of the fiberport collimator with no additional adjustment and assembly requirement.

When the mask for the optical fiber bundle coupler is designed, the fiberport and the microlens are pre-aligned to the designed position. No changes and adjustment between the mask and the photoresist on the substrate are needed during the lithography process. The precision of the pre-assembled fiber bundle coupler is therefore limited by the optical mask used. Without any assembly and alignment, the optical axis of the microlens is parallel to the substrate on which the whole optical system is built. This unique advantage makes it possible to design and fabricate pre-aligned fiber bundle couplers with precise alignment and high coupling efficiency.

The fabrication and working principle for the fiber bundle coupler are shown in Figure 7.1. Because SU-8 is a negative tone photoresist, the exposed regions remain after lithography and development. The entire fiber bundle coupler is designed on a single photomask. Two exposures at  $\pm 45^\circ$  tilt angles with respect to the surface normal are conducted for the out-of-plane microlens array fabrication. When two cylindrical light beams in perpendicular are projected on the SU-8 resist, two perpendicular cylindrical structures are formed at a  $45^\circ$  angle with respect to the substrate and the intersected region of the resist is double-exposed. This faceted surface of the intersected region includes four pieces of cylindrical surfaces. The lithography light used is an h-line ( $\lambda = 405 \text{ nm}$ ) dominated UV light source with optimized dosage and wavelength selection ratio. The position between the substrate and the mask are fixed during and after the exposure for the microlens and microlens array. With a defined region of the microlens or microlens array covered using a shade mask, the fiberport collimator array is then

fabricated lithographically using an i-line ( $\lambda = 365$  nm) dominated broadband UV light source in an optimized exposure dosage and wavelength selection ratio.

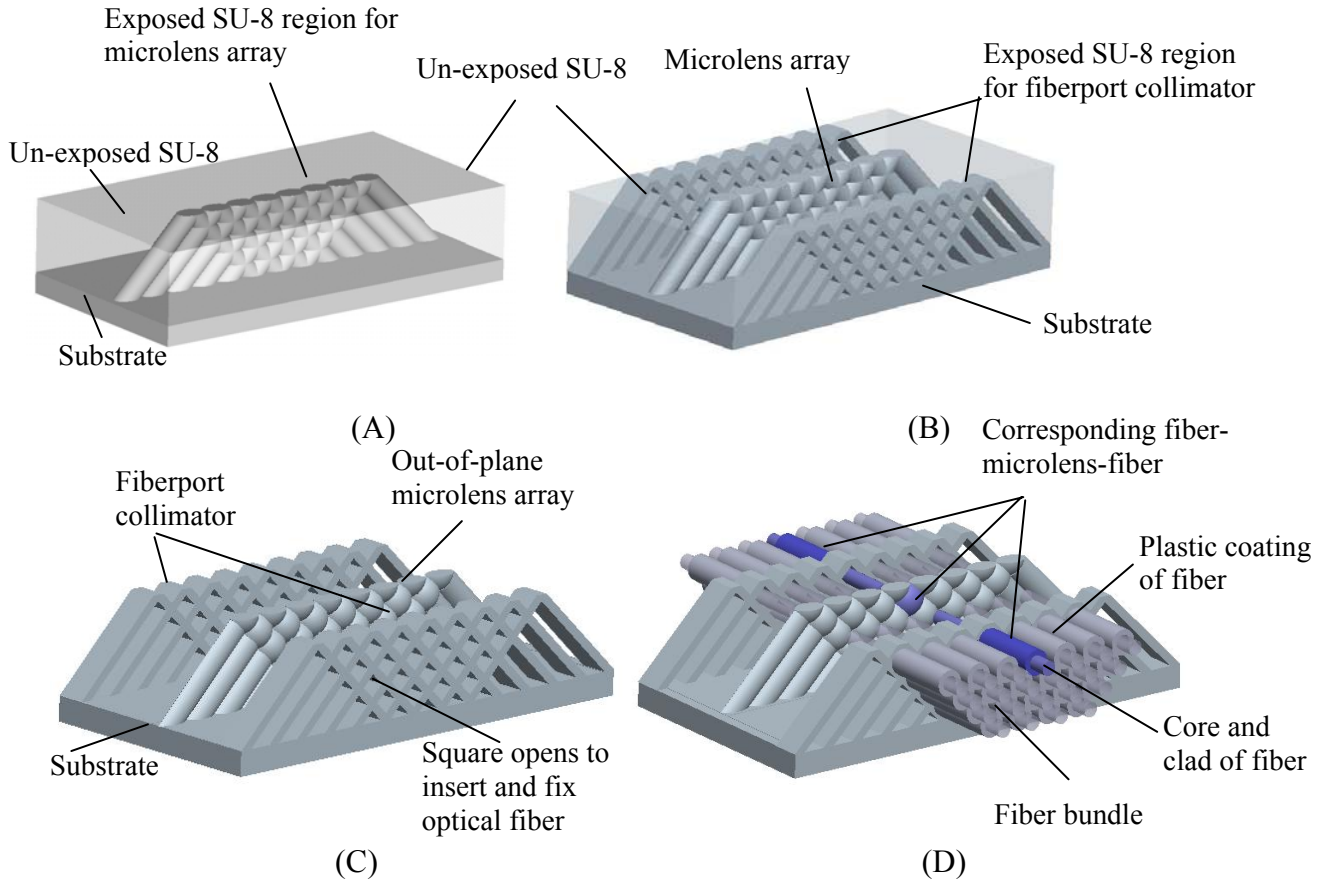


Figure 7.1, Fiber bundle couplers. (A)  $\pm 45^\circ$  tilted expose for the out-of-plane microlens array region. (B) Covering the microlens array region by a shade mask with a  $\pm 45^\circ$  tilted expose for the fiberport collimator region with the same mask. (C) After development, each pixel of the microlens array and corresponding pixel of the fiberport collimator array are precisely aligned. (D) Diagram showing the position of the fibers after inserting the fiber bundle, in which the corresponding fiber-microlens-fiber system is marked in blue for clear definition of the optical path.

The development rates for the unexposed SU-8 and exposed SU-8 with different exposure dosages are different. By careful control of the exposure dosages, wavelength selection, and the optimized development time, the intersection regions are developed into the out-of-plane microlens and microlens array [26-28, 30, 31]. The rectangle posts tilted at  $\pm 45^\circ$  formed the fiberport collimator. The final shape of this fiber bundle coupler after development is

schematically shown in Figure 7.1(C). In a practical lithography process, each pixel of this convex microlens array can be expected to have a quasi-spherical shape with a smooth surface profile and its optical axis is overlapped with the central line of the square opening for the corresponding fiberport collimator. Each pixel of the out-of-plane microlens can be aligned with the corresponding pixel of the fiberport collimator as schematically shown in Figure 7.1(D). One single optical mask used therefore determines the pre-alignment precision of the whole fiber coupler.

To obtain a cylindrical light beam in a tilted exposure of SU-8 at  $\pm 45^\circ$  for the out-of-plane microlens and microlens array fabrication, the opening in the photomask must be of a conic shape. The conic curves associated with various values of the conic constant can be used for the mask pattern of the out-of-plane microlens or microlens array, depending on the requirements for the microlens' surface profile. The ellipse, circle, parabola, and hyperbola can be used for the mask pattern for the out-of-plane microlens or microlens array to achieve the corresponding surface profiles. The bigger curvature along the optical axis in the mask pattern will have microlens with bigger curvature along the optical axis. The detail relationship between the final microlens surface profile and the designed mask pattern will be researched in the future work and will not be discussed here. After stripping the plastic coating layers, the diameter of the center glass fiber (include core and clad) used here is  $125\text{ }\mu\text{m}$ . Because of the  $45^\circ$  tilted lithography, the distance between the two open blocks for the fiberport collimator, as shown in Figure 7.2, is  $125\sqrt{2}\text{ }\mu\text{m}$  to obtain a square opening with dimensions of  $125\text{ }\mu\text{m}$  by  $125\text{ }\mu\text{m}$  to fix the optical fiber. If the fiber's diameter of the core and clad changes, corresponding changes in the designed dimensions of the fiberport collimators need to be made. For easy development of the square channels for the fiberport collimators, the long square holes are separated by

several cascaded pieces as shown in Figure 7.2. In order to insert the optical fibers into the fiberport collimators easily, an opening larger than the optical fibers' outside diameter can be designed as shown in Figure 7.2.

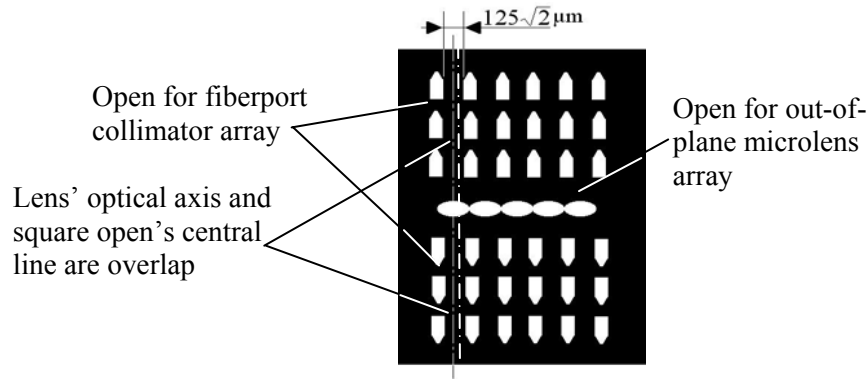


Figure 7.2, Mask patterns for the fiber bundle coupler

### 7.3 Fabrication of Prototype Fiber Bundle Couplers

#### 7.3.1 Wavelength Selection and Refraction Compensation in Tilted Lithography

The lithography light used for the out-of-plane microlens and microlens array fabrication is an *h*-line ( $\lambda = 405\text{nm}$ ) dominated broadband UV light with optimized dosage and wavelength selections light (in Figure 2.16, marked as “Light intensity after PMMA filter”). The transmission of a 1 mm thick unexposed SU-8 100 is measured as shown in Figure 2.1(B). The components of shorter wavelengths are primarily absorbed in the surface region while the longer wavelength components penetrate further down into the resist and expose the bottom region. The absorption coefficient of unexposed SU-8 for the *h*-line ( $\lambda = 405\text{ nm}$ ) is about one fourth that of the *i*-line ( $\lambda = 365\text{ nm}$ ), and 3 times that of the *g*-line ( $\lambda = 436\text{ nm}$ ). In order to improve the exposure uniformity for the entire area of the microlens array, wavelengths shorter than 365 nm need to be filtered to avoid over-exposure of the surface layer. Longer wavelengths (either *g*-line or *h*-line) with much lower absorbances are used to permit more energy to reach the bottom part

of the thick SU-8 resist layer and to achieve better uniformity of the absorbance. In our experiment, a 4.54 mm thick PMMA sheet was used as a filter and an Oriel UV station was used for the lithography. The transmission of this PMMA sheet is about 0.3% at the *i*-line, 82% at the *h*-line, and 82% at the *g*-line. The light intensities of the Oriel UV station with 200 W output before and after the PMMA filter and the transmission of the PMMA filter are also shown in Figure 2.6.

Because the absorbance at the *h*-line is about three times that of the *g*-line, the lithography process for the out-of-plane microlens and microlens array region is *h*-line dominated. During the development process, not only the unexposed SU-8 is removed, the exposed regions may also be dissolved during development, although at a much lower rate. The development rate for the un-exposed SU-8, single-exposed SU-8, and double-exposed SU-8 also occur at different rates. During the development process, the single-exposed region is dissolved at a much higher rate than that of the double-exposed region. The unexposed SU-8 is normally developed many times faster than the exposed SU-8. Our previously reported work [26-28, 30, 31] proved that these intersection areas form microlenses with quasi-spherical surface profiles. In addition to the mask pattern geometry, surface profiles of the microlenses are also affected by exposure dosage, wavelength selection, development conditions, and bake conditions.

The light source used for the lithographic fabrication of the fiberport collimator array is the *i*-line ( $\lambda = 365$  nm) dominated broadband UV light (in Figure 2.6, marked as “Light intensity of light source”). Full exposure dosage was used for the fabrication of the fiberport collimators to make sure the bottom part of the device receives sufficient exposure dosage and is fully cured. The dissolving rate of these sections of the exposed SU-8 in the development process is

negligible and the shape of the fiberport collimator array can therefore be assumed to depend only on the geometry of the mask pattern.

The refraction of the light at the surface of the SU-8 resist is dependent on the wavelengths of the light source. For the *h*-line light ( $\lambda = 405$  nm), the refractive index,  $n$ , is 1.650, the critical angle is  $37.305^\circ$ . For the *i*-line light ( $\lambda = 365$  nm) with  $n = 1.660$ , the critical angle is  $36.836^\circ$ . To obtain  $45^\circ$  exposure angles inside the SU-8 resist, a coupling prism and optical liquid glycerin (or called glyceryl) were required to compensate for refraction at these interfaces [26, 27, 30, 31] as schematically demonstrated in Figure 2.16. For  $\lambda = 405$  nm, the angle between the substrate and the horizontal direction is  $52.19^\circ$ . To provide refraction compensation when  $\lambda = 365$  nm, just change the angle of  $52.19^\circ$  to  $53.32^\circ$ .

### **7.3.2 Microfabrication of Pre-aligned Fiber Bundle Coupler**

The fabrication procedure for the pre-aligned fiber coupler using direct lithography is as follows: 1) conduct tilted exposures for the microlens and microlens array; 2) with the position between the substrate and the mask fixed and a shade mask to cover the pattern for the microlens or microlens array, use a tilted exposure for the fiber fixing grooves with full exposure dosages and different wavelengths; 3) develop the sample.

A layer of  $1100\text{ }\mu\text{m}$  thick SU-8 100 was spin-coated onto a silicon substrate at 400 rpm for 20 s. The sample was then soft-baked at  $110^\circ\text{C}$  for 10 hours and ramped down to room temperature in 8 h. Two consecutive exposures were done in the fabrication process while the optical mask and the wafer were held mechanically without any adjustment. In the first exposure, the sample was tilt-exposed at  $\pm 45^\circ$  to fabricate the microlens or microlens array. In this exposure, the exposure dosage and light source wavelength were carefully controlled to obtain the desired lens profile [9-11]. After the exposure for the microlens or microlens array, a shadow

mask was placed on the optical mask to cover the regions containing the microlens array. The second tilted-exposure at  $\pm 45^\circ$  was conducted to fabricate the fiber fixing grooves using a full exposure dosage. The sample was then post-baked at  $96^\circ\text{C}$  for 20 min and cooled down to room temperature in no more than 12 hours. After the unexposed regions were removed in development stage, the remaining exposed regions of resist formed the microlens array and fiber fixing grooves.

Three types of mask openings are used here: ellipse with long axis equal to  $\sqrt{2}$  times of the short axis and the long axis perpendicular to the lens' optical axis (Group 1); circular openings for ball lens (Group 2); and ellipse with long axis aligned to the lens' optical axis and equal to  $\sqrt{2}$  times the short axis (Group 3). Figure 7.3, shows an SEM Image of a prototype fiber bundle holders (Group 3) fabricated using the direct lithography method as presented in this chapter.

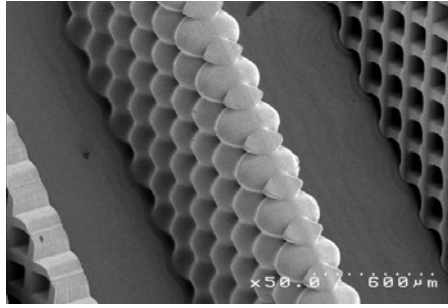
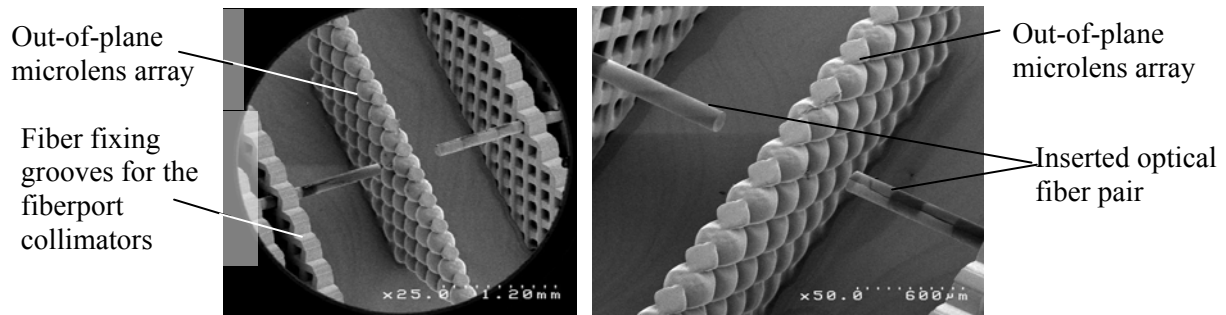


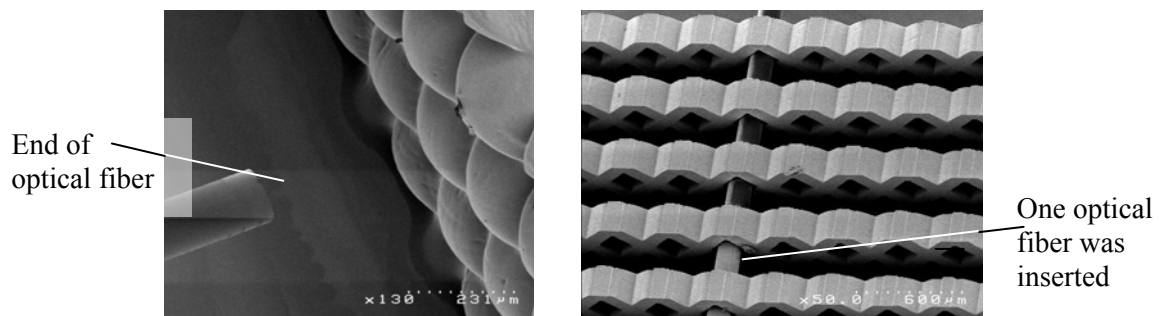
Figure 7.3, SEM image of a prototype fiber bundle holder (Group 3) fabricated using an elliptical mask pattern with long axis aligned to the lens' optical axis:  $250\sqrt{2}\mu\text{m}$  (L),  $250\mu\text{m}$  (S).

After obtaining the SU-8 microstructures for the out-of-plane microlens and fiber holder grooves, optical fibers were inserted into the fiber grooves to complete the construction of the fiber couplers for our optical tests. The optical fibers were prepared by stripping the plastic cladding from the fiber and then cut to a required length so that it can be inserted into the groove

holder of the coupler. When the fiber was inserted into the coupler, it was held in place by these grooves. The length of the stripped fiber determines the separation between the terminal of optical fiber and the surface of microlens.



(A)



(B)

(C)

Figure 7.4, SEM image for the fiber coupler (A) fiber coupler (B) surface profile of the out-of-plane microlens array (C) cascaded fixing grooves of the fiberport collimator

The ends of the optical fibers were stripped of their plastic coating by fiber stripping tools and fiber end terminated using a fiber cleaver (Thorlabs Inc., Newton, NJ). The terminated optical fibers were then inserted into the holding grooves of the fiber coupler. Figure 7.4 (A), (B) and (C) show several SEM images of the fabricated fiber coupler with only one optical fiber inserted into the array. From the SEM images, it can be seen that each pixel of the microlens is pre-aligned with its corresponding fiber holders.



## 7.4 Experimental Results and Discussions

A simple test was conducted to test the focusing capabilities of the microlens array. A collimated red light beam (about 630nm) was projected onto the backside of the out-of-plane microlens array and the focused image was acquired using CCD camera (DXC-960MD SONY) in a Nikon OPTIPHOT-88 optical measurement microscope. Figure 7.5 shows a photograph of the focused image. The pixels at the array's edge are partial microlens so the focal pads are not as bright as the pixels contained within the central region of the array. The pixel size of the microlens array shown in the photograph was  $247.89\text{ }\mu\text{m}$  by  $247.89\text{ }\mu\text{m}$ . The size of the focused pads can be estimated to have a diameter of  $18.72\text{ }\mu\text{m}$ .

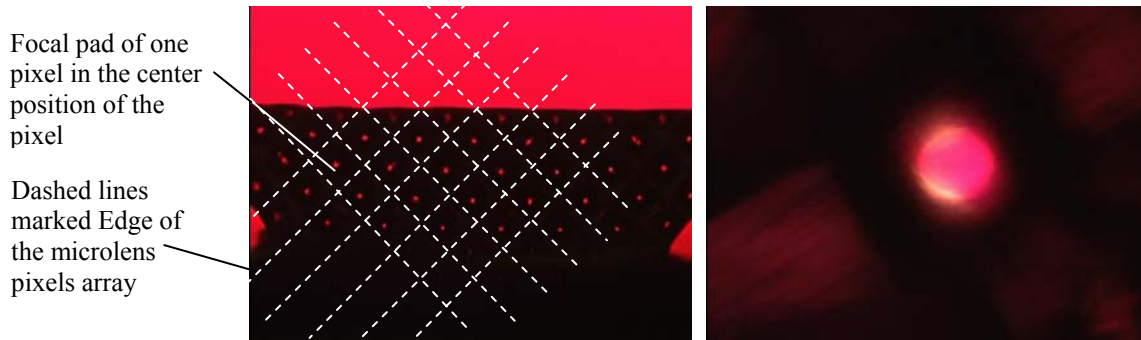


Figure 7.5, Optical images of the focal pads of the out-of-plane microlens array with collimated red light projected on the backside. The dashed white lines are used for visualization to help locate the individual pixels of the array. The picture at the right is a zoomed image of the focal pad.

The experimental setup for determining the optical system's coupling efficiency is schematically shown in Figure 7.6. A broadband light source (A1010 Arc lamp, Photon Technology International) or laser diode (DL5038-021, Thorlabs, Nowton, New Jersey) served as the light source, which was then focused using a coupling microscope objective lens ( $\text{NA} = 0.4$ , 40X). The plastic coating at the end of an optical fiber was stripped and then terminated using a cleaver. One end of the fiber was then fixed on the fiberport collimator facing the

microscope objective lens. The fiberport collimator's relative position was then adjusted with respect to the microscope lens to obtain maximum output power at the opposite end of the fiber. A power meter (FieldMate 1067353, Coherent Inc., Santa Clara, CA) was used to measure the input/output light power. In each measurement the end of the output fiber is perpendicular with the photo-cell and slightly touching on the center area of the cell surface. This will reduce the measurement error and improve the repeatability of focus/align. After the output power from the first optical fiber was measured, it was then inserted into one of the holder-grooves in the fiberport collimator with the help of a microscope. The second optical fiber (the receiving fiber) was inserted into the holder-groove on the opposite side. The output power,  $P_{out}$ , for the receiving optical fiber was then measured to obtain the coupling efficiency,  $P_{out}/P_{in}$  ( $dB = -10\log(P_{out}/P_{in})$ ).

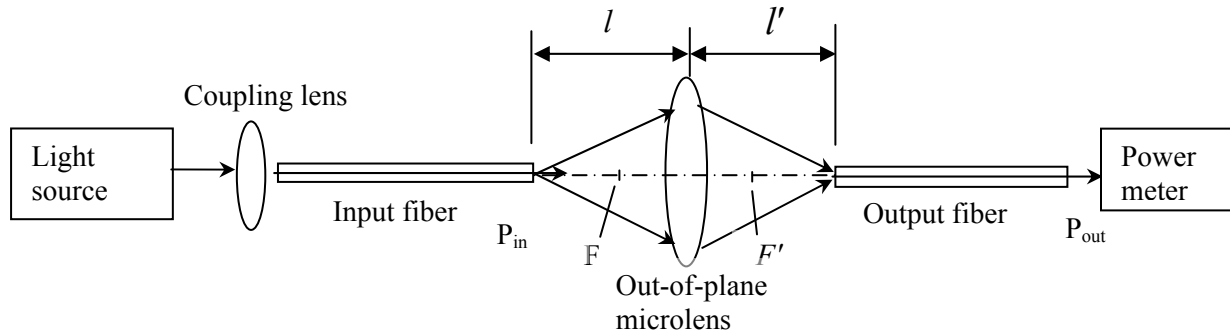


Figure 7.6, Schematic diagram of the experimental setup for determining the coupling efficiency of the fiber bundle coupler.

The distances between the fiber pair and the coupling microlens can be adjusted to obtain the highest coupling coefficient. Figure 7.7 shows a photo image of the prototype fiber bundle coupler with one pair of fibers inserted into the coupler and light supplied. The distances between the microlens array and the ends of the fibers,  $l$  and  $l'$ , are close to 2 times the focal length ( $f$ ) with  $l$  slightly longer than  $2f$  and  $l'$  slightly shorter than  $2f$ . If the numerical aperture (NA) of the microlens and the optical fiber are matched (i.e., microlens' NA equals or larger than

optical fiber's NA), the highest coupling efficiency ( $dB = -10\log(P_{out}/P_{in})$ ) can be achieved. In addition, the cross-talk between neighboring channels was also tested by measuring the output powers of several different receiving fibers not positioned directly within the optical train and compared with the input light power.

Both multi-mode optical fibers (GIF625 from Thorlabs Inc. Newton, New Jersey) and single mode fibers (TBII single mode fiber, Corning Inc., Corning, New York) were used in the tests for the fiber coupling efficiency. The GIF625 fiber is a graded index fiber with NA = 0.275 and a core diameter of 62.5  $\mu\text{m}$ . The TBII single mode fiber has a NA of 0.13 and core diameter of 8  $\mu\text{m}$ . Both a broadband light source and a 635 nm laser were used in these tests. For the multi-mode optical fiber, the coupling efficiency was measured to be 44.7% using the broadband light source, and 24.5% using a laser diode with a wavelength of 635 nm. For the single mode optical fiber, the coupling efficiency was found to be about 22.7% for the laser diode at 635 nm. Because the prototype lens has some significant aberration, this may have made the focus pad for broadband light sources better at some position, therefore higher coupling efficiency.

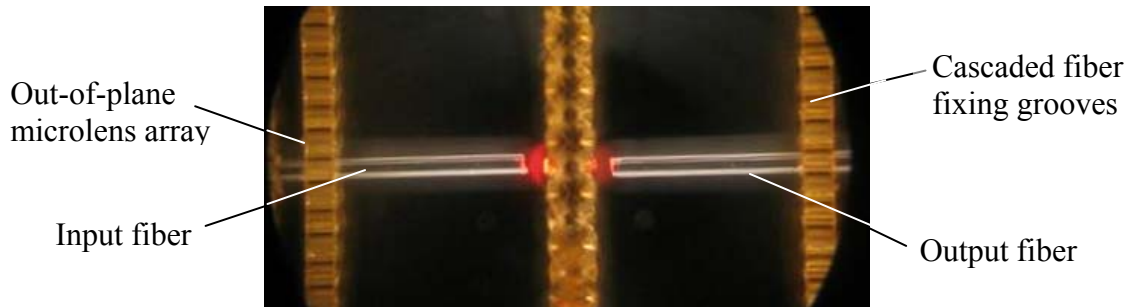


Figure 7.7, Photograph of the top view of the fiber bundle coupler with one pair of fibers inserted into the coupler and the light from a laser diode ( $\lambda = 635 \text{ nm}$ ) supplied to the fiber pair.

All three groups of out-of-plane microlens arrays with different surface profiles and dimensions were tested. The total coupling efficiency with the 635 nm laser is shown in Figure 7.8. For all of these fiber couplers, the cross-talk between neighboring fiber pairs was also

measured and the amount of light leaking into these fibers was too small to be measured by our power meter, therefore indicating that the degree of cross-talk was minimal.

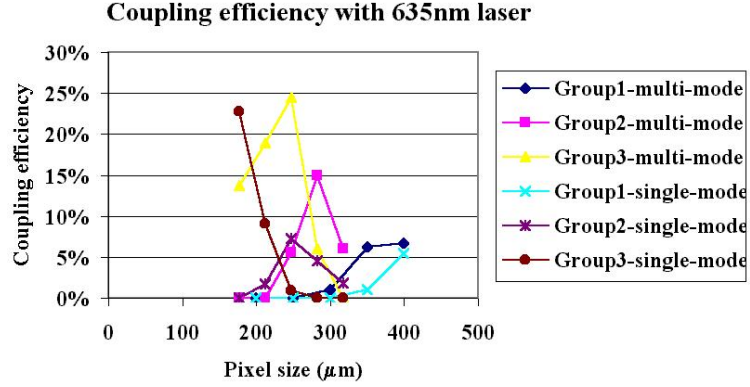


Figure 7.8, Coupling efficiency for the fiber coupler with different surface profiles and dimensions.

In the coupling efficiency test, the light reflection and the absorption by the structural material, cured SU-8 polymer, also needs to be considered. Partial reflection exists at the interfaces between materials of different refractive indices (such as air and glass, cured SU-8). The percentage of the reflection at a particular interface depends upon the refractive indices, angle of incidence and the polarization state of the light. In the case of normal incidence, the following equation is used to estimate the back reflection:

$$BR = \frac{(n_2 - n_1)^2}{(n_2 + n_1)^2} \quad (7.1)$$

At normal ( $0^\circ$ ) incidence, light transiting between air and another optical material with an index of 1.496 (fused silica at 632.8 nm) will suffer an insertion loss of 0.15 dB or 3.3% of the incident light reflected. At normal ( $0^\circ$ ) incidence, light transiting between air and material with an index of 1.596 (cured SU-8 at 632.8 nm) will have an insertion loss of 0.24 dB or 5.3% of the incident light is reflected. These reflections result in a reduction in the coupling efficiency of the

fiber-to-fiber coupler. To calculate the coupling efficiency for the fiber bundle coupler, reflections at a total of five interfacial surfaces need to be accounted for: one terminal of the input optical fiber, two lens' surfaces, and two terminal faces of the output optical fiber. The total insertion loss can be calculated as:

$$1 - (1 - 0.033)^3 \times (1 - 0.053)^2 = 18.9\% \quad (7.2)$$

The attenuation of the SU-8 microlens is estimated to be about 5%. The theoretical coupling efficiency (assuming losses only induced by reflection) that could be achieved is ~76.1% for the fiber-microlens-fiber coupler system presented in this work. However, the experimentally obtained coupling efficiency for this system was found to be 25% for the multi-mode fiber and 23% for the single-mode fiber as shown in Figure 7.8, which are much lower than the theoretical value of 76.1%

There may be three reasons for the lower than expected coupling efficiency: 1) the relative position between the optical mask and the photoresist changed during lithography; 2) the optical aberration caused the focal pads of the microlenses to become larger than the end size of the fiber core; 3) the numerical aperture numbers between the fiber and the microlens were not matched; and 4) errors caused by the fiber inserted into the holder.

In the foregoing estimation of coupling efficiency, it was assumed that no positional changes occurred between the mask and the photoresist on the substrate during the UV lithography of SU-8. However, glycerin liquid was filled between the resist on the sample wafer and the optical mask to minimize the diffraction caused by the significant air gap between the resist and mask. Glycerin is also necessary for the reflection composition for 45 degrees tilt exposure. A simple mechanical clip was used to hold the wafer and the mask during the tilted exposures (at  $\pm 45^\circ$ ). The glycerin liquid layer reduces the friction between the mask and the

photoresist, but increased the possible sliding movement. Positional shift between the mask and the photoresist on the substrate may reach several or even tens of microns. This shift caused errors in the subsequent multiple exposures and significantly reduced the fabrication precision and the alignment precision for the fiber coupler. The alignment error therefore contributed to the reduced coupling efficiency. A better design for the mechanical holder is therefore necessary to improve the lithography quality. The holder should permit rotation for well-controlled angles for the tilted lithography and maintain precise position control during lithography to avoid possible positional shift.

The diameter of the focal pads is determined by the surface profile of the microlens. The defects on the lens surface and the surface roughness may also affect the quality of the focal pads. In future work, the lithography conditions such as the mask pattern shape, exposure dosage, wavelength selection, development conditions, and bake conditions, need to be further studied to obtain the optimal process parameters for better surface profile and surface quality. In addition, optical aberration of the microlenses can be reduced by better control for the surface profile as further understanding for the relationship between development rate and lens profile is achieved in the future.

The prototype fiber coupler presented in this chapter used only one pixel of the microlens array. Using a single microlens may cause mismatch in the numerical aperture (NA) between the fiber and the microlens. Two cascaded microlenses with each lens symmetrically mirrored another lens for the fiber coupler, one for the input fiber and another for the output fiber, may help to improve the NA match and reduce possible longitudinal misalignment. In addition, this symmetrical structure will help to reduce the optical aberration for the lens pair. Further improvement may also be achieved by reducing the distances between the fiber holders and the

focusing lens to avoid misalignment caused by mechanical deflection of fiber that is basically a cantilever. In addition, variations in the lengths of the stripped fiber might also affect the longitudinal alignment accuracy and contributed to the signal loss.

Though further work is still needed to improve the performances of the prototype coupler before it can be used in telecommunications and other industrial applications, the experimental results presented in this chapter have proved the feasibility of a fiber bundle coupler with integrated microlens array. It is also proved that the device can be fabricated using direct UV lithography of SU-8. With the optical axis of pixels parallel with the substrate, each pixel of the microlens array is pre- aligned with the corresponding pixels of fiberport collimator arrays in lithography mask design, no additional adjustment and assembly are therefore required for the fabrication of the integrated fiber-coupler array. This helps to reduce the running cost and improve the alignment quality and coupling efficiency. Further improvement may be made using better mechanical holder in lithography to prevent sliding errors and two focusing lenses with symmetrically mirrored structure.

## **CHAPTER 8. A NEW TYPE OF NEGATIVE-TONE, UV LITHOGRAPHY PHOTORESIST BASED ON COMPOSITE OF EPON RESINS 165 AND 154**

### **8.1 Introduction**

As presented in the foregoing chapters, SU-8 has very good lithography properties. Cured SU-8 polymer also has excellent material properties. The results, it has been widely used in MEMS in recent years [1, 2, 16-18, 25-27, 29, 37, 41, 42, 45-47, 50, 103-105, 107, 110, 111, 123].

However, SU-8 has also been found to have several significant disadvantages. First, spin-coat properties for both thick and thin layers of resist are not good enough for some demanding applications. The edge-beam is always a problem for contact lithography. The second disadvantage is debonding problem after postbaking and development. The third one is cracking problem at the corners of the microstructures. Because the spin-coating property of SU-8 is not very good, flatness errors of the resist film may reach to more than one hundred micrometers from the central region of the wafer to the edges for resist layer with thickness more than 1000 micrometers. The flatness errors in photoresist may cause serious diffraction in lithography and make it extremely difficult to obtain high aspect-ratio microstructures across the entire wafer. To overcome this difficulty, some researchers reported to use fly-cut machine to obtain a better surface flatness mechanically. However the fly-cut process takes extra time and may cause other problems, such as changing properties at the surface layer of resist, even resulting in thermal curing in some local spots of resist surface.

Debonding problem typically happens after postbaking and development. For commonly used substrates such as glass, adhesion strength may be a quite challenging issue. The main



reason behind this phenomenon is that cured SU-8 tends to have significant residual stress, which may cause the microstructures to debond from the substrate. For some patterns, such as long lines, this problem may become very serious and the lines are easily debonded from their two ends.

Cracking problem, caused by excessive residual stress, normally happens at the corners of the microstructure. SU-8 normally shrinks a few percentages of the volume during curing process. Because the bottom of the microstructure is bonded on the substrate and cannot shrink with the top part, this will cause the corners shrink in two different directions and result in cracks.

In this chapter, we present a new type of negative-tone photoresist based on composite resins with different molecular weights. The new resist is based on a mixture of EPON resin 154 and EPON resin 165 (Hexion Specialty Chemicals, Inc., Columbus, OH 43215) [124]. These two epoxy resins were mixed together in an optimized ratio and dissolved into the gamma-butyrolactone (GBL) solvent. There is no chemical reaction involved and the mixing process is a purely physical one. The solution is then photosensitized by adding triaryl sulfonium salt (such as, Cyacure UVI 6970 from Dow Chemical). The combination of these two epoxy resins has helped to provide some unique properties suited for both ultraviolet (UV) lithography and X-ray lithography of ultra thick resist layer.

In this chapter, the material properties and lithography properties of both 154 and 165 will be separately discussed first. Then, the material properties, lithography parameters, and experiment results for the resist based on composite of EPON resins 154 and 165 will be demonstrated. Finally, the potential applications and conclusions are provided.

## 8.2 Material and Lithography Properties of 154

EPON resin 154 is a polyfunctional epoxy novolac resin as a semi-solid under ambient temperature and with glass temperature lower than 20°C. EPON Resin 154 is phenolic based resin and has very high glass temperature. Its thermal cross-link temperature is 130~140°C. The equivalent molecular weight is 176~181g/eq, its viscosity is 5~12 Poise at 25°C, and density of 10.2lbs/gal. It has short molecular chain and lighter molecular weight compared with EPON resin 165. Chemical structure of EPON resin 154 is shown in Figure 8.1. After EPON resin 154 is cured, the resulting polymer forms a highly cross-linked composition exhibiting very high chemical resistance, high temperature resistance and dimensional stability. EPON resin 154 can be used as the basic component material to make photoresist by adding photo initiator or mixed with other liquid epoxy resins such as EPON resin 828 or EPON resin 862 to develop specific process and application properties. EPON resin 154 reacts with many kinds of curing agents. The resin is widely used in chemical resistant tank linings, flooring and grouts, electrical laminates and encapsulation, casting and molding compounds, construction and electrical adhesives [124].

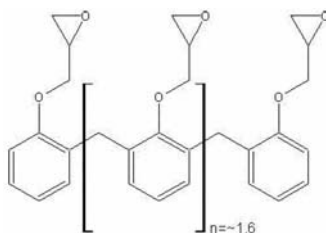


Figure 8.1. Chemical structure of resin 154. (Product data sheet, Hexion Specialty Chemicals, Inc., Columbus, OH)

From the molecular structure shown in Figure 8.1, it can be seen that EPON resin 154 has an average of 3.6 function groups, it therefore has high crosslink density after being cured. However, higher crosslink property results in lower flexibility and higher rigidity. Because of

its excellent surface properties, it can also be mixed with SU-8 to obtain improved adhesion, wetting properties, and better resist surface flatness.

To investigate the feasibility of developing a photoresist based on resin 154, EPON resin 154 was dissolved into GBL in a weight ratio of 15% GBL to 85% resin 154. A photo initiator, UVI 6970 was then added to the solution in a weight ratio of 16.15 to 1 and thoroughly mixed. The resulting solution is a photoresist that maintains semi-solid state at room temperature.

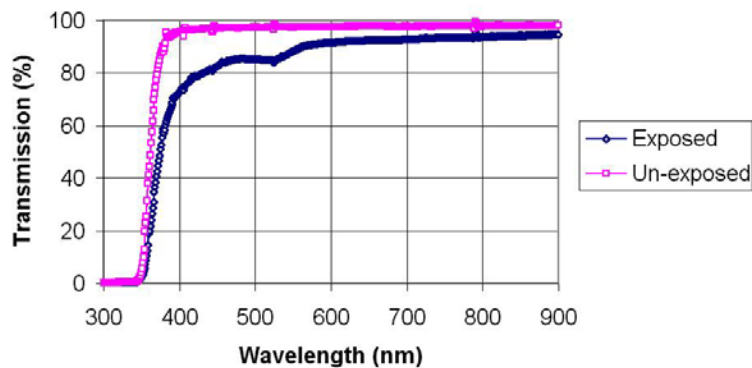


Figure 8.2. Transmission vs. wavelength curve for 152.8 $\mu$ m thick 154 film (For an un-exposed film, the transmission is 61.61% at 365nm, 95.17% at 405nm)

Experiments were conducted to measure the transmission properties of both exposed and unexposed resist. Figure 8.2 shows the transmission spectrum of EPON 154 based photoresist. As can be seen from the transmission spectrum in Figure 8.2, this EPON resin 154 based photoresist has very high transmission in near UV range. After cured with UV light, the cross-linked polymer also demonstrated excellent transmission property at wavelength longer than 600nm. In comparison with SU-8, there are two significant differences. First, the unexposed resist showed similar absorption at wavelength shorter than 400nm but lower absorption at wavelength longer than 400nm. The attenuation coefficients  $\alpha$  for un-exposed SU-8 are 0.0031/ $\mu$ m at 365nm and 0.0005 at 405nm. In comparison, the attenuation  $\alpha$  for un-exposed

EPON 154 based resist are  $0.0031/\mu\text{m}$  at 365nm and 0.0003 at 405nm. Second, the transmission of cured SU-8 polymer starts to decrease as the wavelength increases to more than 900nm while cured 154 polymer does not show such behavior.

Experiments were conducted to study the lithography property of EPON resin 154 based photoresist. The following is a typical process procedure adopted in our experiment: 1) Clean silicon wafer; 2) Spin at 500 rpm for 25 seconds and pre-bake at  $96^{\circ}\text{C}$  for 3.5 hours; 3) A small amount of glycerin is dropped on the central area of the resist to form a thin film between the mask and the 154 resist; 4) Expose with a broadband UV light source in a dosage of  $1000\text{mJ}/\text{cm}^2$ ; 5) Separate the mask from the wafer in DI water and blow dry using nitrogen gas; 6) Post-bake for 10 minutes at  $90^{\circ}\text{C}$ ; 7) Develop in glycol methyl ether acetate (PGMEA) for about half hours; 8) Rinse the sample with fresh PGMEA developer, followed with a rinse in IPA for 3 minutes, finally rinse with DI water, and naturally dry. Figure 8.3 shows two SEM images of some representative microstructures made using UV lithography of EPON resin 154 based photoresist.

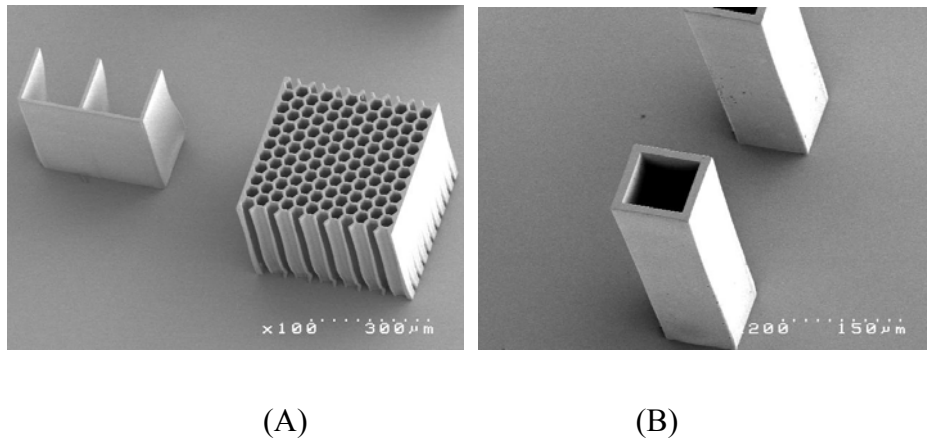


Figure 8.3. SEM images of sample microstructures made using photoresist 154 with *i*-line dominated UV broadband light source. (A) image of microstructures with sidewall thicknesses of  $3\mu\text{m}$  and height of  $370\mu\text{m}$ ; (B) Feature size is  $9\mu\text{m}$  wide and  $370\mu\text{m}$  high.

Because EPON resin 154 maintains semi-solid state at room temperature, the photoresist based on EPON resin 154 may stick with photo masks when it is used in contact lithography. It therefore can only be used in project lithography if no special measures are taken to avoid sticking to the mask.

One way to use 154 based photoresist in contact lithography while avoiding sticking with the mask is to apply a thin glycerin separation layer between the resist and the mask as used the foregoing process steps. This is a common practice in SU-8 lithography for air gap compensation. Because glycerin solution has a refractive index of 1.472 at 20°C, which is very close to that of unexposed SU-8 and EPON resin 154 based resist ( $n=1.668$  at  $\lambda=365\text{nm}$  and  $n=1.650$  at  $\lambda=405\text{nm}$ ), it can be used both for air gap compensation and as a separation layer between the EPON resin 154 based resist and mask to overcome sticking problem.

### **8.3 Material and Lithography Properties of 165**

EPON resin 165 is a cresol novolac epoxy resin with amber color and flakes state at room temperature. Its melting temperature is 91°C and the density is 10 *lbs/gal* [124]. Its physical properties (color, density, status, lithography properties, etc.) are very similar to those of EPON resin 157 (with SU-8 as its trade name), which is the main resin used in SU-8 photoresist.

As a Novolac resin, EPON resin 165 can also be used as the basic component material to make UV photoresist. First, EPON resin 165 was dissolved in GBL with weight ratios of 34% of GBL to 66% of EPON resin 165. A photo initiator, UVI 6970, was then added to the mixed solution in a weight ratio of 16.15 to 1 and thoroughly mixed. The resulting solution is a UV photoresist with the lithography properties very similar to those of SU-8.

The basic processing steps for photorsist based on EPON resin165 are as follow: 1) clean silicon wafer; 2) spin-coat the photoresist at 400 rpm for 25 seconds to obtain a 350  $\mu\text{m}$  thick

Cc1ccccc1OCC1OC1Cc2ccc(C)c(OCC3OC3)c2Cc4ccc(C)c(OCC5OC5)c4

researchers [1, 2, 8, 15-18, 20, 26, 29, 30, 32, 37, 38, 41, 42, 46-48, 50, 78, 103-106, 110, 111, 123]. However, EPON resin 165 based photoresist has a much shorter curing time. The overall quality of the microstructures obtained seems also very close to that obtained using SU-8 resist in our laboratory.

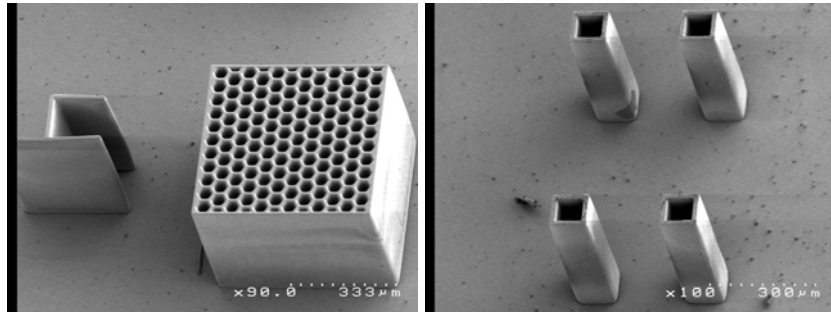


Figure 8.6. SEM pictures of the 351 $\mu\text{m}$  height microstructure made from photoresist 165 with 600  $\text{mJ}/\text{cm}^2$  in *i*-line dominated UV broadband (A) feature size 4 $\mu\text{m}$  (B) feature size 9 $\mu\text{m}$ .

In comparison with the resist based on EPON resin 154, the one based on EPON resin 165 maintains solid state at room temperature after pre-baking process. It therefore does not have the problem of sticking on the masks in contact lithography. This is obviously a significant advantage considering the fact that most of the MEMS fabrication laboratories still use contact lithography as primary technology.

However, there are several disadvantage in comparison with the resin 154 based resist. First, the EPON resin 165 based resist has higher cross-linking density and may cause higher internal stress. Secondly, the small exposure dosage difference between top and bottom layers of the resist may cause significant difference of curing condition because of the much higher cross-link density, sidewall profile of the microstructures may therefore be negatively affected. Third, the development rate is lower and it is relatively harder to clean any residuals in comparison with the SU-8 and EPON resin 154 based resists. Because EPON resin 165 has longer molecular

chain, it requires more GBL solvent to fully dissolve the resin for the similar level of viscosity compared with resin 154 or resin SU-8.

#### **8.4 Use the Composite of EPON Resins 154 and 165 in UV Resist for Optimal Lithography Properties**

From the study on the resists using either EPON resin 165 or EPON resin 154, it can be seen that the resists based on both resins have advantages and disadvantages. EPON resin 154 has excellent flexibility and mobilization. The resist based on EPON resin 154 has excellent surface flatness and adhesion, fast cross-link rate (curing rate) because of its much higher cross-linking density. However, it maintains a semisolid state at room temperature after pre-baking process. This makes it difficult to use in contact exposure. On the other hand, the resist based EPON resin 165 has higher molecular weight than EPON resin 154. It does not have the sticking problem, but the surface flatness error is at about the same level as SU-8. In comparison with SU-8, both EPON resins 165 and 154 have lower molecular weights, and therefore are better in flexibility and mobilization during processing. The best way to take the advantages of both EPON resins 154 and 165 is therefore to take a composite approach.

To find the optimal ratio to mix EPON resins 154 and 165 for the best possible material and lithography properties, experiments have been conducted using various ratios of resins 154 and 165 for optimal lithography properties. The procedure for making resist based on composite of EPON resins 154 and 165 is similar to ones presented in the foregoing sections. First, the two resins were mixed in a given ratio and then dissolved into gamma-butyrolactone (GBL) solvent. The mixing process is a pure physical one and no chemical process is involved. The mixture solution is then photosensitized by adding triaryl sulfonium salt (e.g., Cyracure UVI 6970 from Dow Chemical) in it.



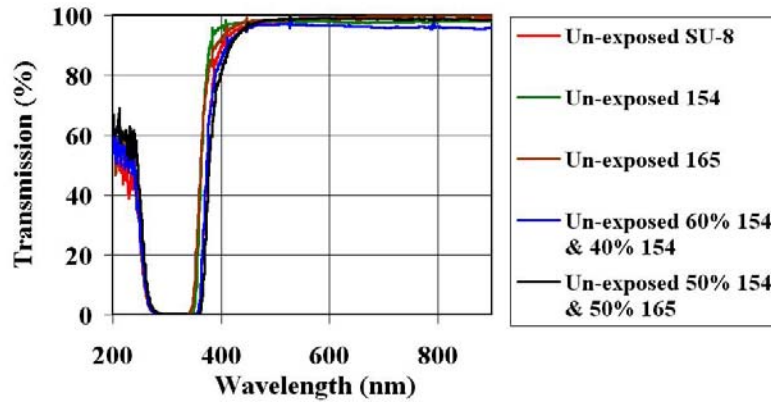
Experimental results have shown that when EPON resin 165 has weight ratio of more than 40% in the mixture, the resist turns into a complete solid state at room temperature after postbaking process. There is no sticking problem with photomask in contact lithography under reasonable level of pressure. This new class of resists based on composition of EPON resins 165 and 154 has some unique properties suitable for both ultraviolet (UV) lithography and X-ray lithography of ultra-thick resist layer.

#### **8.4.1 The Optical Properties of the Resist Based on EPON Resins 154 and 165**

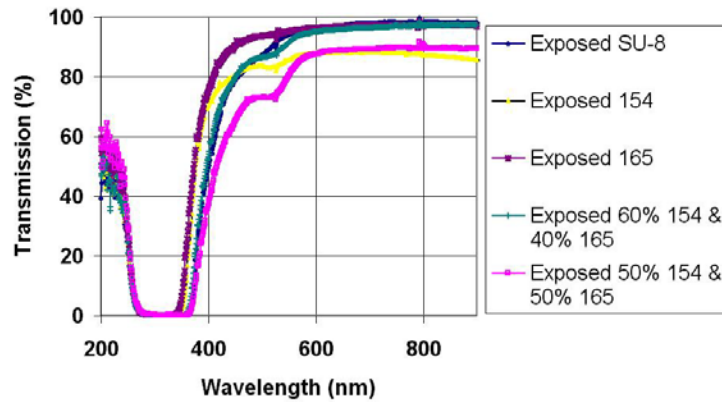
For the purpose of comparison, experiments were conducted to measure the absorbance and transmissions of resists based EPON resin 154, EPON resin 165, as well as the resists based on composite of EPON resins 154 and 165 in different weight ratios. The measured absorbance data are shown in Figure 8.7 (A) and the measured data of transmissions of different sample thicknesses are shown in Figure 8.7 (B).

The proper molecular weights of EPON resins 154 and 165 allow both resins to dissolve in many kinds of organic solvents to form very high concentration (around 80% weight in solution). It is therefore possible to obtain mixture with high viscosity. This is very important in obtaining ultra thick resist layers for fabrication of high aspect ratio microstructures. It is also found that the photoresist based on the composite of EPON resins 165 and 154 has very high optical transmission in the near UV spectrum as shown in Figure 7 (A). For a 493.6 $\mu$ m thick un-exposed resist film with EPON resins 154 and 165 in weight ratio of 40 to 60, UV transmission is about 22.70% at 365 nm and 87.43% at 405 nm. In another experiment of composite resist with EPON resins 154 and 165 in a weight ratio of 50 to 50, an 540 $\mu$ m thick un-exposed film shows an UV transmission about 25.01% at 365 nm and 85.23% at 405nm.

The high transmission of un-exposed resist means that the exposing light can penetrate very thick resist without significant attenuation; this makes it very suitable for fabrication of high aspect ratio microstructures.



(A)

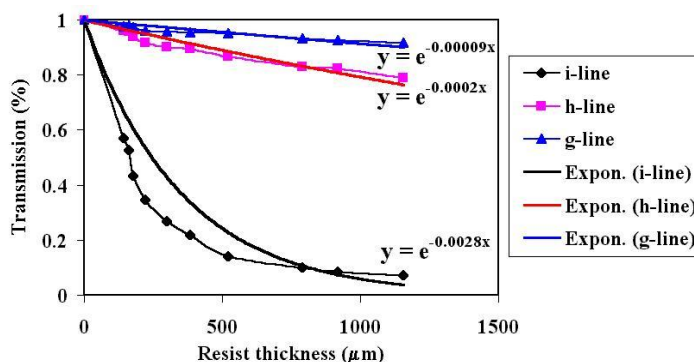


(B)

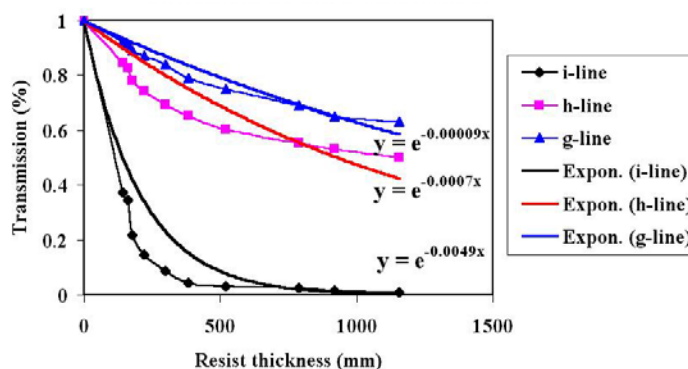
Figure 8.7. Measured results of transmissions for unexposed resists (Figure 7A) and exposed resists (Figure 7B). Several different resist samples with different thicknesses were tested: (1) resist film based on composite of ENPN resins of 154 and 165 in weight ratio of 40%:60% at 493.6 $\mu$ m; (2) resist film based on composite of ENPN resins of 154 and 165 in weight ratio of 50%:50% and thickness of 768.7 $\mu$ m; (3) resist based on EPON resin 154 at thickness of 152.8 $\mu$ m; (4) resist based on EPON resin 165 with a thickness of 108.4 $\mu$ m; (6) SU-8 resist with thickness of 396.8 $\mu$ m.

Experiments were also conducted to measure the absorbance coefficient of resist based on composite of EPON resin 154 and 165 in weight ratio of 50% to 50%. The transmissions of

the un-exposed resist at different thicknesses were measured first, the absorbance coefficients at different wavelengths were then calculated using the measured transmission data. The results are shown in Figure 8. As can be seen from Figure 8, the absorbance coefficient is 0.0028 for *i*-line, 0.0002 for *h*-line, and 0.00009 for *g*-line.



(A)

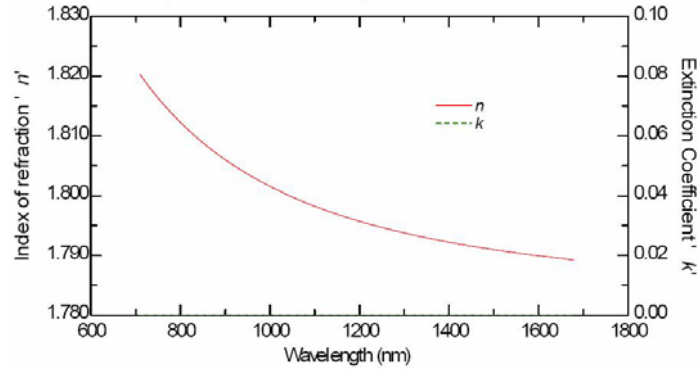


(B)

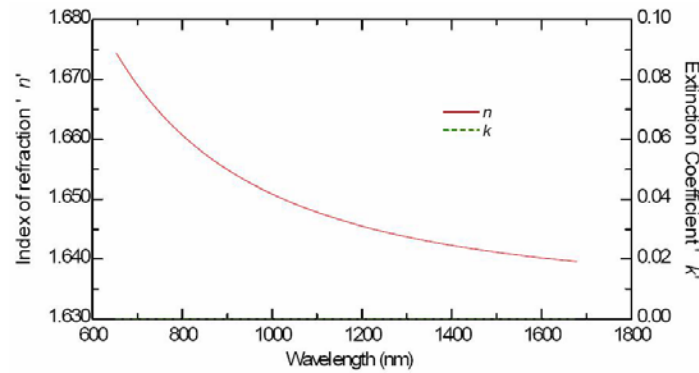
Figure 8.8. Measured transmissions of the un-exposed and exposed resist based on the composite of EPON resins 154 and 165 in weight ratio of 50% to 50%.

The resist based on composite of EPON resins 154 and 165 at a weight ratio of 50% to 50% was also analyzed using TA DSC thermal analyzer. Experimental results show that the resist starts the thermal cross-link at the temperature of 140°C without any exposure. The glass

temperature of cured 154 and 165 composite with weight ratio of 50% to 50% is about 130°C. In comparison, the glass temperature of cured SU-8 is higher than 220~230°C.



(A)



(B)

Figure 8.9. The measured relationship between refractive index and wavelength for the resist based on based the composite of EPON resins 154/165 in weight ratio of 50% to 50%. (A) measured results for unexposed resist; (B) measured results for cross-linked polymer.

#### 8.4.2 Lithography Properties of Resist Based on EPON Resins 165 and 154

After running tests with various weight ratios of resin 154 and 165, it has been found that the optimal ratio for EPON resins 154 and 165 is from 40%:60% to 50%:50%. The mixture of EPON resins 154 and 165 composite is first dissolved into gamma-butyrolactone (GBL) to form 85% weight concentration solution. A photoinitiator, Cyacure UVI 6970, is then added into it at a 5% weight ratio.

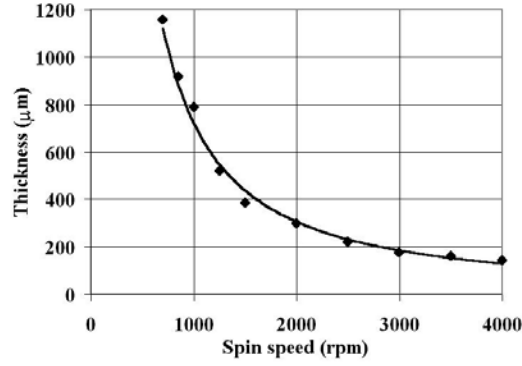


Figure 8.10. Spin-coat curve for the resist based on the composite of EPON resins 154 and 165 in a weight ratio of 50%:50%. The resist's weight ratios are 80.75% resins (40.375% for each resin), 14.25% GBL, and 5% UVI 6970.

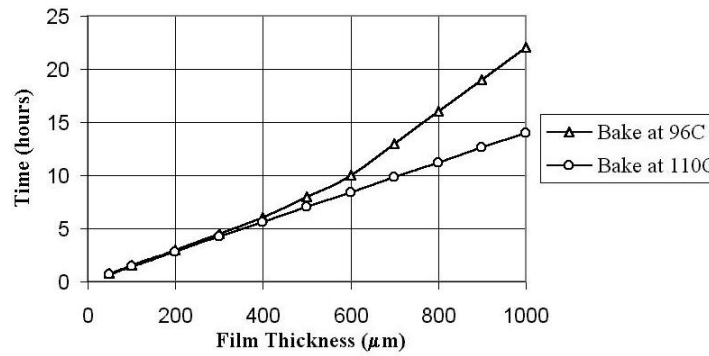


Figure 8.11. Recommended pre-exposure bake time vs. 154/165 film thickness

Film thickness between 1000~1500μm can be obtained with a single spin-coating step. The resist is typically baked on hot-plate for 14 hours at 110°C. Lithography is done using broadband UV light source containing *i*, *h*, *g* -lines. The pre-bake temperature needs to be lower than 125°C because the resist can be thermal cured at temperature higher than 140°C. The spin-coat property of the resist based on the composite of EPON resins 154 and 165 at weight ratio of 50% : 50% was calibrated with the results shown in Figure 8.10. The recommended pre-exposure bake conditions for resists with different thicknesses are shown in Figure 8.11.

The recommended UV exposure dosages at for light with different wavelengths and different film thicknesses are shown in Figure 8.12. For resist film thinner than 500μm, a

broadband light source can be used following the recommended exposure dosage shown in (A). When the film thickness is more than 500 $\mu\text{m}$ , the exposure dosage shown in (B) is recommended with an h-line dominated light source in which the *i*-line component eliminated as suggested by Yang and Wang [25]. For resist based on composite of EPON resins 154 and 165 in weight ratio of 50% to 50%, the recommended exposure dosage is 48 J/cm<sup>2</sup> for *h*-line dominated broadband light for resist thickness between 700 $\mu\text{m}$  to 1000 $\mu\text{m}$ .

Because this new type of UV resist based composite of EPON resins 154 and 165 has excellent surface wetting properties, the surface flatness of the spin-coated resist films is proved to be extremely high. Our experiments have proved that this new type of resist based composite of EPON resins 165 and 154 can cover the entire wafer surface area in high uniformity even by simply pouring a given amount resist on the wafer with no spin-coating done at all.

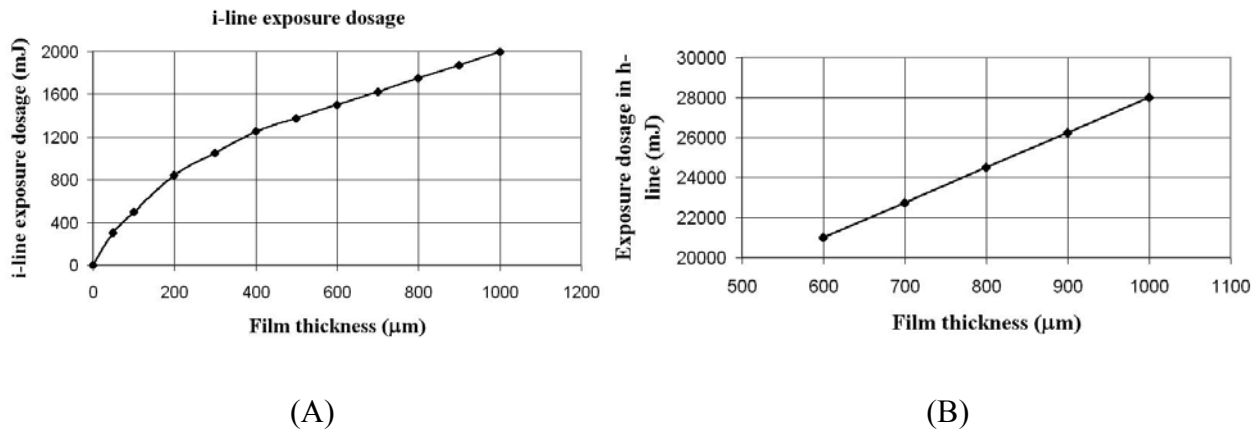
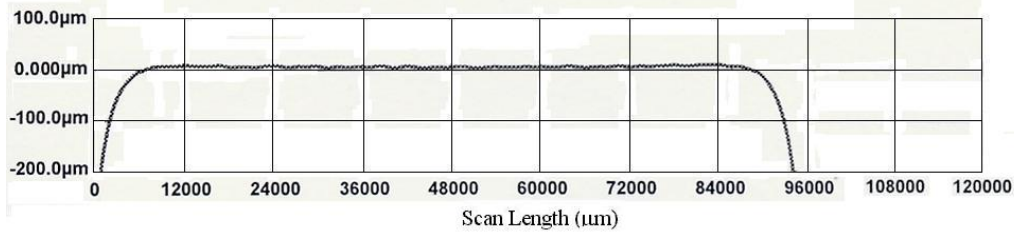
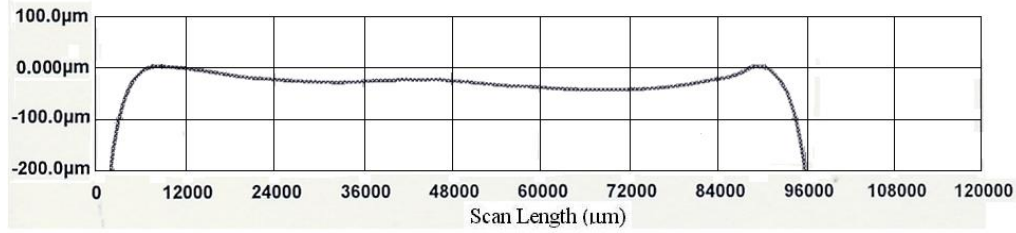


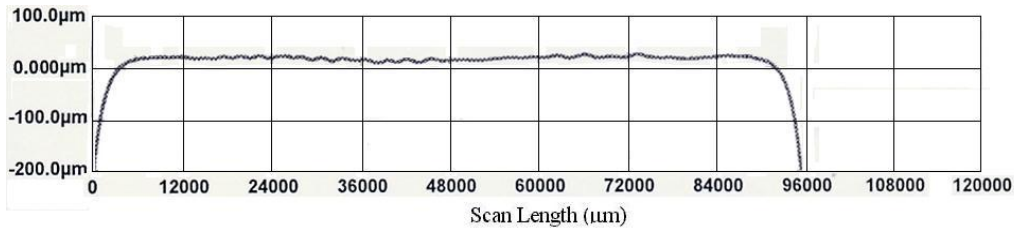
Figure 8.12. Recommended exposure dosages vs. 154/165 thicknesses with EPON resins 154 and 165 in weight ratio of 60% to 40%. For film with thickness less than 500 $\mu\text{m}$ , (A) can be used; for film with thickness 500 $\mu\text{m}$ ~1 $\mu\text{m}$  or more than 1mm thin, exposure dosage can just use the h-line in (B), but if combining the dosage for i-line in (A) and h-line in (B), better lithography result can get. The recommended exposure dosage for resist based on EPON resins 154 and 165 in weight ratio of 50% to 50%. Exposure dosage is 48 J/cm<sup>2</sup> *h*-line dominated broadband for thickness 700~1000 $\mu\text{m}$ .



(A)



(B)



(C)

Figure 8.13, The measured surface flatness results for spin-coated and prebaked. All films are 1mm thick. (A) Resist based on the composite of EPON resins 154 and 165 in ratio of 50% to 50%; (B) SU-8 2100; (C) SU-8.

Figure 8.13 shows the calibrated the surface profiles measured using Tencor P-2 Long Scan Profiler (KLA-Tencor, San Jose, CA, USA). For the experimental results shown in Figure 13, all samples were spin-coated and pre-baked. In the results shown in Figure 13, the TIR (Total Indicator Run out) is defined as the difference between maximum and minimum profile heights for section of plot between measurement cursors. The surface profiles shown in Figure 13 demonstrated that, TIR is 5.4924  $\mu\text{m}$  across a span of 80mm of the resist surface area for the new resist presented in paper, 17.75  $\mu\text{m}$  for SU-8 2100 resist, and 46.03  $\mu\text{m}$  for SU-8 100 resist. It

can therefore be concluded that the new type of resist based on the composite of EPON resins 154 and 165 has much better surface planarization property than SU-8, the commercially available resist SU-8.

### **8.4.3 Lithography Results and Discussions**

Though further study is still needed to optimize the lithography conditions for the new type of resist based on the composite of EPON resins 154 and 165, the preliminary study has demonstrated excellent lithography results using a UV light source. For this new type of resist based on the composite of EPON resins 154 and 165 in a weight ratio of 50% to 50%, the final resist has 80.75% resin, 14.25% GBL, and 5% UVI 6970. A recommended processing procedure is as follows:

- 1) Spin coat resist for 25s at a particular speed to get desired film thickness. Suitable spin speed can be found from the spin-coat curve shown in Figure 8.9;
- 2) Pre-bake the photoresist. The temperature is first ramped up from 20°C to 75°C in 30mins, dwelled at 75°C for 10mins, increased to 96~110°C in 30mins, dwelled again at 96~110°C for a time period (depending on particular film thickness), ramped down to 75°C in 30mins, dwelled at 75°C for 15mins. For film thickness of less than 500μm, the sample is then naturally cooled down to room temperature while for film thickness of more than 1mm it needs to be anneal by reducing to 55°C in 40mins, dwelled in 55°C for 4 hrs, ramped to 20°C in another 3hrs. The pre-exposure baking time can be determined using the baking curve shown in Figure 8.11;
- 3) Expose the photoresist film with broadband UV light for film thinner than 500μm. For ultra thick film (500μm~1μm or more than 1mm), light source with an optimize

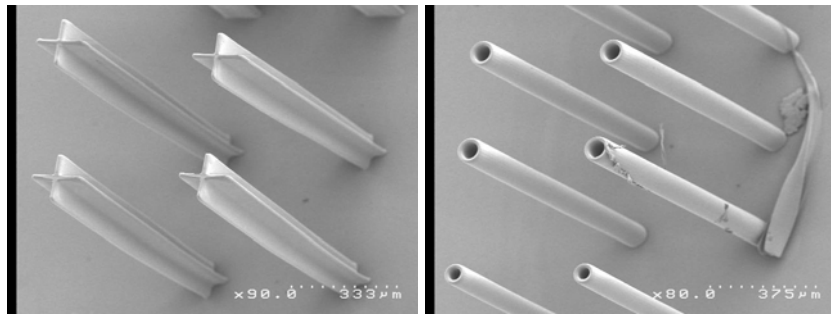


ratio between *h*-line and *i*-line wavelengths needs to be used. Our experiments show that the dosage ratio of *i*-line and *h*-line wavelengths should be about 1:14. The recommended exposure dosage shown in Figure 8.12 should be followed;

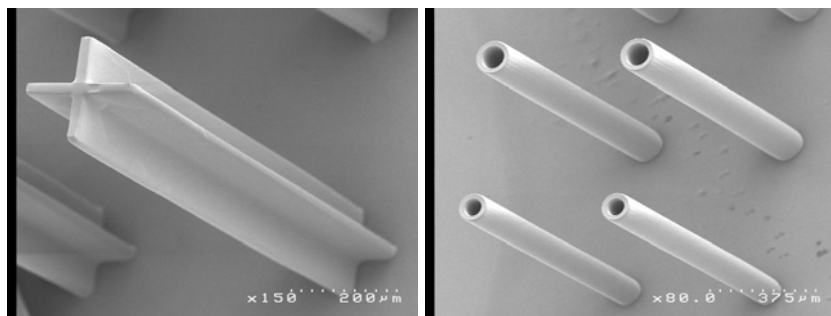
- 4) Post-bake the exposed sample. The postbaking temperature should be ramped up from 20°C to 75°C in 30mins, dwelled at 75°C for 10mins, then ramped to 96°C in 30mins, dwelled in 100°C for 30mins. The sample can then be ramped down to 75°C in 30mins, dwelled again at 75°C for 15mins. For film less than 500μm, the sample can then be naturally cooled to room temperature. For film thickness of more than 1mm, the sample needs to be annealed by reducing to 55°C in 40mins, dwelled in 55°C for 4hrs, and finally ramped to 20°C in 3hrs;
- 5) Develop the sample. The sample needs to be developed using PGMEA developer and then rinsed with IPA until no milk-like material is generated in developer solution. After complete development, the sample needs to be rinsed with IPA and DI water, and naturally dried.

Figure 8.14 and Figure 8.15 show a group of SEM images of some representative microstructures obtained using the new resist based on the composite of EPON resins 154 and 165. The images of microstructures as shown in Figures 14 and 15 show that the new resist based on the composite of EPON resins 154 and 165 has excellent UV lithography properties. The microstructures shown in Figure 14 have a height of 1028 μm and aspect-ratios of more than 50. The microstructures also demonstrated excellent sidewall quality. The microstructures shown in Figure 15 have an average height of about 1159 μm and aspect-ratios of about 100. These results are much better than the ones for SU-8 reported in the field. These microstructures shown in

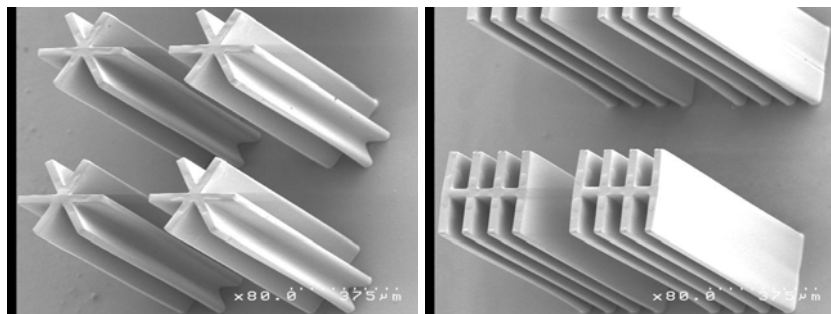
Figures 14 and 15 also do not have any cracking patterns at the corners of the microstructure, a common phenomenon for cured SU-8 microstructures.



(A) Crosses and cylinders with designed wall thicknesses of  $15\mu\text{m}$  (aspect-ratio: 68.5)

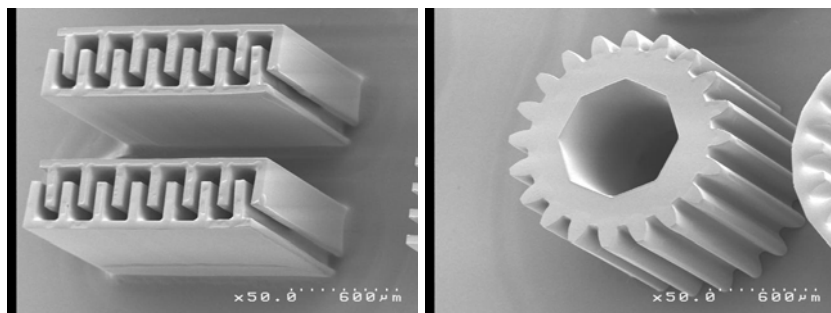


(B) Crosses and cylinders with designed wall thicknesses of  $20\mu\text{m}$  (aspect-ratio: 51.4)



(C) Micro-sized crosses with designed wall thickness of  $30\mu\text{m}$  (aspect-ratio: 34.3)

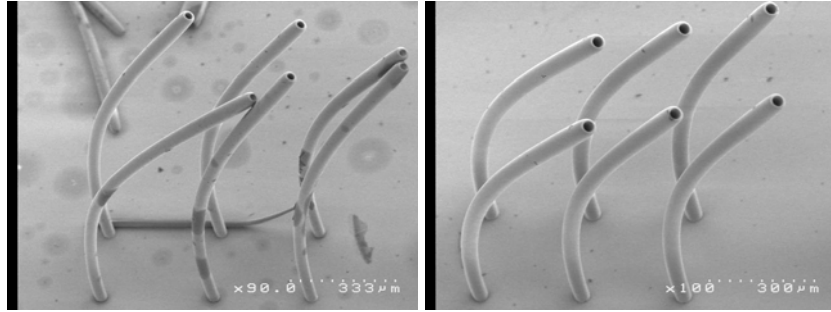
Figure 8.14. SEM pictures of the ultra high-aspect-ratio microstructures made from photoresist based on EPON resins 154 and 165 at a weight ratio of 60%:40%,. The lithography was done using a dosage of  $28\text{J}/\text{cm}^2$  and *h*-line dominated UV broadband light source. The height of the microstructures is  $1028\mu\text{m}$  (Figure continued)



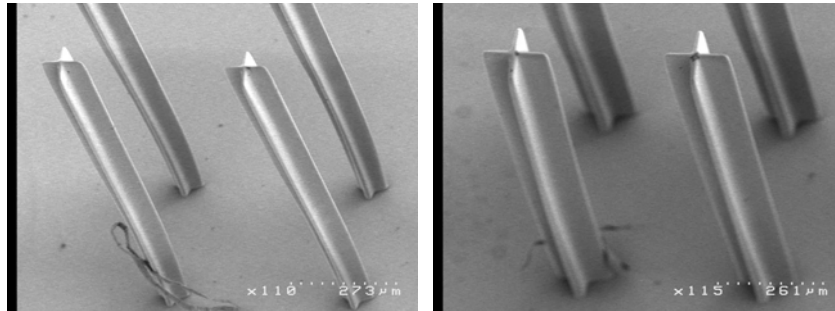
(D) Comb and gear patterns

The improved lithography properties can be explained by inspection of the chemical structures of EPON resin 157, the main component of SU-8 resist in addition to photo initiator. It can be seen from its chemical structure that EPON 157 (a BPA based Novolac resin) is high in molecular weight and functionality. It has function groups at both sides, leading to a physical behavior that is much less flexible during application process. The lower flexibility in its structure may lead to significant internal stress during the curing process. The cast resin may therefore be seriously damaged. This often causes cracking during application process. In addition, it may take much longer time to achieve the desired cross-link degree for SU-8 than that required for EPON resins 154 and 165 under the same thermal conditions.

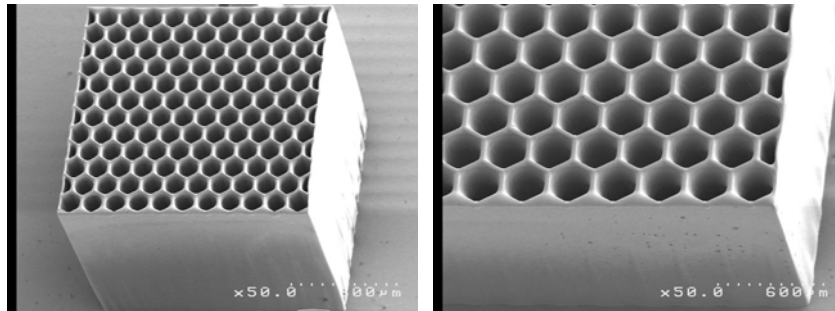
EPON 154 is lower in MW than EPON 165 and better in flexibility and mobilization during processing. Both EPON 154 and EPON 165 have lower molecular weights (MW) compared to EPON resin 157, the main component of SU-8 resist. However, the low MW of ENPON 154 and its semi-solid state in room temperature make the application process difficult. The optimal approach is obviously to use the composite of EPON resins 154 and 165 at a desired ratio. This helps to overcome the process difficulty of EPON 154 while taking the advantages of its other excellent properties. This physical and lithography properties of the new EPON 154/165 resist system would exceed those of the EPON 157 based one, such as SU-8.



(A) Micro cylinders with the designed wall thicknesses of 7 $\mu$ m (left) and 8 $\mu$ m (right)

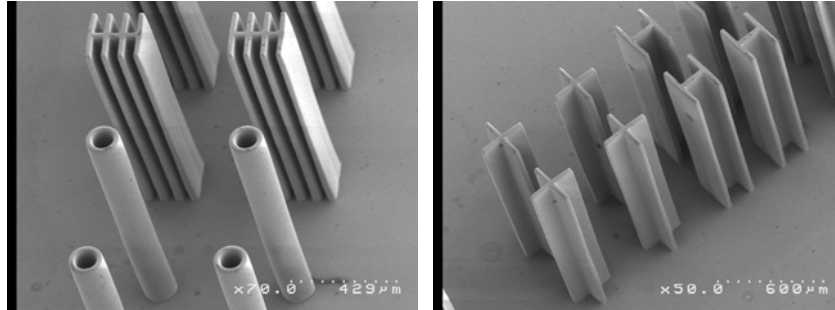


(B) Micro crosses with the designed wall thicknesses of 10 $\mu$ m (left) and 15 $\mu$ m (right)

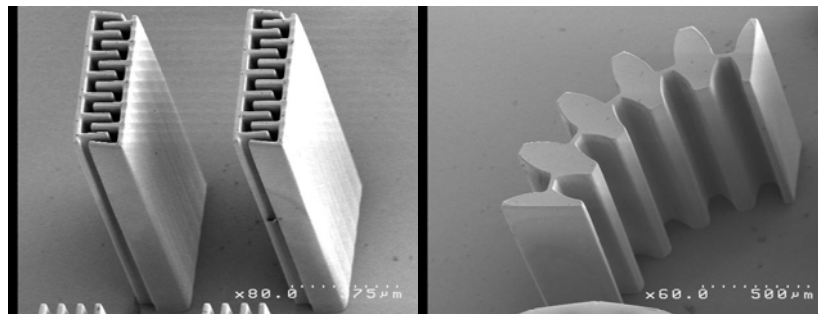


(C) Micro comb structures with the designed wall thicknesses of 10 $\mu$ m (left) and 20 $\mu$ m (right)

Figure 8.15. SEM images of the ultra high aspect-ratio microstructures made from photoresist based on composite of EPON resins 154 and 165 in a weight ratio of 50% to 50%. The exposure was done with 48J *h*-line dominated UV broadband light source. The height of the microstructures is 1159  $\mu$ m. (Figure continued)



(D) Micro cylinders and crosses with the designed wall thicknesses of 20μm



(E) Micro comb structure with 20μm designed line/space and micro gear with feature size of 20 μm. Both structures have the same height of 1159 μm

## 8.5 Advantages of the New Resist and Discussions

The experimental results have proved that there are four major advantages with the composite resin approach in developing new resist: 1) the proper molecular weights allow both of the fraction materials dissolved into many kinds of organic solvents to form very high concentration mixtures (around 80% weight in solution) and high viscosity mixtures; 2) the new resist has very high optical transmission in the near UV spectrum and excellent lithography properties; 3) it has very good surface wetting properties helps to obtain excellent surface flats across the entire wafer area; 4) it has excellent adhesion property and does not require any special treatment of wafer surface; 5) minimal cracks were observed in the microstructures because the structural flexibility of these two epoxy resins.

Because SU-8 is based on EPON resin 157 that has high molecular weight and has function groups at both sides of the molecular structure, it has higher functionality, and therefore less flexibility. This may cause cracking during application process. In addition, it takes much longer time to cross-link. In comparison, EPON 154 and EPON 165 are low in MW and therefore, structurally better in flexibility and mobilization during processing. The resist based on the composite of EPON resins 154 and 165 at an optimal ratio therefore is highly resistant to cracks and provide much better application performances. The experimental results have proved that the new resists has superior lithography properties and can be used for ultra high aspect ratio microstructures with excellent sidewall quality.

Though further study is still needed, the experiments have proved that microstructures with aspect-ratios of more than 100 can be achieved using ultraviolet lithography of more than 1mm thick photoresist film. Microstructures with height of more than 1000  $\mu\text{m}$ , 10  $\mu\text{m}$  feature sizes, and excellent sidewall quality were successfully obtained. This new resist may have many potential applications in microfabrication and MEMS systems. The resist in particular can be useful in bio-MEMS or microfluidic devices or systems that require polymer structures.

## **CHAPTER 9. CONCLUSIONS AND FUTURE WORK**

The UV lithography of ultra thick resists, such as SU-8 and the new resist based on the composite of EPON resins 154 and 165 as presented in Chapter 8, have wide applications in microfabrication and MEMS systems. There are also many challenging research issues in this important field. The research work presented in this dissertation has the following major achievements and conclusions:

- (1) Numerical simulations were made to analyze the images of the light as it penetrates the thick SU-8 film. The effect of diffractions, wavelengths, dependence of absorption on wavelengths, air gap and different ways to compensate for them, as well as the substrate surface were considered in the simulations. Experiments were also conducted to validate the results of numerical simulations. Optimal lithography conditions were obtained based on the numerical simulations and experiments. As the results, microstructures with excellent sidewall quality and aspect ratios more than 100 have been obtained using the UV lithography of SU-8 following the optimal processing parameters. The results obtained are the best ones for UV lithography of SU-8 reported in MEMS field.
- (2) Tilted lithography of SU-8 with compensation for refraction error has also been developed to obtain perpendicularly intersected exposures. This unique method of tilted lithography of thick SU-8 resist has been used in fabrication of several useful microdevices.
- (3) With better understanding of the lithography process of thick SU-8 resist, two-level mold insert has been fabricated with desired tapering angles. Low cost replications of such as biodegradable materials such as PLGA have been realized for applications in implanted

long term drug delivery. This type of implantable drug delivery system can potentially be used for long term, on-spot delivery of drugs.

- (4) Because cured SU-8 has excellent optical properties, it can be used to make micro optical components and systems. However, there were very limited work reported in MEMS field before we work on this subject. A novel technology has been developed to fabricate out-of-plane microlens that does not require alignment and assembly. The microlens can potentially be used as a key component for truly 3-D, free-space integrated micro-optic devices and systems in a wide variety of scientific and industrial applications. Mathematical model has been developed and numerical simulations have been conducted to provide better understand the surface forming mechanism of the microlens during development process. With the help of the mathematical model and numerical simulation tool, it would then be feasible to control the surface profile and focus length of the microlens. **A US patent application has been filed by the Office of Intellectual Properties of LSU.**
- (5) As a simple application of the SU-8 based microlens, a novel optical fiber bundle with integrated focusing lens and fiber collimators has been successfully designed, fabricated, and tested. **A provisional US patent application has been filed by the Office of Intellectual Properties.** A private company has expressed their interests for potential technology transfer.
- (6) Mixing different fluidic samples or reagents at microscopic scale is a very challenging issue. Various research efforts have been reported in the MEMS field with limited success. A novel truly three-dimensional micro-mixer based on spatially impinged micro-jets has been successfully designed, fabricated, and tested. The fabrication is based on UV lithography of SU-8. The experimental results have proved that the mixer has



excellent mixing efficiency. **A US patent application has been filed by the Office of Intellectual Properties of LSU.**

- (7) Traditional flow cytometers have large physical sizes and are expensive. Most of the reported research efforts to make micro-sized cytometers take a two-dimensional design approach. The main reason behind this choice is the limitation of the two dimensional nature of the silicon micromachining. Using direct UV lithography of SU-8, a novel, truly three-dimensional hydrofocusing unit has been successfully designed, fabricated, and tested for micro flow cytometry applications. This three-dimensional hydrofocusing unit has the advantages of focusing cells and other biological samples accurately and effectively for high precision measurement. It can be integrated with the micro-optic components such as out-of-plane microlens, to make a completely integrated lab-on-chip system for remote care applications.
- (8) In the research effort to develop a new type of UV resist with optimal lithography properties for fabrication of high aspect ratio microstructures, it has been found that the EPON resins 154 and 165 can be used to make a new negative tone resist. The optimal ratio between EPON resins 154 and 165 should be between 40%:60% to 50%:50% in weight ratios. The mixture of EPON resins 154 and 165 composite is first dissolved into gamma-butyrolactone (GBL) to form 85% weight concentration solution. A photoinitiator, Cyacure UVI 6970, is then added into it at a 5% weight ratio. The experimental results using this new type of UV resist have proved that it has excellent lithography and material properties. The microstructures fabricated using this new type of resist has excellent sidewall quality and may reach an aspect ratio of more than 100. The resist also showed much better surface flatness and much stronger adhesion than

those of SU-8. **A patent disclosure has been filed with the OIP of LSU.** It may be used in MEMS and microfabrication applications.

## Future Work

The future work includes two major subjects: the first one is to continue the research on the fiber bundle coupler and the second one is to conduct study on surface profile control of the out-of-plane microlens based on direct UV lithography of SU-8 and the new resist based on the composite of EPON resins 154 and 165.

The research on new fiber bundle coupler includes improved design for the fiber bundle coupler presented in Chapter 7. The fiber couplers in Chapter 7 have lower coupling efficiency than expected. There are three major reasons for it: 1) the numerical aperture of the coupling lens does not match what required by the fiber; 2) the microlens' aberration might have caused the focal pad to be bigger than the core of optical fiber, 3) the possible slip of the mask relative to the photoresist. The improved fiber coupler can be fabricated using direct UV lithography of SU-8 or the new thick photoresist based on the composite of EPON resins 154 and 165. In the new design as shown in Figure 9.1, two symmetrical microlenses will be used to obtain better match between the numerical apertures of the fiber and the microlens pair. The symmetrical microlens pair will also help to reduce the optical aberration for higher focal pads quality.

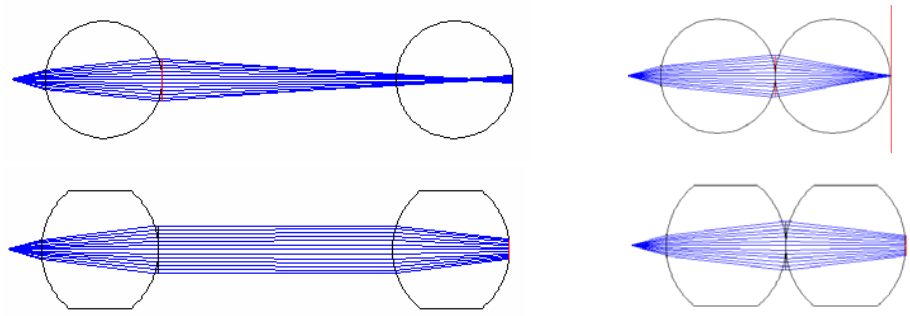


Figure 9.1 The new optical design for the fiber bundle coupler. Two microlenses are adopted symmetrically.

In addition, the set-up based on the scheme shown in Figure 9.2 needs to be used in lithography. When the substrate is inclined at an angle of  $\theta$ , based on the geometrical relationship,  $\theta_7$  should be maintained at  $\theta-45^\circ$ .

According to Snell's Law, the following relations can be found:

$$n_1 \sin \theta_{11} = n_2 \sin \theta_{21} = n_3 \sin \theta_{31} = n_4 \sin \theta_{41} = n_5 \sin \theta_{51}, \quad (9.1)$$

$$n_1 \sin \theta_{12} = n_2 \sin \theta_{22} = n_3 \sin \theta_{32} = n_4 \sin \theta_{42} = n_5 \sin \theta_{52}, \quad (9.2)$$

$$\text{and} \quad n_7 \sin \theta_7 = n_5 \sin \theta_6. \quad (9.3)$$

From the geometrical relationship as shown in Figure 9.2, the following equations can be found:

$$\theta_6 + (90^\circ - \theta_{51}) = 45^\circ, \quad (9.4)$$

$$\theta_{51} = \theta_{52}. \quad (9.5)$$

Because the sum of the reflective angle  $\theta_5$  and the refractive angle  $\theta_{51}$  is 90 degrees,  $\theta_{52}$  is therefore equal to  $\theta_{51}$ . When  $\theta_5$  is larger than the critical angle of the prism, the total internal reflection happens and all of the reflected light from one sidewall of the prism's 90 degrees corner are used for the exposure. Finally, both the refractive angles ( $\theta_{11}$ ,  $\theta_{12}$ ) and the exposure energy along the refractive angles are the same. In order to obtain the total internal reflection, the refractive index of the prism needs to meet the following requirement:

$$1 \cdot \sin 90^\circ \leq n_5 \sin(90^\circ - \theta_{52}), \quad (9.6)$$

where the refractive index of the prism  $n_5$  needs to be more than 1.5366 (when  $n=1.650$  for SU-8 at  $\lambda=405\text{nm}$ ).

This approach may help to elimination of the requirement for the rotation of the optical mask and the substrate, therefore avoid possible relative slip between the resist and the mask.

Because the new resist based on the composite of EPON resins 154 and 165 has better adhesion and flexibility, there are less cracks and debonding problems with it. Both SU-8 and new photoresist based on the composite of EPON resins 154 and 165 were used in lithography. Figure 9.3 shows several SEM images of the prototypes of the improved design of fiber bundle coupler. Further study is still needed to calibrate the performances of the fiber bundle coupler. Based on the measured performances and analysis, the design can be further improved.

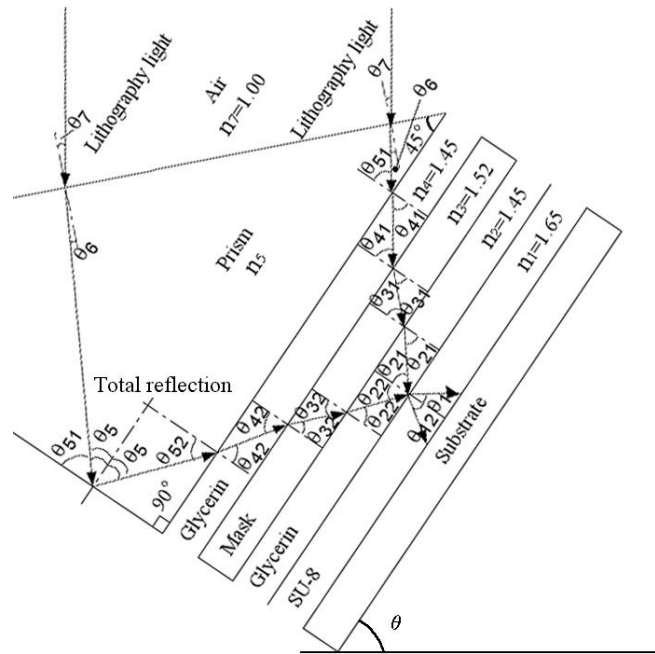


Figure 9.2 the total reflection on the prism with a 90 degrees corner.

The second part of the future work is to continue the study on the surface forming mechanism of microlens and the method to control the surface profile. To be able to control the surface profile of the microlens is very important for obtain high quality, integrated, and free-space optical benches. As presented in Chapters 6 and 7, the surface profile and the focus length of the out-of-plane microlens fabricated using direct lithography of SU-8 depends on several factors: the mask design, the exposure dosage, the wavelengths of the light source, particular pre-bake, exposure, post-bake, the development conditions and time. The mathematical model and

numerical simulations are very essential for understanding the surface profile forming mechanism and accurately control of the surface profile and focus lengths. A commercial lithography simulation software, Solid-E (Sigma-C, Germany), will be used to conduct the three-dimensional surface profile simulation. The etch properties of the photoresists, including SU-8 and the one based on the composite of EPON resins 154 and 165, will be experimentally measured and entered to the data base in Solid-E. A short program needs to be written and launched using Solid-E for the simulation of the surface forming mechanism. Based on the simulation results of Solid-E, some fabrication and test experiments will be done to compare with the ones from numerical simulations for further improvement of the mathematical model. The long-term goal is to develop a set of mathematical tools and design/fabrication guidelines to obtain the desired surface profiles and focus lengths for the microlenses and array of microlenses.

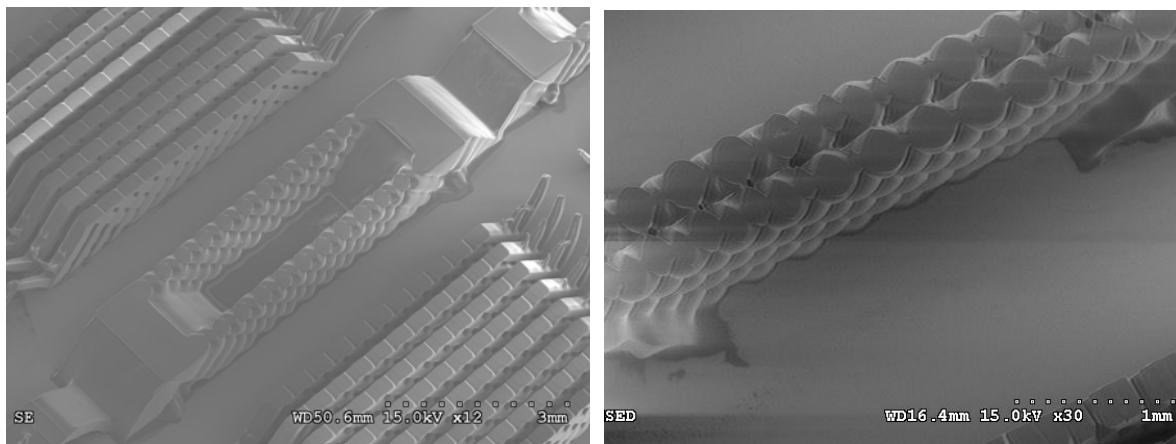


Figure 9.3 Some SEM pictures for the prototype of new fiber bundle couplers

## REFERENCES

1. H. Lorenz, M. Despont, N. Fahrni, N. Labianca, P. Vettiger, and P. Renaud. *EPON SU-8: A low-cost negative resist for MEMS*. in *Proc. of Micro Mechanics Europe'96*. 1996. Barcelona.
2. H. Lorenz, M. Despont, P. Vettiger, and P. Renaud, *Fabrication of photoplastic high-aspect ratio microparts and micromolds using SU-8 UV resist*. *Microsystem Technologies*, 1998. 4: p. 143-146.
3. H. Lorenz, M. Laudon, and P. Renaud, *Mechanical characterization of a new high-aspect-ratio near UV-photoresist*. *Micorelectronics Engineering*, 1998. 41/42: p. 371-374.
4. K. Lee, N. LaBianca, S. Rishton, and S. Zohlgharnain, *Micromachining applications for a high resolution ultra-thick photoresist*. *Journal of Vacuum Science and Technology B*, 1995. 13: p. 3012-3016.
5. N. LaBianca, J. Delorme, *High aspect ratio resist for thick film applications*. *Proc. SPIE* 1995. 2438: p. p846-852.
6. Catherine Oropeza, Kun Lian, and W. Wang. *Fracture Toughness Study on LIGA Fabricated Microstructures*. in *Photonics West*. 2003. San Jose, California.
7. Dong Eun Lee, Hang-Ping Chen, Steve Soper, and W. Wang. *An Electrochemical Micropump and Its application in a DNA Mixing and Analysis System*. in *Micromachining and Microfabrication, Photonics West*. 2003. San Jose, California.
8. H. Lorenz, M. Despont, N. Fahrni, J. Brugger, P. Renaud, and P. Vettiger, *High aspect ratio ultrathick, negative-tone near-UV photoresist and its applications for MEMS*. *Sensors and Actuators A: Physical*, 1998. 64: p. 33-39.
9. J. D. Williams, R. Yang, and W. Wang, *Numerical Simulation and Dynamic Test of UV-LIGA Fabricated Electromagnetic Micro-relay for Power Applications*. *Sensors and Actuators A: Physical*, 2005. 120(1): p. 154-162.
10. K.-H. Hang, W. Wang, M. C. Murphy, and K. Lian. *UV-LIGA Microfabrication and Test of an AC Type Micropump Based on Magnetohydrodynamic (MHD) Principle*. in *SPIE Symposium on Microfabrication*. 2000. Santa Clara, CA.
11. L. Dellmann, S. Roth, C. Beuret, L. Paratte, G.-A. Racine, H. Lorenz, M. Despont, P. Renaud, P. Vettiger, and N. de Rooij, *Two steps micromoulding and photopolymer high-aspect ratio structuring for applications in piezoelectric motor components*. *Microsystem Technologies*, 1998. 4: p. 147-150.

12. Ren Yang, S. J. Jeong, and W. Wang. *UV-LIGA microfabrication of a power relay based on electrostatic actuation*. in *Micromachining and Microfabrication, Photonics West*. 2003. San Jose, California.
13. Y. Konaka, Mark G. Allen. *Single and multi-layer electroplated microaccelerometers*. in *Proceedings of the IEEE Micro Electro Mechanical Systems (MEMS)*. 1996.
14. H. Chang, Y. Kim, *UV-LIGA process for high aspect ratio structure using stress barrier and C-shaped etch hole*. *Sensors and Actuators A: Physical*, 2000. 84: p. 342-350.
15. J. D. Williams, W. Wang, *Study on the postbaking process and the effects on UV lithography of high aspect ratio SU-8 microstructures*. *Journal of Microlithography, Microfabrication and Microsystems*, 2004. 3(4): p. 563-568.
16. J. Zhang, K. L. Tan, G. D. Hong, L. J. Yang, and H. Q. Gong, *Polymerization optimization of SU-8 photoresist and its applications in microfluidic systems and MEMS*. *Journal of Micromechanics and Microengineering*, 2001. 11(1): p. 20-26.
17. C. Lin, G. Lee, B. Chang, and G. Chang, *A new fabrication process for ultra-thick microfluidic microstructures utilizing SU-8 photoresist*. *Journal of Micromechanics and Microengineering*, 2002. 12(5): p. 590-597.
18. Z. Ling, K. Lian, L. Jian. *Improved patterning quality of SU-8 microstructures by optimizing the exposure parameters*. in *Proceeding of SPIE*. 2000.
19. P. M. Dentinger, K. L. Krafcik, K. L. Simison, R. P. Janek, J. Hachman, *High aspect ratio patterning with a proximity ultraviolet source*. *Micronic Engineering*, 2002. 61-62: p. 1001-1007.
20. J. O'Brien, P. J. Hughes, M. Brunent, B. O'Neil, J. Alderman, B. Lane, A. O'Riordan, C. O'Driscoll, *Advanced photoresist technologies for microsystems*. *Journal of Micromechanics and Microengineering*, 2001. 11(4): p. 351-358.
21. R. Yang, W. Wang, *Application of Optical Refractive Index Liquid and Wavelength Selection for Ultra-high-aspect-ratio UV-lithography of Thick SU-8 Resist*. *Sensor and Actuator B: Chemical*, 2005. 110(2): p. 279-288.
22. R. Yang, T. Chen, H. Chen, W. Wang, *Microfabrication of Biodegradable (PLGA) Honeycomb-structures and Potential Applications in Implantable Drug Delivery*. *Sensors and Actuators B: Chemical*, 2005. 106(2): p. 506-511.
23. R. Yang, T. Chen, H. Chen, W. Wang. *Fabrication of Biodegradable Polymer (PLGA) Microstructures and Applications in Controlled Drug Delivery*. in *SPIE Photonics West*. 2004. San Jose, CA.

24. R. Yang, J. D. Williams, W. Wang, *A Rapid Micro-mixer/reactor Based on Arrays of Spatially Impinging Micro-jets*. Journal of Micromechanics and Microengineering, 2004. 14(10): p. 1345-1351.
25. R. Yang, D. L. Feedback, W. Wang, *Microfabrication and Test of Three-Dimensional Polymer Hydro-focusing Unit for Flow Cytometry Applications*. Sensors and Actuators A: Physical, 2005. 118(2): p. 259-267.
26. R. Yang, W. Wang, *Out-of-plane Polymer Refractive Microlens Fabricated Based on Direct Lithography of SU-8*. Sensor and Actuators A: Physical, 2004. 113(1): p. 71-77.
27. R. Yang, S. Soper, and W. Wang, *Out-of-Plane Microlens Array Fabricated using Ultraviolet Lithography*. Applied Physics Letter, 2005. 86(16): p. 161110.
28. R. Yang, W. Wang, *Numerical and Experimental Study on an Out-of-Plane Pre-aligned Refractive Microlens Fabricated Using UV Lithography Method*. Optical Engineering, 2004. 43(12): p. 3096-3103.
29. R. Yang, Steve Soper, W. Wang, *Microfabrication of pre-aligned fiber bundle couplers using ultraviolet lithography of SU-8*. Sensors and Actuators, A: Physical, 2006. 127(1): p. 123-130.
30. R. Yang, W. Wang. *Fabrication of out-of-plane SU-8 refractive microlens using directly lithography method*. in *Proceedings of SPIE*. 2004. San Jose, CA.
31. R. Yang, S. A. Soper, W. Wang. *Fabrication of out-of-plane concave and convex refractive microlens array*. in *Proceedings of SPIE*. 2005.
32. N. LaBianca, J. Gelorme, K. Lee, E. Sullivan, J. Shaw. *High aspect ratio optical resist chemistry for MEMS applications*. in *Proc. 4th Int. Symp. on Magnetic Materials, Processes, and Devices*. 1995.
33. L. Guerin, M. Bossel, M. Demierre, S. Calmes, and P. Renaud. *Simple and low cost fabrication of embedded microchannels by using a new thick-film photoplastic*. in *Proc. Transducers 1997*. 1997. Chicago.
34. L. Dellmann, S. Roth, C. Beuret, G. Racine, H. Lorenz, M. Despont, P. Renaud, P. Vettiger, and N. de Rooij. *Fabrication process of high aspect ratio elastic structures for piezoelectric motor applications*. in *Proceeding of Transducers 1997*. 1997. Chicago.
35. J. Thorpe, D. Steenson, and R. Miles, *High frequency transmission line using micromachined polymer dielectric*. Electronics Letters, 1998. 34(12): p. 1237-1238.
36. Wen Dai, Kun Lian, Wanjun Wang, *A quantitative study on the adhesion property of cured SU-8 on various metallic surfaces*. Microsystem Technologies, 2005. 11(7): p. 526-534.



37. M. Rabard, J. Bablet, M. Ruty, M. Kipp, I. Chartier, C. Dubarry. *Thick SU-8 photolithography for bioMEMS*. in *Proceedings of SPIE - The International Society for Optical Engineering*. 2003.
38. Jamil El-Ali, I. R. Perch-Nielsen, Claus R. Poulsen, Duong D. Bang, Pieter Telleman, Anders Wolff, *Simulation and experimental validation of a SU-8 based PCR thermocycler chip with integrated heaters and temperature sensor*. Sensors and Actuators, A: Physical, 2004. 110(1-3): p. 3-10.
39. Yoonsu Choi, Richard Powers, Varadraj Vernekar, A. Bruno Frazier, Michelle C. LaPlaca, Mark G. Allen. *High aspect ratio SU-8 structures for 3-D culturing of neurons*. in *American Society of Mechanical Engineers, Micro-Electromechanical Systems Division Publication (MEMS)*. 2003.
40. C.-M. Cheng, R.-H. Chen, *Development behaviours and microstructure quality of downward-development in deep x-ray lithography*. Journal of Micromechanics and Microengineering, 2001. 11(6): p. 692-696.
41. J. D. Williams, W. Wang, *Using megasonic development of SU-8 to yield ultra-high aspect ratio microstructures with UV lithography*. Microsystem Technologies, 2004. 10(9): p. 694-698.
42. H.C. Ho, K.-P. Chin, C.R. Yang, H.-M. Wu, S.-L. Chen, *Ultrathick SU-8 mold formation and removal, and its application to the fabrication of LIGA-like micromotors with embedded roots*. Sensors and Actuators, A: Physical, 2002. 102(1-2): p. 130-138.
43. R. Yang, J. Jiang, W.J. Meng, W. Wang, *Numerical simulation and fabrication of microscale, multilevel, tapered mold inserts using UV-Lithographie, Galvanoformung, Abformung (LIGA) technology*. Microsystem Technologies, 2006. 12(6): p. 545-553.
44. D. M. Cao, J. Jiang, R. Yang, W. J. Meng, *Fabrication of high-aspect-ratio microscale mold inserts by parallel  $\mu$ -EDM*. Microsystem Technologies, 2006. 12(8): p. 131-138.
45. M. P. Dentinger, W. M. Clift, S. H. Goods, *Removal of SU-8 photoresist for thick film applications*. Microelectronic Engineering, 2002. 61-62: p. 993-1000.
46. M. K. Ghantasala, J.P. Hayes, E.C. Harvey, D.K. Sood, *Patterning, electroplating and removal of SU-8 moulds by excimer laser micromachining*. Journal of Micromechanics and Microengineering, 2001. 11(2): p. 133-139.
47. K. Kim, S. D. Park, M. H. Lu, W. Che, K. Kim, J.-B. Lee, C. H. Ahn, *A tapered hollow metallic microneedle array using backside exposure of SU-8*. Journal of Micromechanics and Microengineering, 2004. 14(4): p. 593-603.
48. Y.-K. Yoon, H.-H. Park, F. Cros, M. G. Allen. *Integrated vertical screen microfilter system using inclined SU-8 structures*. in *Proceedings of the IEEE Micro Electro Mechanical Systems (MEMS)*. 2003.

49. H. Sato, Y. Houshi, S. Ito, S. Shoji, *Improved inclined multi-lithography using water as exposure medium and its 3D mixing microchannel application*. Sensors and Actuators, A: Physical, 2006. 128(1): p. 183-190.
50. H. Sato, Y. Houshi, T. Otsuka, S. Shoji. *Fabrication of the 3-D SU-8 fine micromesh and electroplated Ni micromesh structures*. in *Digest of Papers - Microprocesses and Nanotechnology 2004*. 2004.
51. M. Han, W. Lee, S.-K. Lee, S. S. Lee. *Fabrication of 3D microstructures with inclined/rotated UV lithography*. in *Proceedings of the IEEE Micro Electro Mechanical Systems (MEMS)*. 2003.
52. M. Han, W. Lee, S.-K. Lee, S. S. Lee, *3D microfabrication with inclined/rotated UV lithography*. Sensors and Actuators A: Physical, 2004. 111(1): p. 14-20.
53. K.-Y. Hung, H.-T. Hu, F.-G. Tseng, *Application of 3D glycerol-compensated inclined-exposure technology to an integrated optical pick-up head*. Journal of Micromechanics and Microengineering, 2004. 14(7): p. 975-983.
54. H. Sato, T. Kakinuma, J. S. Go, S. Shoji. *A novel fabrication of in-channel 3-D micromesh structure using maskless multi-angle exposure and its microfilter application*. in *Proceedings of the IEEE Micro Electro Mechanical Systems (MEMS), 2003*. 2003.
55. M. Didier, V.L. Harald, R.-M. Gilles, H. Roland. *A High-Performance Silicon Micropump for an Implantable Drug Delivery System*. in *Proceedings of the 12th IEEE Internal Conference on Micro Electro Mechanical Systems*. 1999. Orlando, Florida, USA.
56. J.T. Santini, Jr., R. Langer, M.J. Cima. *A Microfabricated Controlled Release Device*. in *10th International Conference on Solid-State Sensors and Actuators*. 1999. Sendai, Japan: Technical Digest.
57. J. Drake, H. Jermann *A Precision Flow Restrictor for Medical Infusion Therapy*. in *The 8th International Conference on Solid-State Sensors and Actuators, and Eurosensors IX*. 1995. Stockholm, Sweden.
58. S. Sershen, J. West, *Implantable, polymetric systems for modulated drug delivery*. Advanced Drug Delivery Review, 2002. 54: p. 1225-1235.
59. Heller, J., *Biodegradable polymers in controlled drug delivery*. CRC Critical Reviews in Therapeutic Drug Carrier Systems, Band, 1985. 1: p. 39-90.
60. Pitt, C. G., *The controlled parenteral delivery of polypeptides and proteins*. International Journal of Pharmaceutics, 1990. 59: p. 173-196.
61. L. Brannon-Peppas, A.L. Grosvenor, B.S. Smith. *Drug Delivery of Penicillin and  $\beta$ -estradiol from Biodegradable Microparticles within Degradable and Nondegradable*

- Films. in the 21st International Meeting of The Controlled Release Society, Proceedings of International Symposium on Control, Release of Bioactive Materials. 1994. Nice, France.*
62. F. Qian, N. Nasongkla, J. Gao, *Membrane-encased polymer millirods for sustained release of 5-fluorouracil*. Journal of Biomedical Materials Research, 2002. 61: p. 203-211.
  63. G. Vozzi, C. J. Flaim, F. Bianchi, A. Ahluwalia, S. Bhatia, *Microfabricated PLGA scaffolds: a comparative study for application to tissue engineering*. Materials Science Engineering, 2002. C: p. 760.
  64. R. Yang, S. J. Jeong, and W. Wang. *UV-LIGA microfabrication of a power relay based on electrostatic actuation*. in *Micromachining and Microfabrication, Photonics West*. 2003. San Jose, California.
  65. R. A. Vijayendran, K. M. Motsegood, D. J. Beebe, D. E. Leckband, *Evaluation of a three-dimensional micromixer in a surface-based biosensor*. Langmuir, 2003. 19(5): p. 1824-1828.
  66. K.-P. Kaemper, W. Ehrfeld, J. Doepper, V. Hessel, H. Lehr, H. Loewe, Th. Richter, A. Wolf. *Microfluidic components for biological and chemical microreactors*. in *Proceedings of the IEEE Micro Electro Mechanical Systems (MEMS)*. 1997.
  67. S. Norber, F. Thomas, W. Helmut, *A Modular Microfluid System With An Integrated Micromixer*. Journal of Micromechanics and Microengineering, 1996. 6(1): p. 99-102.
  68. M. Koch, H. Witt, *Improved characterization technique for micromixers*. Journal of Micromechanics and Microengineering, 1999. 9(2): p. 156-158.
  69. Z. Yang, S. Matsumoto, H. Goto, M. Matsumoto, R. Maeda, *Ultrasonic micromixer for microfluidic systems*. Sensors and Actuators, A: Physical, 2001. 93(3): p. 266-272.
  70. V. Bibhu, Y. Zeng, E. S. Kim. *Novel Acoustic-wave Micromixer*. in *Proceedings of the IEEE Micro Mechanical Systems (MEMS)*. 2000.
  71. R. Miyake, K. Tsuzuki, T. Takagi, K. Imai. *Highly sensitive and small flow-type chemical analysis system with integrated absorptiometric micro-flowcell*. in *Proceedings of the IEEE Micro Electro Mechanical Systems (MEMS)*. 1997.
  72. A.J. Mahajan, D.J. Kirwan, *Micromixing effects in a two-impinging-jets precipitator*. A/ChE Journal, 1996. 42(7): p. 1801-1814.
  73. Mohseni, K. *Mixing and impulse extremization in microscale vortex formation*. in *2002 International Conference on Modeling and Simulation of Microsystems*. 2002.

74. B.H. Weigl, R. L. Bardell, T. H. Schulte, C. F. Battrell, J. Hayenga. *Design and Rapid Prototyping of Thin-Film Laminate-Based Microfluidic Devices*. in *Biomedical Microdevices 2001*. 2001: Kluwer Academic Publishers.
75. R. Miyake, H. Ohki, I. Yamazaki, T. Takagi, *Flow cytometric analysis by using micro-machined flow chamber*. JSME International Journal, Series B, 2000. 43: p. 219-224.
76. R. Miyake, H. Ohki, I. Yamazaki, T. Takagi, *Investigation of sheath flow chambers for flow cytometers (micro machined flow chamber with low pressure loss)*. JSME International Journal, Series B, 1997. 40: p. 106-113.
77. B. H. Weigl, K. Hedine, *Lab-on-a-chip-based separation and detection technology for life science applications*. American Biotechnology Laboratory, 2002. 20(1): p. 28-30.
78. G.B. Lee, C.-H. Lin, G.-L. Chang, *Micro flow cytometers with buried SU-8/SOG optical waveguides*. Sensors and Actuators A: Physical, 2002. 103(1-2): p. 165-170.
79. A.Y. Fu, C. Spencel, A. Scherer, F.H. Arnold, S.R. Quake, *A microfabricated fluorescence-activated cell sorter*. Nature Biotechnology, 1999. 17: p. 1109-1111.
80. R.L. Bardell, B.H. Weigl, N. Kesler, T. Schulte, J. Hayenga, F. Battrell. *Microfluidic Disposables for Cellular and Chemical Detection - CFD Model Results and Fluidic Verification Experiments*. in *SPIE BIOS 2001*. 2001.
81. Weigl, B. H., *Microfluidics-based lab-on-a-chip systems*. IVD Technology, 2000. 6: p. 47-53.
82. B.H. Weigl, A. Hatch, A. Kamholz, P. Yager. *Novel Immunoassay Formats for Integrated Microfluidic Circuits - Diffusion Immunoassays (DIA)*. in *SPIE, Micro-& Nanotechnology for Biomedical and Environmental Applications, 2000*. 2000.
83. B. H. Weigl, R. L. Bardell, T. H. Schulte, C. Williams. *Passive Microfluidics- Ultra-Low-Cost Plastic Disposable Lab-on-a-chips*. in  *$\mu$ TAS 2000 Proceedings*. 2000. Dordrecht: Kluwer Academic Publishers.
84. B.H. Weigl, C.J. Morris, N. Kesler, C.F. Battrell, R.L. Bardell. *Standard and high-throughput microfluidic disposables based on laminar fluid diffusion interfaces*. in *SPIE BIOS 2002*. 2002. San Jose, CA, USA.
85. M. A. McClain, C. T. Culbertson, S. C. Jacobson, and J. M. Ramsey, *Flow Cytometry of Escherichia coli on Microfluidic Devices*. Analytical Chemistry, 2001. 73: p. 5334.
86. D. P. Schrum, C.T. Culbertson, S.C. Jacobson, J.M. Ramsey, *Microchip Flow Cytometry Using Electrokinetic Focusing*. Analytical Chemistry, 1999. 71: p. 4173.

87. G. Goranovic, I. R. Perch-Nielsen, U.D. Larsen, A. Wolff, J. P. Kutter, P. Telleman. *Three-Dimensional Single Step Flow Sheathing in Micro Cell Sorters*. in *International Conference on Modeling and Simulation of Microsystems - MSM 2001*. 2001.
88. S.-K. Lee, K.-C. Lee, S.S. Lee, *A simple method for microlens fabrication by the modified LIGA process*. Journal of Micromechanics and Microengineering, 2002. 12(3): p. 334-340.
89. M. Severi, P. Mottier, *Etching selectivity control during resist pattern transfer into silica for the fabrication of microlenses with reduced spherical aberration*. Optical Engineering, 1999. 38(1): p. 146-150.
90. R. Yang, K.F. Chan, Z. Feng, I. Akihito, W. Mei, *Design and fabrication of microlens and spatial filter array by self-alignment for maskless lithography systems*. Journal of Microlithography, Microfabrication and Microsystems, 2003. 2(3): p. 210-219.
91. S. Biehl, R. Danzebrink, P. Oliveira, M.A. Aegerter, *Refractive microlens fabrication by ink-jet process*. Journal of Sol-Gel Science and Technology, 1998. 13(1-3): p. 177-182.
92. H. Yang, M.-C. Chou, A. Yang, C.-K. Mu, R.F. Shyu. *Realization of fabricating microlens array in mass production*. in *Proceedings of SPIE - The International Society for Optical Engineering*. 1999.
93. Y. Ishii, S. Koike, Y. Arai, Y. Ando. *Hybrid integration of polymer microlens with VCSEL using drop-on-demand technique*. in *Proceedings of SPIE - The International Society for Optical Engineering*. 2000.
94. M. C. Wu, L. Y. Lin, S. S. Lee, C. R. King, *Free-space integrated optics realized by surface micromachining*. International Journal of High Speed Electronics and Systems, 1997. 8(2): p. 51-65.
95. Wu, M. C. *Micromachining for Optical and Optoelectronic Systems*. in *Proceeding IEEE*. 1997.
96. C.R. King, L.Y. Lin, M.C. Wu, *Out-of-Plane Refractive Microlens Fabricated by Surface Micromachining*. IEEE Photonics Technology Letters, 1996. 8(10): p. 1349-1351.
97. Yong W. Yi, Chang Liu, *Assembly of Micro Optical Components Using Magnetic Actuation*. Sensors and Actuators A: Physical, 1999. 78: p. 205-211.
98. A. Bertsch, H. Horenz, and P. Renaud. *Combining microstereolithography and thick resist UV lithography for 3D microfabrication*. in *Proceedings of the 1998 IEEE 11th Annual International Workshop on Micro Electro Mechanical Systems*. 1998. Heidelberg, German.

99. K. Ikuta, S. Maruo, S. Kojima. *New micro stereo lithography for freely movable 3D micro structure - Super IH process with submicron resolution.* in *Proceedings of the IEEE Micro Electro Mechanical Systems (MEMS)*. 1998. Heidelberg, Germany.
100. J. Mohr, J. Gottert, A. Muller, P. Ruther, K. Wengeling. *Micro-optical and opto-mechanical systems fabricated by the LIGA technique.* in *Proceedings of SPIE - The International Society for Optical Engineering*. 1997.
101. J.A. Cox, D. C. Dobson, T. Ohnstein, J. D. Zook, *Optical performance of high-aspect LIGA grating II.* *Optical Engineering*, 1998. 37(11): p. 2878-2884.
102. J. Hossfeld, T. Paatzsch, J. Schultze, M. Neumeier, L. Weber, H.-D. Bauer, W. Ehrfeld. *Polymetric Optical MEMS.* in *Symposium on Design, Test, and Microfabrication of MEMS and MEOMS*. 1999. Paris, France.
103. E. Reznikova, V. Namov, J. Mour, *Deep photo-lithography characterization of SU-8 resist.* *Microsystem Technologies*, 2005. 11(4-5): p. 282-291.
104. A. Borreman, S. Musa, A. Kok, M. Diemeer and A. Driessen. *Fabrication of Polymeric Multimode Waveguides and Devices in SU-8 Photoresist Using Selective Polymerization.* in *Proceedings Symposium IEEE/LEOS Benelux Chapter*. 2002. Amsterdam.
105. Y. Choi, R. Powers, V. Vernekar, A. B. Frazier, M. C. LaPlaca, M. G. Allen. *High aspect ratio SU-8 structures for 3-D culturing of neurons.* in *American Society of Mechanical Engineers, Micro-Electromechanical Systems Division Publication (MEMS)*. 2003.
106. J. D. Williams, Wanjun Wang. *Micro fabrication of an Electromagnetic Power Micro-Relay Using SU-8 Based UV-LIGA Technology.* in *High Aspect Ratio Micro-Structure Technology Workshop (HARMST2003)*. 2003. Monterey, California USA.
107. W. Dai, K. Lian, W. Wang, *A quantitative study on the adhesion property of cured SU-8 on various metallic surfaces.* *Microsystem Technologies*, 2005. 11(7): p. 526-534.
108. Y. J. Chuang, T. G. Tseng, W. K. Lin, *Reduction of diffraction effect of UV exposure on SU-8 negative thick photoresist by air gap elimination.* *Microsystem Technologies*, 2002. 8: p. 308-313.
109. S. Maruo, K. Ikuta, H. Korogi, *Submicron Manipulation Tools Driven by Light in a Liquid.* *Applied Physics Letters*, 2003. 82(1): p. 133-135.
110. S.J. Lee, W. Shi, P. Maciel, S.W. Cha. *Top-edge profile control for SU-8 structural photoresist.* in *Proceedings of 15th Biennial University/Government/Industry Microelectronics Symposium*. 2003. Boise, ID, USA.
111. J. D. Williams, Wanjun Wang. *UV Lithography process for ultra high aspect ratio SU-8 microstructures With and without megasonic development.* in *High Aspect Ratio Micro-Structure Technology Workshop (HARMST2003)*. 2003. Monterey, California USA.

112. J.D. Williams, W. Wang. *UV-LIGA fabrication of electromagnetic power micro-relays*. in *UV-LIGA fabrication of electromagnetic power micro-relays*. 2001.
113. R. Yang, S.J. Jeong, W. Wang. *UV-LIGA microfabrication of a power relay based on electrostatic actuation*. in *Proceedings of SPIE Symposium on Micromachining and Microfabrication, MEMS Components and Applications for Industry, Automobiles, Aerospace, and Communication II*. 2003.
114. C.E. Collins, R.E. Miles, J.W. Digby, G.M. Parkhurst, R.D. Pollard, J.M. Charnberlain, D.P. Steenson, N.J. Cronin, S.R. Davies, J.W. Bowen, *New micro-machined millimeter-wave and terahertz snap-together rectangular waveguide technology*. IEEE Microwave and Guided Wave Letters, 1999. 9(2): p. 63-65.
115. W.Y. Liu, D.P. Steenson, M.B. Steer. *Technique of microfabrication suitable for machining submillimeter wave components*. in *Proceedings of SPIE - The International Society for Optical Engineering*. 2000.
116. P.C. Deguzman, G.P. Nordin, *Stacked subwavelength gratings as circular polarization filters*. Applied Optics, 2001. 40(31): p. 5731-5737.
117. H. Han, J.D. Stack, J. Mathews, C.S. Koehler, E. Johnson, A.D. Kathman. *Integration of silicon bench with micro optics*. in *Proceedings of SPIE - The International Society for Optical Engineering*. 1999.
118. K. Song, J. Bu, Y. Jeon, C. Park, J. Jeong, H. Koh, M. Choi. *Micromachined silicon optical bench for the low cost optical module*. in *Proceedings of SPIE - The International Society for Optical Engineering*. 1999.
119. T. Abe, Z. Ito, M. Enomoto, Y. Matsumura, *New fabrication technique of lens-ended fibers for optical connector*. Tohoku Kogyo Daigaku Kiyo, 1986. 1: Rikogakuhen(6): p. 21-27.
120. W.R. Cox, T. Chen, D. Ussery, D.J. Hayes, J.A. Tatum, and D.L. MacFarlane, *Microjetted lenslet triplet fibers*. Optics Communications, 1996. 123(4-6): p. 492-496.
121. H. Yang, C. Chao, C. Lin, S. Shen, *Micro-ball lens array modeling and fabrication using thermal reflow in two polymer layers*. Journal of Micromechanics and Microengineering, 2004. 14(2): p. 277-282.
122. Pan, C. T., *Silicon-based coupling platform for optical fiber switching in free space*. Journal of Micromechanics and Microengineering, 2004. 14(1): p. 129-137.

123. H. Lorenz, M. Despont, N. Fahrni, N. Labianca, P. Renaud, and P. Vettiger, *SU-8: A low-cost negative resist for MEMS*. Journal of Micromechanics and Microengineering, 1997. 7(3): p. 121-124.
124. <http://www.resins.com/resins/am/products/Epon.html>.



## **VITA**

The author, Ren Yang, was born in January 1973, in Sichuan Province, People's Republic of China.

In September 1991, the author attended Tsinghua University with a majoring in precision instruments. He obtained a Bachelor of Science degree in precision instruments in July 1996. He continued his graduate study in Tsinghua University and obtained his Master of Science in optical engineering in March, 1999.

In June 1999, the author furthered his graduate study in the Engineering College, Louisiana State University. In May 2002, the author got his second Master of Science degree in engineering science.

From September 2001 to February 2003, the author works as optical engineer in Ball Semiconductor Inc., in Allen, Texas. From March 2003 to present, the author works as research associate in Louisiana State University.

In August 2006, the degree of Doctor of Philosophy will be conferred.